Plasmonic nanomaterials for label-free biosensor towards next-generation point-of-care immunoassay

by

Jiacheng He

A dissertation submitted to the Graduate Faculty of
Auburn University
in partial fulfillment of the
requirements for the Degree of
Doctor of Philosophy

Auburn, Alabama
December 11, 2021

Keywords: localized surface plasmon resonance (LSPR), biosensing, microfluidics, multiplexed immunoassay, cytokine

Approved by

Dr. Pengyu Chen, Chair, Associate Professor of Materials Engineering
Dr. Zhongyang Cheng, Professor of Materials Engineering
Dr. Dong-Joo Kim, Professor of Materials Engineering
Dr. Christopher Easley, Professor of Chemistry and Biochemistry
Dr. Feng Li, Assistant Professor of Drug Discovery and Development

Abstract

Cytokines, a broad category of low molecular weight signaling proteins, are key immune modulators for cell-based immune response. An abnormal level of cytokine can lead to acute/chronic inflammation, multiple organ failure, or even death. The current "gold standard" method for cytokine quantification is enzyme-linked immunosorbent assay (ELISA), which involves tedious labeling and washing process. In a current clinical laboratory setting, a minimum assay time of 3-8 h is required for simplex cytokine measurement. Considering a detrimental acute inflammation, characterized by the unregulated and increased level of cytokines, a personalized cytokine-blockade treatment needs to be delivered in time based on the individual's transient immune status. In this regard, an unmet need is developing a next-generation multiplexed immunoassay allowing rapid cytokine analysis with sufficient sensitivity. Localized surface plasmon resonance (LSPR)-based immunoassay that exploits attractive optical properties of plasmonic nanomaterials is a promising candidate to bridge such a gap. In this dissertation, we demonstrated the development of point-of-care nanoplasmonic immunoassay from three aspects. Firstly, we developed a scalable manufacturing method for the parallel fabrication of multiplexed immunoassay by using the weasel hair-enabled calligraphy technique. Secondly, we improved the sensing performance of the current LSPR immunoassay by engineering conventional antibodies and adopting a new LSPR sensing methodology, i.e., digital LSPR. Lastly, we demonstrated the practical use of our label-free LSPR immunoassay to characterize the T cell responses to a type 2 diabetes biomarker, human islet amyloid polypeptide (hIAPP) with differing aggregation stages. Together, we demonstrated the developed LSPR immunoassays can be a promising tool for patient immune status monitoring and cellular functional analysis.

Acknowledgments

The completion of this study could not have been possible without the help and guidance of many individuals. I would like to express my sincerest gratitude to each of those who supported and helped me during my time at Auburn University.

First and foremost, I would like to thank my advisor, Dr. Pengyu Chen for his continued support and guidance throughout my Ph.D. journey. I am so grateful to work with such an outstanding researcher for five years in plasmonic biosensing. His patience and encouragement got me through my difficult time. His immense knowledge and scientific rigor helped me develop my research abilities. I would like to extend my appreciation to my committee members: Dr. Zhongyang Cheng, Dr. Dong-Joo Kim, and Dr. Christopher Easley for their time to review this work and invaluable comments. My gratitude also goes out to our collaborators, Dr. Siyuan Dai, Dr. Bryan Chin, Dr. Feng Li, Dr. Feng Ding, Dr. Weiqiang Chen, and Dr. Pu Chun Ke for intense discussion and consistent engagement of our projects.

Besides, to Steven Moore, William Ingram, and Cheryl Rhodes, thank you for always being there to lend your assistance when I needed it. Thank you to all the members of Advanced Nanomaterials Engineering Laboratory: Dr. Lang Zhou, Dr. Zhuangqiang Gao, Dr. Jingyi Zhu, Wen Yang, Yuxin Cai, Chuanyu Wang, Alana MacLachlan, Lili Chen, Yuan Gao, Te Yi Hsiao, Yiming Cheng, Feng Xiong and Zhengyang Gu. It is their help that made my study possible. Additionally, I would like to express my gratitude to my friends, Dr. Yuzhe Sun, Dr. Yuzhe Liu, Dr. Songtao Du, Dr. Liangxi Li, Dr. Xingxing Zhang, Dr. Anqi Zhang, Dr. Yan Chen, Dr. Pu Deng, Dr. Jiahui Xu, Dr. Jianguo Xi, Dr. Haijiao Wang, Doohee Lee, Jaesik Yoon, Bin Bai, Dongliang Chen, Yimeng Zhang, Shuo Liang, Weili Liu, Bolin Li, Haiyan Li, Tiantian Gao, Zhaoyin Liu, Siyuan Ran, Rukai Guo, Zhicheng Zhao, Jiachen Liu, Yanceng Cai, Jingdong Wei Jialiang Sheng,

Mingyuan Chen, Shuai Wu, Haotian Wu, Jingfan Yang, Houshang Yin, Qingyu Pan, Wu Chen, Xuejia Kang, Chung-Hui Huang, Qi Wang, Junwei Wang Xin Wei, Nan Shi, Yaokun Xu, Xianze Sun, Zihan Zhang, Sida Zhang, Renjie Li, Jiucheng Cai and Yao Lin.

Lastly, I would like to express my deepest appreciation to my family for their conditional love and unwavering support.

Thank you and War Eagle!

Table of Contents

Chapter 3

List of Tables

List of Figures

List of Abbreviations

0D	0-dimensional
1D	1-dimensional
2D	2-dimensional
3D	3-dimensional
Ab-AuNR	Antibody-conjugated gold nanorod
AC	Alternating current
ACE-2	Angiotensin-converting enzyme 2
ADPA	Antibody-derived peptide aptamer
ADPA-AuNR	Antibody-derived peptide aptamer -conjugated gold nanorod
AgNC	Silver nanocube
APTES	(3-Aminopropyl)triethoxysilane
ARDS	Acute respiratory distress syndrome
AuNBP	Gold Nanobipyramid
AuNP	Gold nanoparticle
bLg	Beta-lactoglobulin
BSA	Bovine serum albumin
CAb	Capture antibody

CD	Circular dichroism
CDR	Complementarity-determining region
Cit	Citrate
Cit-AuNR	Citrate-capped gold nanorod
CNN	Convolutional neural network
CNT	Carbon nanotube
COMSOL	Commercial multiphysics simulation software
COVID-19	Coronavirus disease 2019
CPU	Central processing unit
CTAB	Hexadecyltrimethylammonium bromide
DAb	Detection antibody
DC	Direct current
DI	Deionized
DLS	Dynamic light scattering
DMEM	Dulbecco's modified eagle medium
ECMO	Extracorporeal membrane oxygenation
EDC	1-ethyl-3-(3-dimethylaminopropyl)carbodiimide
EG	Ethylene glycol

EIS	Electrochemical impedance spectroscopy
ELISA	Enzyme-linked immunosorbent assay
EMCCD	Electron-multiplying charge-coupled device
FBS	Fetal bovine serum
FEA	Finite element analysis
FEM	Finite element method
FET	Field effect-transistor
GTS	Global thresholding and segmentation
H	Height
HFIP	Hexafluoro-2-propanol
hIAPP	Human islet amyloid polypeptide
HRP	Horseradish peroxidase
HSI	Hyperspectral imaging
IAPPa	IAPP amyloid
IAPPm	IAPP monomer
IAPPo	IAPP oligomer
ICU	Intensive care unit
ID	Identification

IFN-γ	Interferon gamma
IL-1β	Interleukin 1 beta
IL-2	Interleukin 2
IL-4	Interleukin 4
IL-6	Interleukin 6
IL-10	Interleukin 10
IR	Infrared
LOD	Limit of detection
LPS	Lipopolysaccharides
LSP	Localized surface plasmon
LSPR	Localized surface plasmon resonance
mRNA	Messenger ribonucleic acid
MALDI	Matrix-assisted laser desorption/ionization
ML	Machine learning
MOFs	Multiple organ failures
MS	Mass spectrometry
MW	Molecular weight
NHS	N-hydroxysuccinimide

NK	Natural killer
NMR	Nuclear magnetic resonance
NPs	Nanoparticles
PBS	Phosphate buffered saline
PBST	Phosphate buffered saline with 0.05% tween-20
PDI	Polydispersity index
PDB	Protein data bank
PDMS	Polydimethylsiloxane
PEG	Polyethylene glycol
PEG-COOH	Polyethylene glycol-carboxyl
PI	Propidium iodide
PMA	12-myristate-13-acetate
PMMA	Poly(methyl methacrylate)
PoC	Point-of-care
PTT	Photothermal therapy
PVA	Poly(vinylalcohol)
PVP	Poly(vinylpyrrolidone)
QCL	Quantum cascade laser

qPCR	Quantitative polymerase chain reaction
ReLU	Rectified linear unit
RPMI	Roswell park memorial institute
S protein	Surface protein
SARS-CoV-2	Severe acute respiratory syndrome coronavirus 2
SAW	Surface acoustic wave
SEM	Scanning electron microscope
SGDM	Stochastic gradient descent with momentum
SP	Surface plasmon
SPR	Surface plasmon resonance
s-SNOM	Scattering-type scanning near-field optical microscopy
STD	Standard deviation
T2D	Type 2 diabetes
TAM	Tumor-Associated Macrophage
TCEP	Tris(2-carboxyethyl)phosphine
TEM	Transmission electron microscope
TGF-β	Transforming growth factor beta
ThT	Thioflavin T

TLR2	Toll-like-receptor-2
TMB	3,3′,5,5′-Tetramethylbenzidine
TNF-α	Tumor necrosis factor alpha
UV-Vis	Ultraviolet-visible
W	Width
WGM	Whispering-gallery-mode

List of Symbols

C_{scs}	Scattering cross section area
ΔD	Deformed distance
D_i	Initial distance
D_f	Finial distance
d_1	Thickness of recognition layer
d_2	Thickness of analyte layer
ΔI	Scattering light intensity change
I_i	Initial scattering light intensity
I_f	Final scattering light intensity
I_{AuNR}	Scattering intensity from AuNR
$I_{background}$	Scattering intensity from background
K_a	Association constant
K_d	Dissociation constant
K_D	Equilibrium dissociation constant
l_d	Decay length
M	Refractive index response
Nimage total pixels	Number of total pixels

Nclass pixels	Number of pixels for each class
R	Plasmonic response
Ω	Far-field plane
λ	Wavelength
$\Delta\lambda$	Resonance wavelength shifting
θ	Title angle
ξ	Zeta potential
$\Delta\eta$	Refractive index difference
ϵ_1	Dielectric constant
ω_p	Plasmon frequency
γ	Damping frequency

Chapter 1

Introduction

1.1 Background and Motivation

1.1.1 Nanomaterials

Nanomaterials are defined by materials with nanoscale size/surface in any dimension, while nanoparticles are particles that have an external dimension on the nanoscale (1~100 nm) in all three dimensions.[1] Therefore, all nanoparticles are nanomaterials, but some nanomaterials are not strictly nanoparticles. Due to their smaller size, nanomaterials possess unique physical and chemical properties from bulk materials that arose from a high surface-to-volume ratio and nanoscale size.[2] Compared with bulk materials, nanomaterials have a larger fraction of surface atom, which behaves differently from the interior atom. Pokropivny *et al* classified nanomaterials based on their number of dimensions in nanoscale.[3] 0-dimensional (0D) nanomaterials are materials with all three dimensions in nanoscale. This includes all nanoparticles such as nanosphere, nanorod, and nanocube.[4-6] 1-dimensional (1D) nanomaterials include materials with

two dimensions in nanoscale, such as nanofiber.[7] 2-dimensional (2D) nanomaterials represent materials that only have one dimension in nanoscale, such as MXene.[8]

Nanomaterials can be classified into carbon-based nanomaterials, ceramics-based nanomaterials, polymer-based nanomaterials, lipid-based nanomaterials, and metal-based nanomaterials.[2, 9] Graphene and carbon nanotube (CNT) are two types of well-known carbon-based nanomaterials due to their attractive electrical conductivity.[10] Ceramics-based nanomaterials are inorganic materials found applications in catalysis.[11] Polymer-based nanomaterials are usually based on organics and serve as matrix materials.[12] Lipid-based nanomaterials are normally spherical materials encapsulating a solid core and currently applied in drug delivery and messenger ribonucleic acid (mRNA) vaccine.[13] Metal-based nanomaterials are one of the extensively studied nanomaterials for their peculiar optical behavior. Among all metal-based nanomaterials, plasmonic nanoparticles, e.g., gold nanoparticles and silver nanoparticles, have accumulated increasing attention biosensing and photothermal therapy (PTT) because of a well-known localized surface plasmon resonance (LSPR).[6, 14-15]

Plasmon is a form of collective oscillation of electrons in metal with respect to the fixed positive ions.[16] Surface plasmon (SP) refers to the plasmon confined to the metal surface and it takes the form of localized surface plasmon (LSP) in a nanoparticle. LSP can be excited by electromagnetic radiation with a wavelength significantly larger than the size of plasmonic nanoparticle and the maximum oscillation amplitude is found at the resonant frequency.[17] It has two critical effects: (*i*) the strength of electric field is greatest at nanoparticle surface and exponentially decaying into the medium; (*ii*) the absorption maximized at plasmon resonant frequency. Therefore, LSPs are sensitive to the local refractive index variation and can be employed for delicate biosensing applications. In contrast to surface plasmon resonance (SPR) that senses the bulk dielectric

environment variation within a range of up to 600-1000 nm, LSPR, with a decay length of tens of nanometer, is less susceptible for the bulk effect and nonspecific bindings. Another advantage is that, compared to SPR, LSPR requires less bulky optics, thereby being promising for point-of-care (PoC) applications.

1.1.2 Biosensors and immunoassays

Biosensors are analytic devices that transduce the presence of a chemical or biological substance into a measurable signal.[18] Immunoassay is a specific biosensor that employs antibodies to detect the concentration of macromolecules, typically proteins. A typical biosensor is composed of a transducer, a bioreceptor, and an analyte.[19] The transducer is the detector element that transforms a biorecognition event into a measurable signal. The bioreceptor is an element that specifically recognizes target molecules and in immunoassay, antibodies are the most used. The analyte is the substance of interest.

The first generation of biosensor that measured oxygen concentration in blood was reported by Leland in 1956.[20] Then Clark developed a glucose biosensor utilizing an amperometric enzyme electrode.[21] The first potentiometric-based biosensor was demonstrated by Guilbault in 1969.[22] The second generation of biosensor integrated co-reactants to enhance the analytical performance.[23-24] In the third generation, bioreceptors became a part of sensing element.[18] Liedberg presented the first real-time SPR biosensing platform in 1983.[25] Biosensing platforms utilizing different detection methodologies have so far been reported and they can be either classified into label detection methods or label-free detection methods.[26-27] A label detection method utilizes foreign molecules attached to the probe element to report the presence of target molecules. It typically involves multiple labeling and washing process, therefore that a long assay time is resulted. For example, the “gold standard” method for protein detection, enzyme-linked

immunosorbent assay (ELISA), employs enzymes conjugated to secondary antibodies and after the binding between secondary antibodies and target proteins, enzymes catalyze substrate and induce a color change. Label-free methods, on the other hand, make use of intrinsic molecular properties, including molecular weight and refractive index, to report the target presence. As a result, the total assay time is greatly shortened and, more importantly, individual binding events can be monitored in a real-time manner.

Fluorescent-based detection is one of the most common methods used in sandwich structure-based immunoassay, in which fluorescent dyes are conjugated to secondary antibodies (detection antibodies).[28-29] The binding of the target molecule forms a so-called sandwich structure, i.e., primary antibody-analyte-secondary antibody. By recording fluorescent intensity, analyte concentration can be back-calculated from an established calibration curve. However, this method suffers from the false-positive signals induced from perturbations in molecular interactions and photobleaching.[27]

Similarly, the reactant can be labeled by an isotope (isotopic labeling) and detected by various analytic methods. Mass spectrometry is employed to the mass difference in an isotope. Infrared spectroscopy detects vibrational mode differences. Gyromagnetic ratio difference can be detected by nuclear magnetic resonance (NMR).

Chemiluminescent-based detection also transforms the binding events into the emission of light, but it differs from fluorescent method because the luminescence emitted is the result of a chemical reaction, rather than of the photon absorption. One photon of light is given off during molecular relaxation to lower energy states.[27] Chemiluminescent methods have so far been demonstrated to simultaneously measure analytes in low concentrations, but suffered from inefficient energy transfer.[30]

Mass spectrometry (MS) is a sensitive, high-throughput, and, in many cases, label-free technique that detects ionized analytes based on their mass-to-charge ratio.[26] For a long time, MS was limited to the detection of small molecules due to no effective method to noninvasively ionize samples.[31] This barrier was breached by the development of matrix-assisted laser desorption/ionization (MALDI). So far, MALDI-based MS has been applied in proteomics and metabolites analysis.[32-34]

Mechanical-based biosensing is a rapid and label-free detection method that measures the surface deflection or resonance shift resulting from surface stress or mass change upon analyte-receptor interaction.[26] Binding of the analyte can be quickly detected and transduced into the signal response of a bending or vibration frequency change.[35-37] Microcantilever-deflection-based biosensors exploit microscale structures that act as physical, chemical, or biological sensors by detecting changes of the cantilever deflection induced by weight variations on the surface. Quartz crystal biosensing platforms detect the oscillation frequency variation caused by mass change.[38] The other common mechanical biosensor employs surface acoustic wave (SAW). By applying a propagating acoustic wave on the surface of a piezoelectric crystal, the mass change of the crystal leads to the frequency variation of the applied wave.[39]

Electrochemical biosensors transduce biorecognition events into electrical signals, such as current, potential, and impedance. Compared to mechanical biosensors, electrochemical biosensors typically show higher sensitivity, while it remains challenging to deal with real biological samples with high ion strength and diverse interfering molecules. Amperometric biosensors detect current variation in a redox reaction.[40] Owing to its simplicity, low cost, and ease of miniaturization, this method has been applied in protein, exosome, and microRNA analysis.[41-43] However, redox reactions usually require an electron-transfer reagent, limiting its usage for recording the dynamic

information in a biological reaction. Electrochemical impedance spectroscopy (EIS) is a technique that measures the electrical impedance of an interface in the alternating current (AC) steady-state with constant direct current (DC) bias conditions.[44] EIS-based technique exerts minimal damage to the biological samples by imposing a small sinusoidal voltage at a particular frequency, therefore being well-suited for biosensing.[26] Recent progress in 2D nanomaterials have advanced field-effect-transistor (FET) based biosensor, which is sensitive to the local electric property changes, but like other electrochemical sensors, its performance is greatly affected by interfering molecules coexisted in the sample.

Optical biosensors that convert biorecognition events into a light signal, such as resonance wavelength or light intensity, on the other hand, allow the direct detection of a variety of chemical and biological substances. Photonic crystals are dielectric material-based periodic nanostructures that can trap light with a specific wavelength in a confined small volume by reflection.[45] The deposition of target analytes on photo crystal creates a local disruption of the periodicity and symmetry of the crystal, thus inducing a reflection wavelength change. Photonic crystal biosensors typically exhibit superior sensitivity because of the high-quality factor of the perfectly arranged structure. Whispering-gallery-mode (WGM) based biosensing platform utilizes the light confinement within a glass sphere through continuous total internal reflection.[46] When the optical path length is an integer multiple of the wavelength, resonance occurs, to yield a dip in the light intensity transmitted. The binding of target molecules on the sphere increases this path length, which can be characterized by a redshift at a given resonant frequency.

The plasmonic biosensor was first reported in 1983 by Liedberg and is now one of the most widely used optical biosensors.[25, 47] Early plasmonic biosensing platforms employ SPR, in which a propagating evanescent wave sensitive to the refractive index variation is generated on the metal

surface. Currently, SPR technique has been predominantly applied in studying bio-molecule surface binding, analyte-antibody binding affinity, protein-protein interactions, and cell detection.[48-50] SPR biosensors usually employ the conventional Kritschmann configuration that requires bulky optical equipment, posing a significant challenge for system miniaturization. Furthermore, its evanescent field shows a greater depth of penetration, therefore being susceptible to non-specific binding and bulk effect. In contrast, LSPR occurs at the interface between a noble nanoparticle and its surrounding medium upon the light illumination at a specific wavelength. Since the electric field is dramatically enhanced on the nanoparticle surface, LSPR is extremely sensitive to the local refractive index change. Current LSPR-based detection typically takes the form of a label-free sensing scheme, in which probe elements, such as antibodies or aptamers, are functionalized on the nanoparticle surface. The binding of the target leads to a local refractive index change and induces a measurable optical signal, i.e., resonance wavelength shift and light intensity change. Due to its excellent sensitivity and ease of system miniaturization, integration, and multiplexing, the LSPR-based biosensing platform is a promising candidate for next-generation point-of-care immunoassay.

1.1.3 Microfluidics-based immunoassay

Microfluidics is the science and technology of a system in that fluid is constrained and manipulated in channels with microscale dimensions.[51] Common microfluidics materials are rigid polymers, inorganic materials, including silicon, glass and ceramics, and polydimethylsiloxane (PDMS).[52] The first material used for microfluidics was silicon because its surface properties were thoroughly investigated and understood in the semiconductor industry.[51] Glass quickly took over due to its superior optical transparency and biocompatibility. However, the fabrication of glass and silicon involves sophisticated instruments and hazardous chemicals and therefore such inorganics-

based microfluidics devices are expensive. Another type of popular microfluidics material is rigid polymers, such as poly(methyl methacrylate) (PMMA). The advantages of PMMA are (*i*) excellent optical transparency; (*ii*) ease of fabrication. Still, due to its potential deformation during fabrication and high roughness of channel, PMMA-based microfluidics device did not successfully transit from laboratory prototype to massive production at industry level. In this regard, PDMS, a silicon-based polymer, has emerged as the most widely used microfluidics material for its low cost, optical transparency, biocompatibility, and ease of large-scale fabrication. Driven by the recent advances in microfabrication, emerging microfluidics applications include biochip for point-of-care diagnosis of diseases, high throughout sequencing and single-cell manipulation.[26, 53-55]

For cellular analysis, microfluidic systems offer a powerful means for upstream sample processing in isolation, purification, concentration, and culturing of cells of interest. Therefore, it can be used to provide a biologically relevant microenvironment for cellular analysis with a carefully managed solution at a high spatial resolution.[26] Moreover, the flexible design of microfluidic structure allows the isolation of single cells of interest from a cell population, by either confining the cells in a functionalized microstructure surface, such as microwells or trapping/sorting the target cells using force gradients generated by specially designed electromagnetic fields.

Over the past decade, microfluidics has been extensively integrated with biosensing platforms because traditional immunoassays suffer from long assay time, unsatisfactory sensing performance, and high cost.[56]. In a routine clinical setting, well-trained personnel is needed to perform complicated and tedious sampling, labeling, and washing processes and the turnaround assay time can thus be several days. In this regard, microfluidics-based biosensing platforms have shown great promise to tackle these challenges. Such a miniaturized system provides a highly confined microenvironment therefore that target molecules in sample fluid are in close proximity to the

biorecognition element.[47] As a result, the diffusion time required for analytes captured by probe elements is greatly reduced, leading to a shorter turnaround time. At the same time, sample consumption is also reduced in microfluidics-based biosensors. Moreover, the integration of microfluidics devices allows multiplexed and high throughput detection, which is critical in clinical applications.[6] All these unique attributes, together with ease of fabrication and low cost, render microfluidics-based biosensors being well-suited for real-world clinical applications.

Current microfluidics-based biosensors can be primarily categorized into (i) paper-based biosensing; (ii) discrete microfluidics-based biosensing and (iii) channel-based biosensing.[57] Paper-based microfluidic biosensors have accumulated tremendous interest for their low-cost and superior biocompatibility and portability. Owing to its intrinsic porous structure, paper-based microfluidics devices permit capillary flow for reagent storage, mixing, and reaction.[57] Discrete microfluidics-based biosensing is another emerging technique allowing the dispensing of fluids into different functional modules (microchambers) and the isolation of each module is achieved by the oil phase. Among all three classes of microfluidics-based biosensors, channel-based biosensing is the most commonly used, in which microscale flow regimes are defined by microchannels and pumps are employed to manipulate continuous flow of fluids. Differing functionalities, such as sample pre-treatment, preparation, and analysis, are therefore realized by assigning to different microchannels. In this study, we will take advantage of microchannel-based microfluidics and integrate it into nanoplasmonic biosensing.

1.1.4 Cytokine

Cytokines are a category of low molecular weight signaling proteins secreted from a range of cells, such as macrophages, lymphocytes, and natural killer (NK) cells. They are responsible for the modulation of cell-based immune response and regulation of cell maturation and growth.[58-59]

Based on their role, cytokines have been classically classified into pro-inflammatory cytokines, such as interleukin 6 (IL-6) and tumor necrosis factor-alpha (TNF-α) and anti-inflammatory cytokines, including interleukin 4 (IL-4) and interleukin 10 (IL-10).[60] Pro-inflammatory cytokines are responsible for inducing acute immune responses to fight against infection and irritation, while anti-inflammatory cytokines, on the other hand, are critical in inhibiting the hyper-inflammatory status.[61] Noteworthy, some cytokines can both have pro-inflammatory activity and anti-inflammatory activity.

Abnormally increased levels of cytokine can induce cytokine storm, multiple organ failures, or even death. For example, cytokine release syndrome (CRS), excessive secretion of the pro-inflammatory cytokine, has been reported as one of the major causes of morbidity for coronavirus disease 2019 (COVID-19).[62-63] Therefore, cytokine levels in biological fluids, including blood and serum, offer clinically valuable information for disease diagnosis and immune monitoring.[61] However, the precise quantification of cytokines in a timely and inexpensive manner remains a challenge due to their low concentrations in the circulating system and short half-lives.[64] For example, TNF-α has a half-life of 18.2 min *in vivo* and is subject to rapid degradation in the sample collection and handling process.[65] As a direct consequence, inappropriate handing and long assay time can cause false negative signals. In addition, cytokine levels can significantly change after three cycles of freeze-thaw.[66] Moreover, multiple cytokines produced from a complicated network are involved in maintaining a regulated balance of immunity, the simultaneous detection of a panel of cytokines is of great significance. In this study, we will demonstrate the development of next-generation point-of-care nanoplasmonic immunoassay with high sensing performance, high throughput, and multiplex capability.

1.2 Dissertation Structure

This work presents the development of nanoplasmonic biosensing platforms for next-generation PoC immunoassay from three aspects: assay fabrication, enhanced sensitivity, and rapid detection. General background and motivation are discussed in Chapter 1. Four projects aimed to address the aforementioned three critical concerns are introduced in Chapter 2-5 (**Figure 1.1**). The remaining challenges and future directions are discussed in Chapter 6.

In Chapter 1, we introduced the motivation of this study and discussed state-of-art techniques and knowledge on nanomaterials, immunoassays, microfluidics, and cytokine detection. We pointed out LSPR-based immunoassays can serve as a promising candidate for next-generation PoC immunoassays.

In Chapter 2, we developed a massively parallel immunoassay manufacturing technique that enabled the production of multiplexed plasmonic immunoassay in less than one minute. We exploited the hierarchically anisotropic microstructure of weasel hair to controllably transfer nanoplasmonic bioink onto the substrate. As-fabricated multiplexed immunoassay was employed to characterize the mouse macrophages' responses to differing stimulations.

In Chapter 3, we improved the sensing performance of LSPR immunoassay by designing a new probe element, i.e., antibody-derived peptide aptamer (ADPA), and directly functionalizing ADPA onto citrate-capped gold nanorod (Cit-AuNR) surface. Due to its significantly smaller dimension, ADPA-based LSPR immunoassay exhibited a limit of detection (LOD) of 4.56 pg/mL and was used to profile the responses of severe acute respiratory syndrome coronavirus 2 (SARS-CoV-2) surface protein stimulated epithelial cells and macrophages.

In Chapter 4, we further enhanced the sensitivity of LSPR immunoassay by developing a machine-learning (ML)-assisted microfluidic nanoplasmonic immunoassay to meet the rising demand for cytokine storm monitoring in COVID-19 patients. The sensing performance was improved due to the use of (*i*) an ultrasensitive silver nanocube (AgNC); (*ii*) a digital imaging technology; (*iii*) an ML-based image processing method.

In Chapter 5, we utilized our label-free multiplexed LSPR immunoassay to characterize the human T cell response toward differing aggregation stages of human islet amyloid polypeptide (hIAPP) and hIAPP interacted with gold nanoparticles stabilized by varying surfactant.

In Chapter 6, we concluded this work and showed the future direction of LSPR immunoassay.

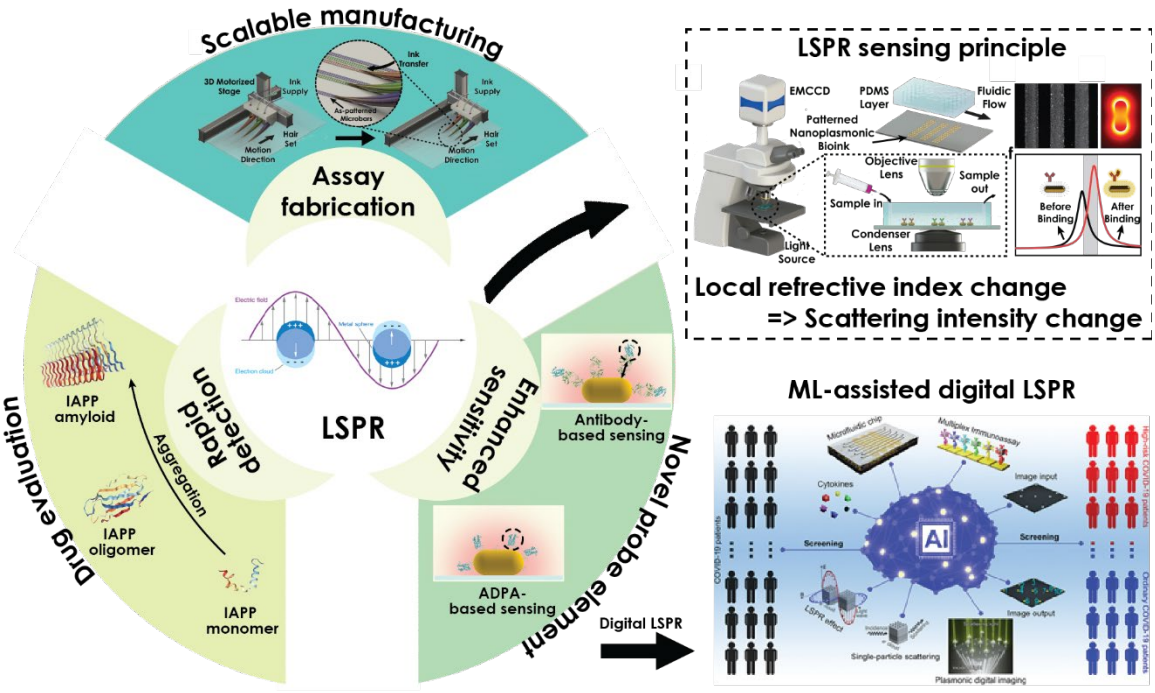

Figure 1.1. The structure of the dissertation. Top left: the sensing principle of LSPR biosensing platform. Right: This work consists of three parts: assay fabrication (top), enhanced sensitivity (bottom left), and rapid detection (bottom right). Four projects are introduced: scalable manufacturing (Top), novel probe element design (bottom left), ML-assisted digital LSPR (left), and novel drug evaluation (bottom right).

Chapter 2

Calligraphy of Nanoplasmonic Bioink-Based Multiplex Immunoassay for Tumor-Associated Macrophage (TAM) Immunophenotyping

2.1 Introduction

Immunomodulation has been suggested as a promising way to treat a broad spectrum of acute inflammatory diseases, or to an adverse immune response against transplant rejection.[67] The ultimate goal of such an approach is to either activate the specific immunity to battle cancer and chronic infection or to suppress the hyperinflammatory response towards implanted materials and tissues.[68] However, in surgical practice, the window for therapeutic intervention is limited, while modulating immune response requires a full mapping of the actual course of the acute-phase response.[67] Moreover, the simultaneous occurrence of the pro-inflammatory and anti-inflammatory response in the acute phase imposes challenges on therapeutic intervention. Therefore, rapid monitoring of the transient immune status in a multiplexed manner is of great clinical benefit.

Cytokines are small molecular weight proteins regulating the innate immune response in complex ways and have been quantified to reflect immune status. Currently, ELISA is the "gold standard" method for the quantification of cytokine. It involves multiple labeling and washing processes, which requires a minimum fabrication time of 24 hours and typically lacks multiplicity.[47] Fortunately, recent advances in nanotechnology have enabled the incorporation of nanomaterials into immunoassay.[15, 54] By doing so, the multiplexed detection is achieved by encoding the differing types of the target to the corresponding position and temporal resolution is improved by exploiting a label-free detection scheme with a superior sensing performance due to the reduced diffuse distance of analytes.[69] However, the fabrication of such immunoassays involving the immobilization of nanomaterials and functionalization of antibodies, which is typically 3 days, is still time-consuming, and more importantly, the need for complicated microfluidics control devices rendering it not suitable in urgent and resource-limited settings.

A variety of patterning techniques have been developed for the fabrication of nanomaterial-based immunoassays, such as microfluidics, microcontact printing, dip-pen nanolithography, and inkjet printing.[47, 70-72] On one hand, microfluidics and microcontact printing that utilizes the predesigned pattern on the polydimethylsiloxane (PDMS) mask layer require the prefabrication of a silicon master with the patterned relief structures on the surface, which is time-consuming and expensive. On the other hand, mask-free techniques, including dip-pen nanolithography and electron beam lithography, are typically limited by the low throughput and harsh processing conditions, i.e., high energy radiation and high vacuum.[73] Recently, Wang et al. reported a direct pattering strategy employing the hierarchically anisotropic microstructures of weasel hairs so that nanoparticle solution can be trapped between hairs.[74-75] Such an approach not only eliminates the need for fabricating masks but also exhibits excellent biocompatibility. However, it can only to exploited

for the patterning of nanoparticles and shows low throughput. Herein, we first developed a "ready-to-use" nanoplasmonic bioink, which is essentially an antibody conjugated gold nanorod (ab-AuNR) solution with outstanding printability, and then we demonstrated the direct patterning of multiple nanoplasmonic bioinks in a "one-step" manner. Together, it allows the fabrication of a multiplexed immunoassay with completely customized targets within 10 seconds and assay time less than 30 mins even in a resource-limited setting. We further showed the flexibility of finely tuning the barcode width, uniformity and sensor density by adjusting experimental parameters (weasel hair number, tilt angle and deformed distance). Finally, the sensing performance was evaluated in a mouse macrophage model.

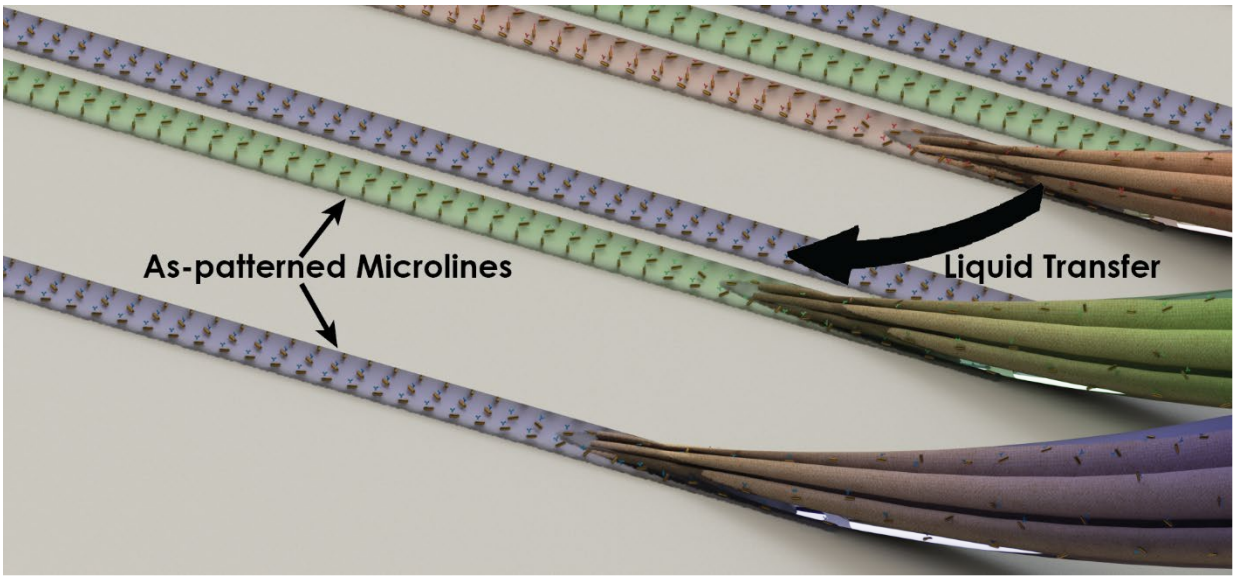

Figure 2.1. Schematic illustration of massively parallel immunoassay manufacturing technique utilizing the hierarchical anisotropic microstructures of weasel hair.

2.2 Materials and Methods

2.2.1 Synthesis of antibody-conjugated gold nanorods

4 mg/mL EDC (Thermo Scientific) and NHS (Thermo Scientific) were dissolved in deionized water and immediately added into 10 μL PEG-COOH-AuNR (nanoComposix, Inc.). After 30 min incubation, the resulting solution was centrifuged at 6000 rpm for 9 min. The supernatant was removed, and the precipitate was resuspended in 10 μL, 5 mM phosphate buffer (pH 7.4) with 0.5% PEG (Thermo Scientific). 1 μL, 50 μg/mL probe antibody was added into EDC/NHS activated nanoparticle solution. After one hour of incubation, the resulting solution was centrifuged again at 6000 rpm for 9 min. The supernatant was carefully removed and resuspended in 30 μL, 5 mM phosphate buffer (pH 7.4). 6 μL, 9 M betaine was added into 30 μL antibody conjugated gold nanorod.

2.2.2 APTES glass functionalization

The glass slide was first soaked in Piranha solution (H_2SO_4:H_2O_2 = 3:1) for 10 min. After deionized water rinsing, an ultrasonic bath of glass slide was conducted for 15 min. Then, the glass slide was rinsed again with deionized water and dried in an oven. The slide was then placed in a desiccator and 0.5 mL (3-Aminopropyl)triethoxysilane (APTES) (Thermo Scientific) liquid was added. The desiccator was vacuumed for 2 hours, followed by two-day incubation. To further fix the APTES molecules, APTES functionalized glass was placed in a 100 °C oven for 30 min.

2.2.3 PDMS fabrication

The PDMS prepolymer was prepared by mixing a silicone elastomer base agent with a curing agent at 10:1 (SYLGARD 184). The resulting prepolymer was transferred onto silicon mold

and cured at 80 °C for 4 hours. The cured PDMS layer with microfluidic flow patterning was then carefully peeled off and cut into multiple pieces for future use.

2.2.4 Characterization of nanoplasmonic bioink and as-patterned immunoassay

1 mL of freshly prepared sample was added into disposable cuvettes (Semi-Macro, VWR), and then corresponding extinction spectrum was obtained on a UV/Vis spectrometer (Ultrospec 2100 pro, Amersham Biosciences). 0.2 mL of freshly prepared nanoplasmonic bioink was diluted by 0.6 mL deionized water and then transferred in capillary zeta cell (Malvern). The cell was stabilized in the zetasizer (Zetasizer Nano ZS 90) for 3 mins, and then zeta potential and hydrodynamic size of nanoplasmonic bioink were recorded. A drop of freshly prepared nanoplasmonic bioink was blotted on a copper grid and 1% uranyl acetate was applied for enhanced image contrast. Transmission electron microscope (TEM) images were taken by a Zeiss EM10 transmission electron microscope at 200 kV. The morphology of the as-patterning barcode was analyzed using a KEOL JSM-7000F scanning electron microscope (SEM).

2.2.5 Macrophage culture and polarization

Raw 264.7 was firstly purchased from ATCC and then cultured in Dulbecco's modified eagle medium (DMEM) medium (BD bioscience), contained 10% fetal bovine serum (FBS) (ThermoFisher) and 100 U per ml of penicillin-streptomycin (ThermoFisher) in a 5% CO_2 humidified incubator at 37°C. For the polarization, RAW 264.7 cells were seeded in a density of 5 x 10^4 cells per well in a 12 well plate and were allowed to reach 50% sub confluency. Then cells were differentiated with 100ng/mL lipopolysaccharides (LPS) (InvivoGen) or 40ng/mL Recombinant Murine IL-4 (PEPROTECH) for 24 hours, following the cells were treated with 30ug/mL minocycline(fisher scientific) or 100 μM R848 (ASK Scientific) to re-educate the

already differentiated cells or prevent the further differentiation for another 24 hours. Then the cell culture medium in different treatment groups was collected and stored separately for future use.

2.2.6 Patterning of nanoplasmonic bioink and fabrication of LSPR immunoassay

The weasel hairs were carefully selected from the painting brushes (ZHOUXY Ltd.) and the different number of weasel hairs were parallelly fixed in a stainless-steel needle (304 stainless steel, McMASTER-CARR). Three sets of weasel hairs were fixed on the holder, which was attached to a 3-dimensional (3D) motorized stage. Nanoplasmonic bioink was continuously supplied through soft plastic tubing (McMASTER-CARR). Multiple nanoplasmonic bioinks were simultaneously patterned on APTES functionalization glass substrate by programming the motion of three axes. As-patterned LSPR chip was incubated for 2 hours, allowing negatively charged antibody-conjugated gold nanorods attracted on positively charged APTES functionalized glass. A PDMS layer with microfluidic channels was applied onto an as-patterning LSPR chip such that the direction of nanoplasmonic bioink barcodes on APTES functionalized glass was perpendicular to the direction of microfluidic channels on the PDMS layer.

2.2.7 Multiplexed LSPR assay protocol

The constructed LSPR immunoassay was then mounted on the motorized stage (ProScanIII, Prior Scientific, Rockland, MA) for positioning of the sensing area. Two droplets of type A immersion oil (Nikon Instrument Inc.) were applied to the condenser lens (Nikon Instrument Inc.). A condenser lens was then attached to the back of the LSPR chip so that the incident light was illuminated on the LSPR chip. Only the light scattered on gold nanorods surface went through a 10× objective lens (Nikon Instrument Inc.) and then filtered by a band-pass filter (670 ± 25 nm, Chroma). The filtered light was recorded by an electron-multiplying charge-coupled device

(EMCCD) camera (mold) and scattering light intensities on each barcode were analyzed by the Matlab program in real-time. Cell culture medium was immediately loaded by a syringe pump at 1 μL/min for 8 mins to wash away unbounded antibody-conjugated gold nanorods and passivate the immunoassay. Then, the cell culture medium was loaded at 0.2 μL/min to stabilize the immunoassay so that the intensity variations solely resulted from the binding events between the cytokines and corresponding antibodies. IL-6, TNF-α, and transforming growth factor-beta (TGF-β) cytokines spiked in cell medium with known concentrations were prepared in advance. Once scattering light intensity stabilized, the standard spiked-in solution was injected into each microfluidic channel by a syringe pump. The optical signal was recorded by the EMCCD camera and the scattering light intensity variation on each sensing area was automatically analyzed by our customized Matlab program. Macrophage samples were sensed in the same protocol.

2.2.8 ELISA validation of macrophage samples

Mouse IL-6 ELISA kit and mouse TNF-α ELISA kit were purchased from affymetrix eBioscience and used as manufacturer's instructions. Briefly, microwell strips were thoroughly washed twice and emptied before measurements. 50 μL of standards and macrophage samples were added to microwell in triplicate, followed by 50 μL biotin-conjugate. After 2-hour incubation on the microplate shaker, microwells were washed six times, and then 100 μL Streptavidin-horseradish peroxidase (HRP) was added and incubated for 1 hour with shaking. Resulted microwells were washed six times, followed by the application of 100 μL 3,3′,5,5′-Tetramethylbenzidine (TMB) substrate solution. After 30 mins incubation, 100 μL stop solution was added and the absorbance of each microwell was read immediately by a plate reader at 450 nm. Mouse TGF-β ELISA kit (Invitrogen) was used according to the manufacturer's instructions. 50 μL of 0.1 M HCl was first added to 50 μL macrophage samples. After 1-hour of incubation, 50

μL of 0.1 M NaOH was injected to neutralize the samples. Microwells were washed twice and emptied on a paper towel. 40 μL pretreated samples along with 60 μL assay buffer were added into microwells in triplicate. Meanwhile, 100 μL standards were added to standard microwells in triplicate. After 2-hour incubation, all microwells were washed thoroughly five times, followed by pipetting 100 μL of biotin-conjugate. After another 1-hour incubation, five times washing was performed and then 100 μL Streptavidin-HRP was injected. Incubated for 30 mins, microwells were washed, followed by the application of 100 μL TMB substrate solution. After 30 min incubation, the enzyme reaction was terminated by adding 100 μL stop solution and absorbance was determined by a plate reader.

2.2.9 Finite element analysis (FEA)

The scattering spectrum of AuNR and 2-dimensional (2D) spatial distribution of electromagnetic field was calculated by finite element method using commercial multiphysics simulation software (COMSOL). Briefly, an AuNR (41 nm × 17 nm) was defined, and a far-field domain with a radius of half wavelength of incident light was set. After binding, the cytokine captured by the antibody was simplified as a protein shell with a thickness of 2 nm. On the top of the far-field domain, a perfectly matched layer that was served as a boundary condition in our simulation was constructed. Polarized incident light was defined in parallel with the longitudinal direction of AuNR. The scattering cross-section of AuNR was denoted as C_{SCS} and calculated by the following equation:

$$C_{scs} = \int \frac{I_{AuNR}}{I_{background}} d\Omega \quad (1)$$

The relative permittivity of water and protein was set as 1.77 and 2.55, respectively. The frequency-dependent dielectric constant of gold was calculated from the Lorentz-Drude model.

2.3 Results and Discussion

2.3.1 Preparation of nanoplasmonic bioink

We developed a solution-based conjugation method for the synthesis of nanoplasmonic bioink (**Figure 2.2a**). Due to the relatively high ionic strength solution typically involved in the surface functionalization process, it is critical to not agglomerate nanoparticles while preserving the functionality of biomolecular probes. Therefore, we employed polyethylene glycol-carboxyl (PEG-COOH) capped gold nanorod, in which PEG provided steric stability in solution. PEG-COOH-AuNR surface was first activated through EDC/NHS coupling chemistry, and then Antibody was conjugated. As a facile yet general method, we demonstrated the conjugation of three different antibodies, i.e., anti-IL-6, anti-TNF-α, and anti-TGF-β. PEG-COOH-AuNR and corresponding conjugates were firstly characterized by TEM. **Figure 2.2b** showed the morphology of PEG-COOH-AuNR with a dimension of 41 nm × 17 nm. After conjugation, antibodies were successfully attached to the nanorod surface, as evidenced by the shaded area around nanorods (**Figure 2.2c**). The dispersity of as-synthesized conjugates was examined by ultraviolet-visible (UV-Vis) spectroscopy. As revealed in **Table 2.1**, the original extinction peak for PEG-COOH-AuNR was located at 662 nm, and after conjugation, peaks slightly red-shifted, indicating successful conjugation of antibody and excellent mono-dispersity.[15] The PEG-COOH-AuNR was also characterized by dynamic light scattering (DLS) to further confirm the antibody conjugation. A hydrodynamic size of 37.82 nm was observed for PEG-COOH-AuNR, while after conjugation, the larger sizes suggested the existence of an antibody layer outside. Meanwhile, as showed by Zeta potential measurements, the net negative charge remained in all samples, thus that conjugates can be immobilized on the positively charged substrate via electrostatic interaction. Additionally, the evaporation behavior of nanoplasmonic bioink was modulated by introducing betaine, a

naturally existing substance, while morphology, peak location, and surface charge were not altered. In **Figure 2.2d**, initial evaporation behavior was not affected when betaine was added, but the evaporation rate significantly slowed from 30 mins and completely ceased at 43 min with around 20% solution remained, which is beneficial to suppress the well-known coffee-ring effect.[76]

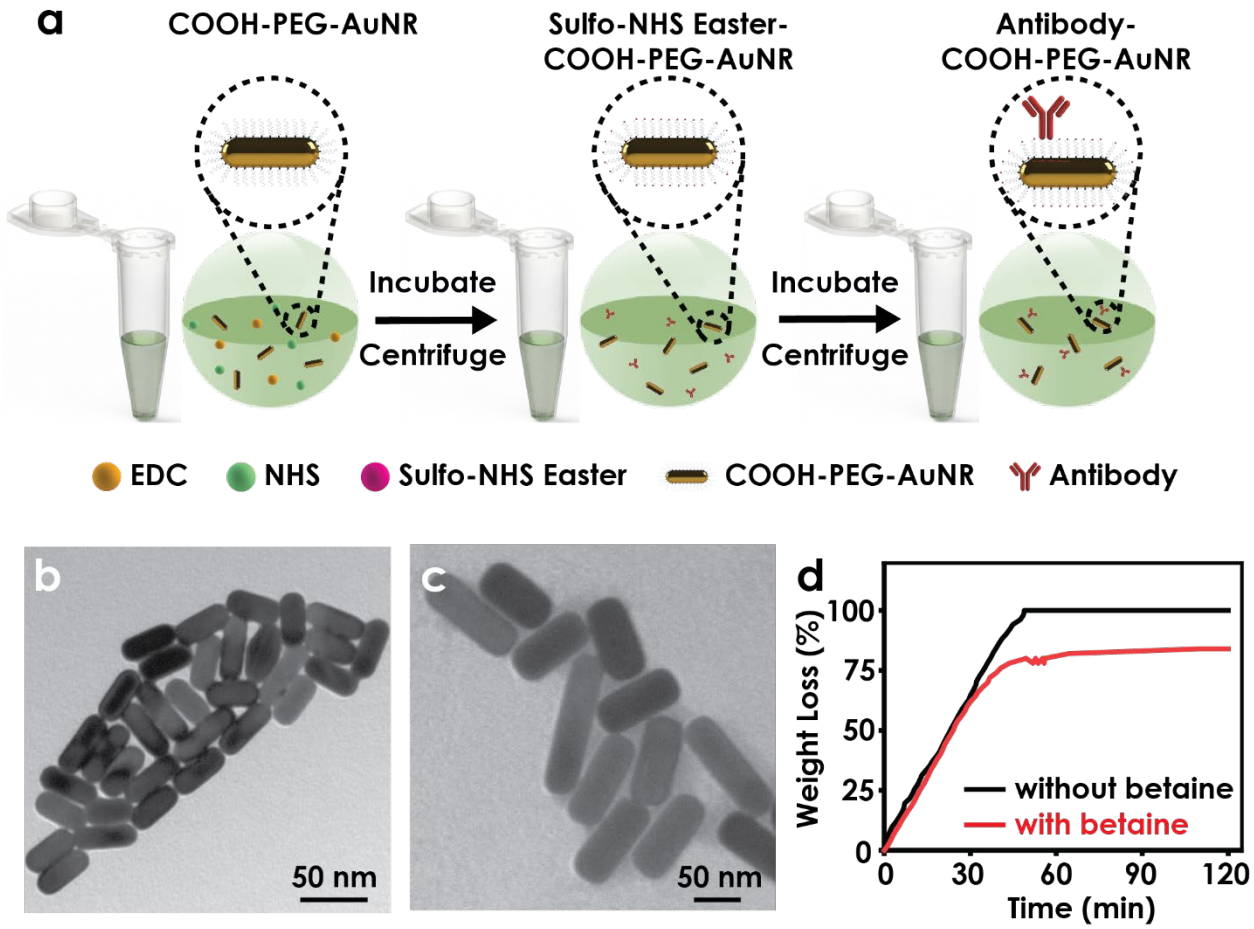

Figure 2.2 Synthesis of nanoplasmonic bioink. (a) Schematic illustration of synthesis strategy of nanoplasmonic bioink. TEM images of PEG-COOH-AuNR (b) and anti-IL-6 conjugated PEG-COOH-AuNR (c). (d) The effect of betaine on nanoplasmonic bioink evaporation behavior.

Table 2.1 The wavelength, hydrodynamic size and zeta potential of AuNR and three types of antibody-conjugated AuNR.

Parameters	AuNR	Anti-IL-6-AuNR	Anti-IL-6-AuNR with betaine	Anti-TNF-α-AuNR	Anti-TNF-α-AuNR with betaine	Anti-TGF-β-AuNR	Anti-TGF-β-AuNR with betaine
λ (nm)	662.67 ± 0.02	663.26 ± 0.02	663.47 ± 0.02	663.45 ± 0.01	663.62 ± 0.02	663.38 ± 0.02	663.61 ± 0.05
Size (nm)	37.82 ± 0.37	42.18 ± 0.76	42.56 ± 0.20	43.38 ± 0.48	44.96 ± 0.09	40.93 ± 0.76	43.58 ± 0.20
Zeta Potential (mv)	-32.23 ± 0.74	-31.93 ± 1.10	-36.37 ± 0.99	-27.60 ± 1.31	-29.1 ± 0.95	-34.37 ± 2.02	-37.00 ±1.47

2.3.2 Development of massively parallel immunoassay manufacturing technique

We further designed a homemade motorized stage enabling programmable motion along three axes. **Figure 2.3a-b** is the photographs of our patterning system, including a 3D stage, syringe pumps, a laptop and three sets of weasel hairs. As illustrated in **Figure 2.3c**, a glass substrate was placed on a 3D printed glass holder. Weasel hairs were firmly clamped by plastic tubing and stainless-steel needle, while corresponding nanoplasmonic bioinks were continuously supplied from the top. Wang *et al* reported the unique multi-scale microstructures of weasel hairs enabling fine manipulation of low-viscosity liquid.[74] The liquid can be held among weasel hairs due to the balance between gravitational force and curvature gradient aroused Laplace pressure.[75] Once deformed, such balanced was perturbed so that liquid can be controllably on substrate. In this chapter, to demonstrate the utilization of weasel hair as a template-free patterning technique, we firstly patterned three different gold nanorod solutions, i.e., citrate capped gold nanorod (Cit-AuNR), hexadecyltrimethylammonium bromide capped gold nanorod (CTAB-AuNR) and PEG-COOH capped gold nanorod (PEG-COOH-AuNR) on APTES functionalized glass substrate. **Figure 2.3d-f** showed the dark-field images of as-patterned gold nanorod barcode with excellent uniformity, suggesting that our technique can be a general patterning method. Besides, the use of anisotropic gold nanorod typically occurred during the evaporation process was significantly

suppressed as the outward capillary flow was resisted by the long-ranged interparticle capillary interaction aroused from anisotropic nanorods.[77]

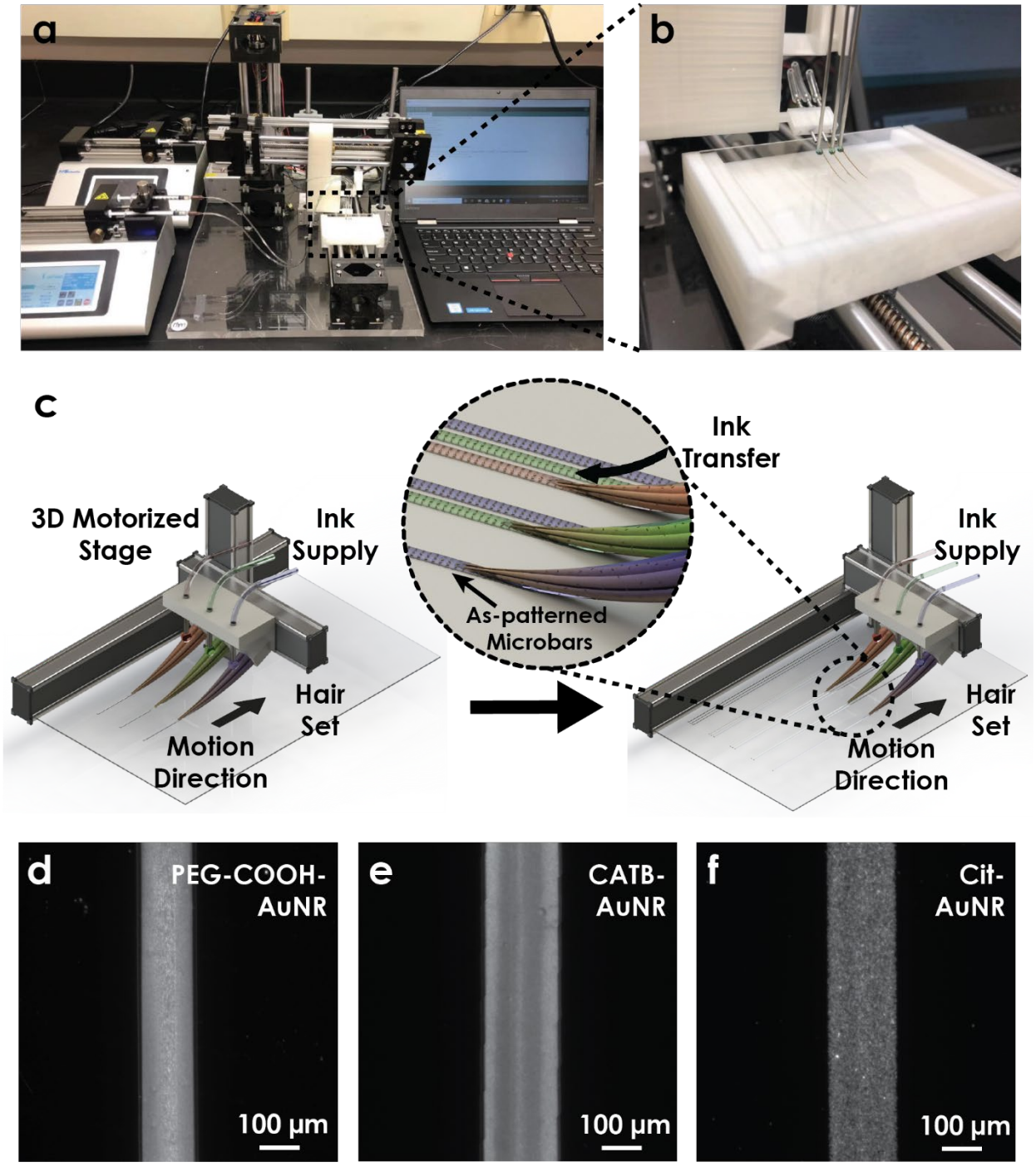

Figure 2.3 Scalable manufacturing of multiplexed immunoassay utilizing weasel hair. (a-b) Photograph of patterning system that was constituted by three components: a homemade 3D stage, a laptop, and syringe pumps. (c) Illustration of patterning system. The dark-field images of as-patterned PEG-COOH-AuNR (d), CTAB-AuNR (e), and Cit-AuNR (f) barcode.

We then optimized barcode width, uniformity, and nanoparticle density by finely manipulating three key parameters, i.e., fiber number (N), tilt angle (θ), and deformed distance (ΔD) (**Figure 2.4**). Since the multiplexity was achieved by encoding different nanoplasmonic bioinks onto spatially encoded barcodes, the width of the barcode essentially defines the number of targets detected. Ideally, a greater number of targets detected on a unit area, i.e., smaller barcode width, is desired. Additionally, the sensing performance was greatly affected by nanoparticle density, indicated by the average scattering light intensity in the dark-field scheme. The higher nanoparticle density can cause plasmonic coupling and a broadened scattering peak in the real-time measurement, while the lower nanoparticle density sacrificed the sensitivity and dynamic range due to insufficient binding sites. The uniformity reflected the distribution of nanoparticles on the barcode, as quantified by the standard deviation (STD) of the scattering light intensity from each pixel. **Figure 2.4a-d** showed the dark-field images of as-patterned barcodes by utilizing varying number of weasel hairs. As revealed by the black curve in **Figure 2.4e**, the fewer weasel hairs involved, the lower density of nanoparticle was resulted because the insufficient volume of nanoplasmonic bioink was held among weasel hairs and transferred onto substrate. Interestingly, the minimized standard deviation of scattering light intensity was obtained when 5 weasel hairs were utilized, suggesting the most controllable liquid transfer and evaporation process (**Figure 2.4e**, olive curve). When more weasel hairs were involved, a noticeable coffee-ring effect was observed, while fewer hairs resulted in scattered bright areas. In **Figure 2.4f-i**, the critical condition that was defined by the smallest deformed distance necessary to transfer liquid onto a glass substrate was investigated. **Figure 2.4j** showed a negative correlation between the weasel hair number and critical deformed distance, implying a lower extent of deformation required as more nanoplasmonic bioink held (black curve), while the largest barcode width was obtained at 5 (olive

curve). Taken together, the optimal barcode patterning quality was achieved when five weasel hairs were involved. By fixing the weasel hair number at 5, the flexibility of the calligraphy patterning technique was demonstrated by adjusting the tilt angle and deformed distance. As illustrated in **Figure 2.4k-l**, tilt angle (θ) was defined by the angle between weasel hair and substrate without deformation, while the deformed distance (ΔD) was the difference of initial distance (D_i) and final distance (D_f). **Figure 2.4m** exhibited a near-linear relationship between average scattering intensity and deformed distance, explained by the loss of Laplace pressure that was originated from the larger curvature gradient near the weasel hair tip. Accordingly, when weasel hairs were deformed during the patterning process, the upward Laplace force was perturbed, so nanoplasmonic bioink was controllably transferred onto glass substrate solely propelled by gravitational force. In this case, the larger deformed distance resulted in the smaller Laplace pressure, suggesting more gold nanorods being transferred on the substrate. On the other hand, when the deformed distance was fixed, a lower tilt angle resulted in a higher scattering intensity because the low tilt angle with a large deformed distance was geometrically equivalent to a high tilt angle with a small deformed distance. The similar trend can be observed from **Figure 2.4n** that larger deformed distance led to more nanoplasmonic bioink transferred but more random evaporation process, which eventually caused noticeable coffee-ring effect and scattered bright spots. **Figure 2.4o** reflected the larger width of the barcode resulted from the larger deformed distance and lower tilt angle. Therefore, our results revealed that weasel hair-based patterning technique, as a facile yet general method, offered the great flexibility to systematically control the barcode width, uniformity, and nanoplasmonic bioink density so that can be easily applied to different practical settings.

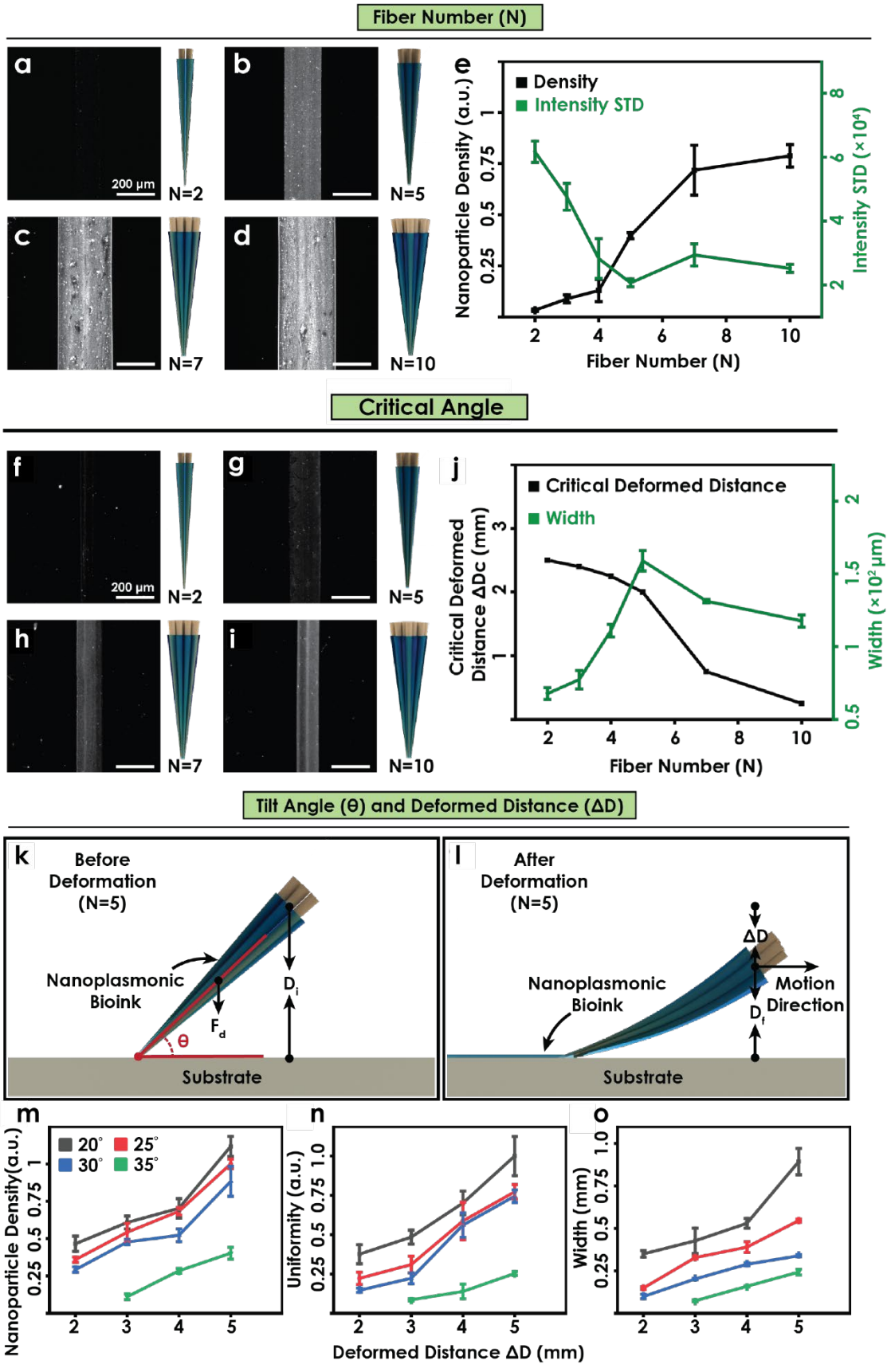
Fiber Number (N)
a
200 μm
N=2
b
N=5
c
N=7
d
N=10
e
Density
Intensity STD
Nanoparticle Density (a.u.)
Intensity STD (×10⁴)
Fiber Number (N)
Critical Angle
f
200 μm
N=2
g
N=5
h
N=7
i
N=10
j
Critical Deformed Distance
Width
Critical Deformed Distance ΔDc (mm)
Width (×10² μm)
Fiber Number (N)
Tilt Angle (θ) and Deformed Distance (ΔD)
k
Before Deformation (N=5)
Nanoplasmonic Bioink
D_i
F_d
θ
Substrate
l
After Deformation (N=5)
ΔD
Nanoplasmonic Bioink
Motion Direction
D_f
Substrate
m
20° 25° 30° 35°
Nanoparticle Density(a.u.)
n
Uniformity (a.u.)
o
Width (mm)
Deformed Distance ΔD (mm)

Figure 2.4 Optimization of massively parallel immunoassay manufacturing technique using weasel hair. (a-d) The dark-field images of as-patterned barcodes by differing numbers of weasel hairs. (e) The analysis of patterning quality resulted from the number of weasel hair employed. The density of gold nanorod (black curve) was indicated by the average scattering intensity on barcode, while uniformity was characterized by the standard deviation of scattering intensity (olive curve). (f-i) The dark-field images of barcode patterned by varying number of weasel hairs under critical condition. (j) The analysis of patterning quality resulted from the number of weasel hair employed. The critical deformed distance (black curve) is defined by the smallest deformed distance necessary to transfer liquid onto glass substrate. The width of patterned barcode was plotted in olive. (k-o) The influence of tilt angle and deformed distance when weasel hair number was fixed at 5. The dependence of average intensity (m), uniformity (q), and width (r) with tilt angle and deformed distance.

2.3.3 Characterization of patterned barcode

Associated with nanoplasmonic bioink, we demonstrated the one-step massively parallel fabrication of multiplexed LPSR immunoassay by our weasel hair-based patterning technique. To immobilize gold nanorods on substrate, in this chapter, we employed a negatively charged gold nanorod (PEG-COOH-AuNR) with a positively charged glass substrate (APTES-glass), therefore that gold nanorods can be immobilized through electrostatic interaction. Anti-IL-6 was firstly conjugated to PEG-COOH-AuNRs in solution through standard EDC/NHS coupling chemistry and 9 μM betaine was then added to modulate the evaporation behavior and form nanoplasmonic bioink. As patterned anti-IL-6-PEG-COOH-AuNR barcode was characterized by dark-field microscope, SEM, and scattering-type scanning near-field optical microscopy (s-SNOM). A width of 132 μm was shown on the SEM image (**Figure 2.5a**) and dark-field image (**Figure 2.5d**). Anti-

IL-6-PEG-COOH-AuNRs were homogeneously distributed, and no obvious aggregation was observed (**Figure 2.5b**). The well-defined barcode edge with nanoscale accuracy was revealed (**Figure 2.5c**), rendering the capability of precisely patterning nanoplasmonic bioink on the location of interests. The noteworthy, the coffee-ring effect was significantly suppressed due to the use of anisotropic gold nanorods resisting the long-ranged interparticle capillary interactions and the addition of betaine modulating the evaporation process. The patterning quality was then characterized by s-SNOM, optical microscopy provided complex optical properties of a sample with a nanoscale resolution.[78] **Figure 2.5e-g** showed the isolated distribution of anti-IL-6-PEG-COOH-AuNRs, consistent with SEM results. A brighter shell (antibody layer) against a darker core (AuNR) was observed from **Figure 2.5h**, indicating the successful antibody conjugation on the AuNR surface. To further confirm the antibody layer, optical amplitude information was analyzed from s-SNOM irradiating incident infrared (IR) light at different frequencies. 1640 cm^{-1} corresponded to the characteristic made I band of protein, therefore we performed s-SNOM imaging at 1530 cm^{-1}, 1600 cm^{-1}, 1640 $cm^{-1,}$ and 1711 cm^{-1}. The strongest optical amplitude signal was observed from 1640 cm^{-1}, while 1600 cm^{-1} exhibited the weakest amplitude response, in accord with literature results.[79]

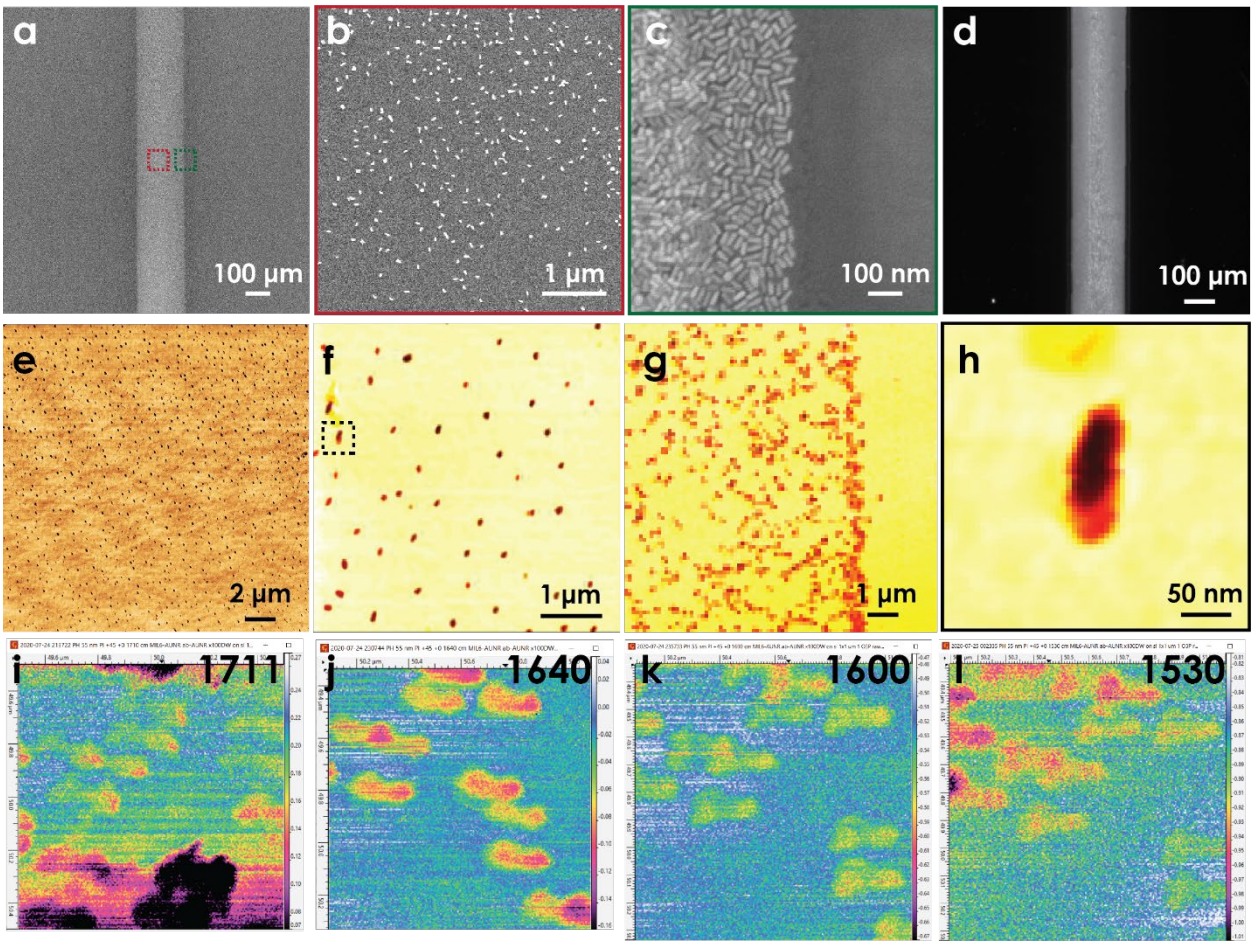

Figure 2.5 Characterization of the patterned barcode. (a) SEM image of a patterned barcode. (b-c) Magnified SEM images revealed uniformly distributed anti-IL-6-PEG-COOH-AuNRs and a well-defined edge. (d) Dark-field image of a patterned barcode. (e) s-SNOM image (optical phase) of patterned anti-IL-6-PEG-COOH-AuNRs. (f-g) Magnified s-SNOM images showed isolated anti-IL-6-PEG-COOH-AuNRs on the barcode and a well-defined edge. (h) Magnified s-SNOM images showed a typically anti-IL-6-PEG-COOH-AuNR with a dark core (AuNR) and a shielded shell (antibody). (i-l) s-SNOM images (optical amplitude) of patterned anti-IL-6-PEG-COOH-AuNRs at different frequencies.

2.3.4 LSPR assay protocol

Current plasmonic immunoassays that involved step-by-step patterning strategy, requiring a total fabrication time of at least 24 hours, fall short of meeting "on-site" routine use requirements, considering the limited window for therapeutic intervention. There is a critical need to develop a ready-to-use multiplexed immunoassay. Associated with nanoplasmonic bioink, our weasel hair-based patterning technique enabled the fabrication of multiplexed plasmonic immunoassay in a "one-step" manner, thus shortening the patterning time to less than 1 min. Notably, the targets of interest are completely customizable and after a 2-hour incubation. Such multiplexed immunoassay is ready to use even in a "resource-limited" setting. Taking advantage of our recently developed intensity-based LSPR real-time imaging system, allowing near-real-time and sensitive detection of multiple cytokines, we first calibrated our plasmonic immunoassay to three targets: IL-6, TNF-α, and TGF-β.[6, 15] **Figure 2.6a** illustrated the setup of intensity-based LSPR biosensing platform. Briefly, a piece of PDMS layer with microfluidic channels on the bottom was placed on as-fabricated plasmonic chip (**Figure 2.6b**), and such LSPR immunoassay was mounted on a dark-field optical microscope. Three types of nanoplasmonic bioinks, i.e., anti-IL-6-PEG-COOH-AuNR, anti-TNF-α- PEG-COOH-AuNR, and anti-TGF-β- PEG-COOH-AuNR, were patterned by our weasel hair-based patterning technique (**Figure 2.6c**). Each sample loading allowed the simultaneous measurement of three biomarkers in triplicate. During the measurement, samples were injected through microfluidic channels, so specific cytokines were captured by corresponding antibodies, and the time-course scattering light intensity with a temporal resolution of 10 seconds, was collected by an EMCCD camera, and automatically analyzed by a customized Matlab algorithm that allowed the high throughput translating of location encoded LSPR signal. According to our previous works, the binding events between cytokine and antibody led to a red-shifted scattering spectrum and increased scattering intensity.[6, 15] The relative variation of

scattering light intensity ($\Delta I/I_i$) was correlated to cytokine concentration. We spiked cytokines with known concentrations (500, 1000, 2000, 5000, 10000 pg/mL) in a cell culture medium and loaded them into nanoplasmonic immunoassay. The LSPR signals of the corresponding sample were analyzed and illustrated in **Figure 2.6d**. Based on the intensity mapping, three calibration curves were thereby constructed (**Figure 2.6e**). The limit of detection for IL-6, TNF-α, and TGF-β was 40.93, 69.15, and 93.67 pg/mL, respectively. Furthermore, by detecting samples by different sensing methods (two unknown macrophage samples and three spiked-in samples with known analyte concentration), we compared our LSPR results with ELISA results and observed a great linear correlation of 0.9817 (**Figure 2.6f**).

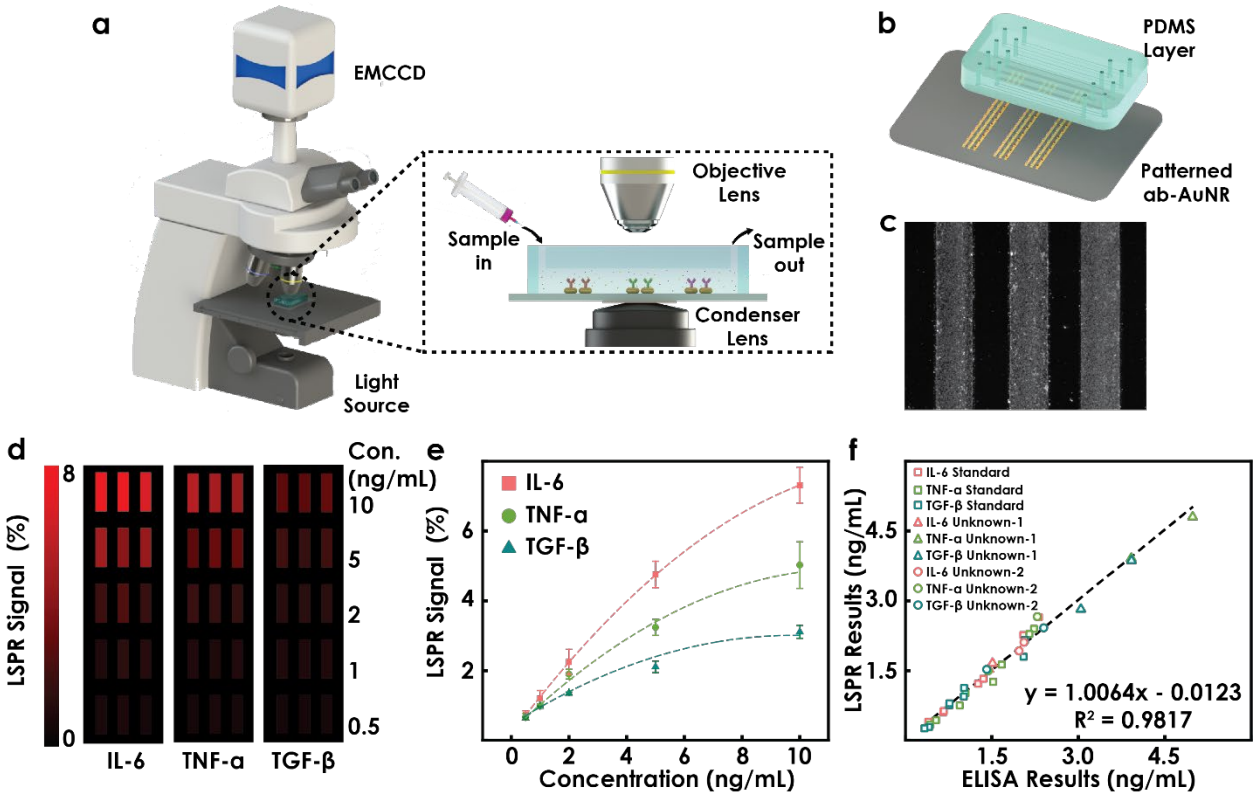

Figure 2.6 LSPR assay protocol. (a-b) LSPR biosensing platform. As-patterned chip was placed under a dark-field microscope. A piece of PDMS layer with microfluidic channels on the bottom was applied to the chip. (c) A representative dark-field image of as-patterned barcodes for LSPR sensing. (d) The scattering intensity mapping of sensing spots on LSPR immunoassay. Known concentrations of mouse IL-6, TNF-α, and TGF-β were spiked in cell culture medium and injected into microfluidic channels. The images were taken every 10 seconds for 30 minutes. (e) Calibration curves of IL-6, TNF-α, and TGF-β were calculated from LSPR barcode intensity mapping in (d). The limit of detection for IL-6, TNF-α, and TGF-β were 40.93, 69.15, and 93.67 pg/mL, respectively. (f) The correlation between LSPR results and ELISA results of three samples with known cytokine concentrations and two samples with unknown cytokine concentrations.

2.3.5 Immunophenotyping of mouse macrophages under different stimulations and treatments

To validate the practical use of our multiplexed plasmonic immunoassay, a mouse macrophage model was selected. Macrophages are multifunctional cells with heterogeneous subpopulations drawn from bone marrow and yolk sac progenitors and play an indispensable role in triggering, instructing, and terminating the adaptive immune response through the release of cytokines.[80-81] They are phenotypically polarized into two extreme subtypes, i.e. classically (M1) and alternatively (M2) activated macrophages.[82] The M1 phenotypes encourage inflammation and inhibit tumor progression by secreting high levels of pro-inflammatory cytokines, including IL-6 and TNF-α, while M2 phenotypes inhibit inflammation and promote the proliferation of tumor through the release of anti-inflammatory cytokines, such as TGF-β.[54] As shown in **Figure 2.7a**, the original macrophage (M0) was first polarized into M1 and M2 phenotype by LPS and IL-4, respectively. Minocycline, a synthetic tetracycline with anti-inflammation and antiviral properties, was then added as an immunomodulator to suppress the hyperinflammatory response of M1 macrophage samples.[83] On the other hand, M2 macrophage samples were treated by a synthetic imidazoquinoline-like drug resiquimod (R848) to promote an inflammatory response.[84] As indicated in **Figure 2.6b-d**, LPS-stimulated macrophage expressed a higher level of all three cytokines, but a more significant difference was observed from pro-inflammatory cytokine IL-6 and TNF-α. Minocycline treatment, as expected, led to a suppressed secretion level of both pro-inflammatory cytokines and a higher TGF-β concentration. Interestingly, as evidenced by the suppressed level of pro-inflammatory cytokines and upregulated anti-inflammatory cytokine, IL-4 that has long been characterized as a promotor of alternatively activated macrophage tilted the polarization from M1 to M2, consistent with recent results.[85-86] In contrast, a significantly increased expression of anti-inflammatory cytokine TGF-β indicated that M0 macrophages were

successfully polarized into M2 with the IL-4 stimulation. Upregulated secretion level of pro-inflammatory cytokines and suppressed level of TGF-β was observed, rendering the promoted inflammatory response. All the macrophage samples were independently tested by ELISA and the results were in good agreement (**Figure 2.6e-g**). Therefore, our multiplexed immunoassay fabricated by one-step weasel hair-based patterning technique exhibited excellent sensing performance and were well-suited for point-of-care inflammation-related disease diagnosis and routinely immune status monitoring.

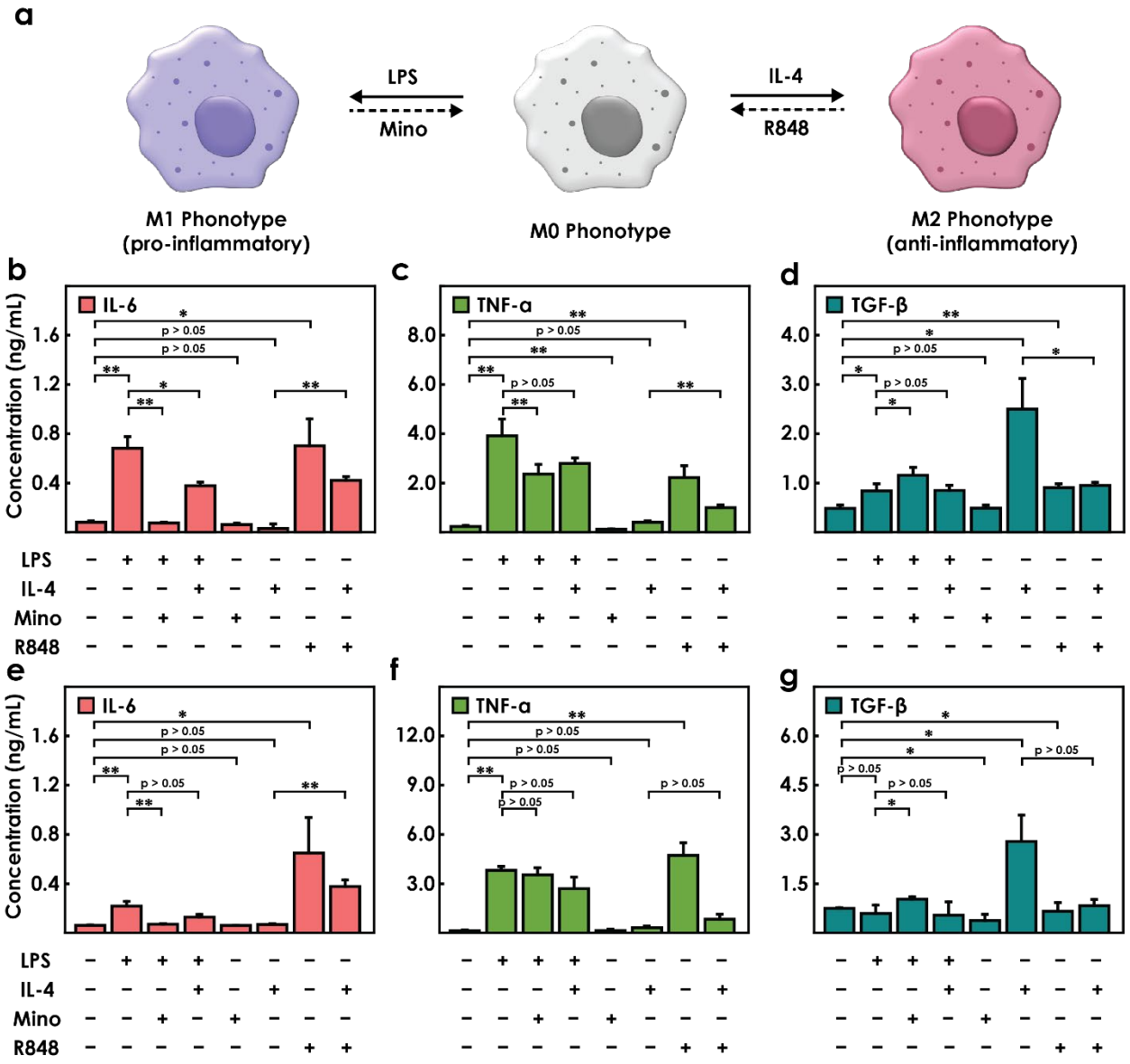

Figure 2.7 Macrophage immunophenotyping under different stimulations and treatments. (a) The schematic illustration of macrophage polarization and immunomodulatory treatment. Primary macrophages (M0) were polarized by LPS and IL-4. The LPS stimulated macrophages (M1) were then treated by minocycline. The IL-4 stimulated macrophages (M2) were treated by R848. (b-d) IL-6, TNF-α, and TGF-β secretion profiles of macrophage samples under different treatment conditions measured by LSPR immunoassay. (e-g) IL-6, TNF-α, and TGF-β secretion profiles of macrophage samples under different treatment conditions measured by commercialized ELISA.

2.4 Conclusion

In summary, we first developed a general and facile method for the synthesis of nanoplasmonic bioink. Associated with weasel hair-based patterning technique, multiple nanoplasmonic bioinks can be directly patterned on the glass substrate in a “one-step” manner, dramatically shortening the fabrication time of immunoassay to less than 1 min. Then we systematically demonstrated the flexibility of finely manipulating barcode width, uniformity, and nanoplasmonic bioink density by controlling the number of weasel hair, tilt angle, and deformed distance. Finally, the sensing performance of our immunoassay was assessed in a macrophage model, rendering it a powerful tool for point-of-care inflammation-related disease diagnosis and routinely immune status monitoring.

Chapter 3

Antibody-Derived Peptide Aptamer (ADPA) for Enhanced Nanoplasmonic Immunosensing

3.1 Introduction

Cytokines are low molecular weight signaling proteins critical in regulating cell growth, differentiation, and immune responsiveness.[87] Rapid and precise quantification of cytokines in a small sample consumption offers clinically valuable information, given the highly dynamic nature of immune status, for viral sepsis, cancer, and autoimmune diseases.[47] A newly emerged COVID-19 caused by SARS-CoV-2 induces the hyper-inflammatory response, a major cause of disease severity and death.[63] Recent studies suggested the elevated serum levels of inflammatory cytokines such as IL-6 are strong and independent predictors of disease severity, and the key to effective medication and treatment is timing and dosage of the drug.[88-90] This has necessitated the profiling of cytokine biomarkers in a near-real-time manner for guided therapeutic interventions.[91-92] However, the current gold standard method for cytokine quantification, ELISA, requires a minimum assay time of 3-8 h because of multiple sample labeling and washing processes.[47] Furthermore, a large sample consumption (0.5-2 mL) is required for an absorbance-based detection scheme so that a sufficient signal-to-noise ratio can be generated.[93] Hence, an urgent need remains

in the development of a novel immunoassay that allows rapid and accurate cytokine detection in a small sample volume.

In contrast to traditional label-based immunoassays, label-free techniques that eliminate the use of secondary antibodies are advantageous for high-speed cytokine detection.[94-96] Among these, nanoplasmonic biosensing platforms based on LSPR have attracted accumulating attention.[6, 15] Integrated with a functional microfluidic device, LSPR immunoassays show great promise in the rapid and sensitive detection of practical biomarkers in the miniature quantity of samples.[54, 97] Unlike surface plasmon resonance (SPR), where propagating surface plasmons sense the bulk dielectric environment variation within a range of up to 600-1000 nm, surface plasmons in LSPR are confined to the nanoparticle surface, thus unique for probing refractive index changes in a highly localized environment (~ 20 nm) around the plasmonic nanoparticle surface.[98-99] Yet, despite its great potentials, the LOD of the current antibody-based LSPR immunoassay was typically over 10 pg/mL, while serum predictor cytokine levels, i.e. IL-6, found in 1,484 hospitalized COVID-19 patients spanned from 1.6 pg/mL to 4823 pg/mL.[6, 15, 63] As such, current label-free nanoplasmonic biosensors based on LSRP cannot afford sufficient sensitivity for the detection of low-concentration cytokines.

Antibodies are Y-shaped proteins to recognize and neutralize foreign substances, also known as antigens.[100] Due to their high affinities and specificities against selected targets, antibody-based biosensors are routinely harnessed in the analysis of complex biological samples.[6, 15, 101] However, the generation of antibodies that requires antigens preparation and animal immunization is costly, while the heat-induced denaturation also poses a limited shelf life.[102-103] Furthermore, the considerable dimension (~ 150 kDa) of antibodies can be disadvantageous in certain scenarios, such as LSPR based biosensing scheme, where the strength of the enhanced electric field is greatest

at the nanoparticle-medium interface and decays exponentially into the medium.[98, 104] As a result, a thick recognition layer formed by covalently conjugated antibodies covers a large fraction of local sensing volume, thereby an antibody-antigen binding event being probed by a less sensitive evanescent field.[98] As an alternative to conventional antibodies, nanobodies, a single domain of camelid heavy-chain antibodies with a molecular weight of 15 kDa, show full capacity to bind target proteins with high affinity.[105] Peptide aptamers derived from directed-evolution have emerged as another alternative, in which a short amino acid sequence with high affinity against the selected target is embedded in an inert peptide scaffold.[103, 106] Despite their simple and robust architecture, the expensive and time-consuming generation of nanobodies and peptide aptamers, in a manner similar to traditional antibodies, involves the construction of a phage library and the selection on the basis of affinity.[106-107] These limitations not only hinder the cost-effective production of small-sized probe elements but constitute bottlenecks to sensitive detection of cytokines in low concentration.

Herein, we report, for the first time, a label-free nanoplasmonic immunoassay enabled by an antibody-derived peptide aptamer (ADPA) for the detection of low-concentration IL-6 in serum. ADPA was derived by joining three complementarity-determining region (CDR) loops of a camelid anti-IL-6 antibody with minimalist linkers that could connect various N- and C-termini of loops in the structure without imposing structural strains (**Figure 3.1a**). Cysteine residues were introduced to the linkers and two termini for anchoring onto the gold surface. Our technique that adopts a scattering light intensity-based LSPR sensing scheme, in which ADPA served as a novel probe element, allows the sensitive detection of IL-6, a key SARS-CoV-2 biomarker, with an 8-times lower LOD than an antibody-based LSPR immunoassay. The ability of ADPA-based LSPR immunoassay to measure much lower concentrations of proteins derives from two effects: (i) the

characteristically smaller dimension of ADPA, 1.5 nm in size, and (ii) directed ADPA immobilization on a "bare" Citrate capped gold nanorod (Cit-AuNR) through Au-S bonding (**Figure 3.1b**). Integrated with a functional microfluidics system, our platform completed the whole assay, including sample loading, incubation, and washing, in 35 min with a miniature sample consumption of 3 μL (**Figure 3.1c**). We also tested the utility of our ADPA-based immunoassay in profiling IL-6 secretion levels from human lung epithelial cells, macrophages, and co-cultured cells exposed to SARS-CoV-2 spike protein. We anticipate our approach, leveraging unique small-sized ADPA in the LSPR sensing scenario, may serve as not only a sensitive tool for the detection of low-concentration biomarkers and a powerful immune monitoring platform.

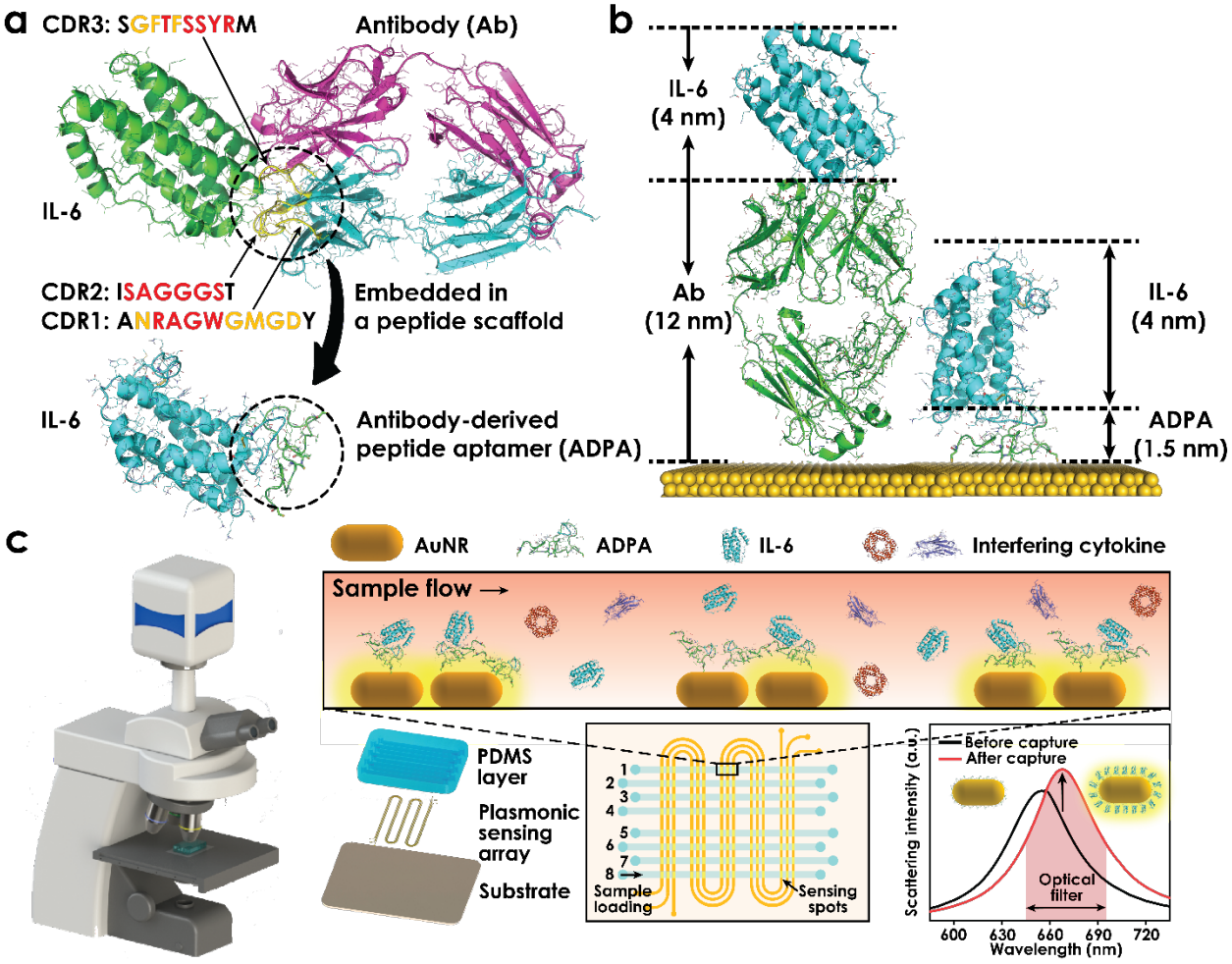

Figure 3.1 Schematic illustration of ADPA design and ADPA based nanoplasmonic immunoassay. (a) The solved antibody-antigen complex structure, in which IL-6 (olive) is recognized by three CDR loops from the heavy chain (cyan). (b) Predicted structure of IL-6 captured by antibody (left) and ADPA (right) on a bare gold surface. The dimension of antibody, ADPA, and IL-6 was calculated as 12 nm, 1.5 nm, and 4 nm. (c) The illustration of a microfluidic integrated LSPR biosensing platform. Cit-AuNRs were firstly patterned on a glass substrate, followed by the direct functionalization of ADPA. As-fabricated LSPR chip was mounted under an optical dark-field microscope. IL-6 in the sample captured by ADPA contributed to an increase in scattering light intensity, which was monitored by a high-resolution EMCCD camera in real-time.

3.2 Materials and Methods

3.2.1 Surface plasmon resonance analysis

The bare gold sensor was thoroughly cleaned in piranha solution (30mL 98% sulfuric acid: 10 mL 30% hydrogen peroxide) for 10 min, followed by 15 min-sonication. 30 μL 1 g/L ADPA scheme 1 or scheme 2 was added into 60 μL 10 mM tris(2-carboxyethyl)phosphine (TCEP) solution and incubated in dark for 1 hour. The mixture was then diluted into a 30 mg/L solution with a pH of 7.4 phosphate-buffered saline (PBS) and injected at 30 L/min into the cleaned bare gold sensor for ligand immobilization. The abundant cysteine residues in scheme 1 and scheme 2 allowed their strong adsorption on gold due to the formation of an Au-S bond. After 30 min of adsorption, 3 mM 6-mercapto-hexanol in pH 7.4 PBS was injected for 1 hour to passivate the gold surface. The surface was then washed with the PBS buffer and then challenged with different concentrations of IL-6 in a PBST buffer (pH 7.4 PBS, 0.05% Tween-20) at 30 L/min. Under each concentration, the injection volume of IL-6 solution was fixed at 250 L. The SPR data was measured at 293 K. The sensor regeneration was accomplished by 10 mM glycine-HCl (pH = 2.5) for 1 min.

3.2.2 Dynamic light scattering and zeta-potential measurements

200 μL freshly prepared samples were diluted by 600 μL deionized water and then transferred into a capillary zeta cell (Malvern). The Cell was stabilized in the zetasizer (Zetaiszer Nano ZS 90) for 3 min and then zeta potential and hydrodynamic size of samples were recorded.

3.2.3 SEM characterization of patterned AuNR

A drop of Cit-AuNR solution was blotted on a silicon wafer and the morphology was characterized by a KEOL JSM-7000F scanning electron microscope.

3.2.4 s-SNOM characterization of patterned AuNR, ADPA-AuNR, and ab-AuNR

The nano-imaging experiments mentioned in the main text were performed using a neaspec scattering-type scanning near field optical microscopy. The s-SNOM is based on a tapping-mode AFM with a tapping amplitude ~ 40 nm and tapping frequency ~ 250 kHz. Metalized AFM tip was used with the coating of PtIr5 and the tip radius ~ 10 nm. In the nano-imaging experiment, a monochromatic IR quantum cascade laser (QCL) was used to illuminate the AFM tip. The back-scattered optical signal of the tip was collected and demodulated at the 3rd harmonics of the tapping frequency to provide genuine near-field optical responses.

3.2.5 LSPR immunoassay preparation protocol

PDMS prepolymer was prepared by a mixture of 1:10 silicone elastomer base and curing agent (SYLGARD 184). The resulting mixture was then poured over the silicon mold and degassed for 30 mins. After that, it was placed in an oven at 65 °C for 4 hours. A Glass slide was firstly washed by deionized (DI) water and dried in a 65 °C incubator. Then the glass slide was soaked in the piranha solution (H_2O_2:H_2SO_4=1:3) to remove organic residues. Excessive piranha solution was washed by DI water and the glass slide was further cleaned by ultrasonics for 15 mins. The cleaned glass slide was then placed in a desiccator with 0.5 mL APTES (Thermo Scientific) for 48 hours. After the 2-day incubation, the as-prepared glass slide was heated in a 100 °C incubator to further fix the monolayer of APTES molecules. A piece of PDMS layer with microfluidic channels on the bottom was applied to the as-prepared APTES glass slide. Cit-AuNR solution was loaded into each microfluidic channel at 1 μL/mL for 8 mins, therefore the negatively charged Cit-AuNRs can be immobilized onto positively charged APTES glass through electrostatic interactions. After a 12-hour incubation period, the unbounded AuNRs were washed. A 50 μg/mL probe element solution (antibody or antibody-derived peptide aptamer) was injected at 1 μL/mL for 8 mins. After

an hour incubation, the excessive probe elements were washed, followed by 1-hour bovine serum albumin (BSA) surface passivation. The original piece of the PDMS layer was discarded and another piece of PDMS was applied perpendicularly onto the as-prepared nanoplasmonic chip.

3.2.6 LSPR immunoassay assay protocol

The constructed nanoplasmonic chip was placed on a motorized stage (ProScan III, Prior Scientific) for the positioning area of interest. Upon the application of immersion oil (Nikon Instrument Inc), the condenser lens was then gently attached to the bottom of the nanoplasmonic chip. For a dark-field microscope, all other lights were blocked but only scattering light that went through a 10× objective lens (Nikon Instrument Inc). Scattering light was then filtered by a band-pass optics (645-695 nm, Chroma) and recorded by an EMCCD camera. The collected images were analyzed by a customized Matlab code so that LSPR signal was read out in real-time.

3.2.7 Cell culture and stimulation

THP-1 was purchased from ATCC and cultured in Roswell Park Memorial Institute (RPMI) 1640 medium (CORNING) with 10% fetal bovine serum (ThermoFisher) and 1% penicillin-streptomycin in a 5% CO_2 humidified incubator at 37 °C. Macrophages were differentiated from THP-1 by incubation in the aforementioned cell culture medium with 100 ng/mL phorbol 12-myristate-13-acetate (PMA) for 48 hours. Lung epithelial cells (ATCC) were cultured Keratinocyte serum free medium (Gibco) with 0.05 mg/mL bovine pituitary extract (Gibco), 5 ng/mL epidermal growth factor (Gibco) and 10 ng/mL cholera toxin (Invitrogen). Briefly, untreated epithelial cells (106 cells per mL) and macrophages (106 cells per mL) were seeded in a 12-well plate overnight. Before surface protein stimulation, the remaining medium was discarded, and then SARS-CoV-2 surface proteins were prepared in corresponding medium at varying

concentrations (1 μg/mL to 20 μg/mL). Cell culture supernatants were collected after 48 hours for further study.

3.2.8 Characterization of LSPR chip

The morphology of AuNRs on the as-patterned LSPR chip was characterized by a KEOL JSM-7000F scanning electron microscope and a neaspec scattering-type scanning near field optical microscopy. 1 mL freshly prepared ADPA functionalized AuNR solution and antibody functionalized AuNR solution was added onto a silicon wafer and dried at room temperature.

3.2.9 Finite element analysis simulation

The electromagnetic simulation of AuNR, ADPA functionalized AuNR and antibody functionalized AuNR was performed by COMSOL. The dimensions of AuNR, antibody, and ADPA were obtained from SEM images and dynamic light scattering. A 40 × 80 nm AuNR was first constructed followed by a shell of recognition layer (12 nm thickness for antibody; 1.5 nm for ADPA). A far-field domain with a diameter equivalent to an incident light wavelength was then defined and, on top of that, a perfectly matched layer was set as boundary condition of scattering. A polarized electric field was defined parallel to the longitudinal direction of the AuNR. The frequency-dependent dielectric constant was calculated from the Lorentz-Drude model, while relative permittivity of antibody and peptide aptamer was set as 2.55.

3.3 Results and Discussion

3.3.1 Rational design of antibody-derived peptide aptamer

The anti-IL-6 antibody (PDB ID: 4o9h) was used to design the peptide aptamers.[108] As shown in the solved antigen-antibody complex structure, the recognition of IL-6 was mainly due to binding with three complementarity-determining regions (CDRs) of the heavy chain. We rationally designed peptide aptamers by joining three CDR loops with linkers and tested different schemes of loop sequence orders. Cystine residues were introduced to linkers and termini for targeted immobilization through Au-S bonding (**Figure 3.2a**). As shown in **Figure 3.2b**, two schemes of ADPA (denoted S1 and S2) were obtained for experimental validation. Noteworthy, compared to widely reported single-domain antibody or nanobody that is ~15 kDa, our ADPA has an even smaller dimension (~3 kDa). The net charge of both peptide aptamers was +1e under our typical experiment conditions (pH = 7.4). The negatively charged citrate gold nanorod was selected in this work to promote electrostatic interaction with ADPA.[109-111] More importantly, as compared to commonly-used CTAB-AuNR, Cit-AuNR offers a "bare surface" that can be readily displaced by other ligands.[112-113] Such virtue is attractive for the subsequent nanoparticle surface functionalization.

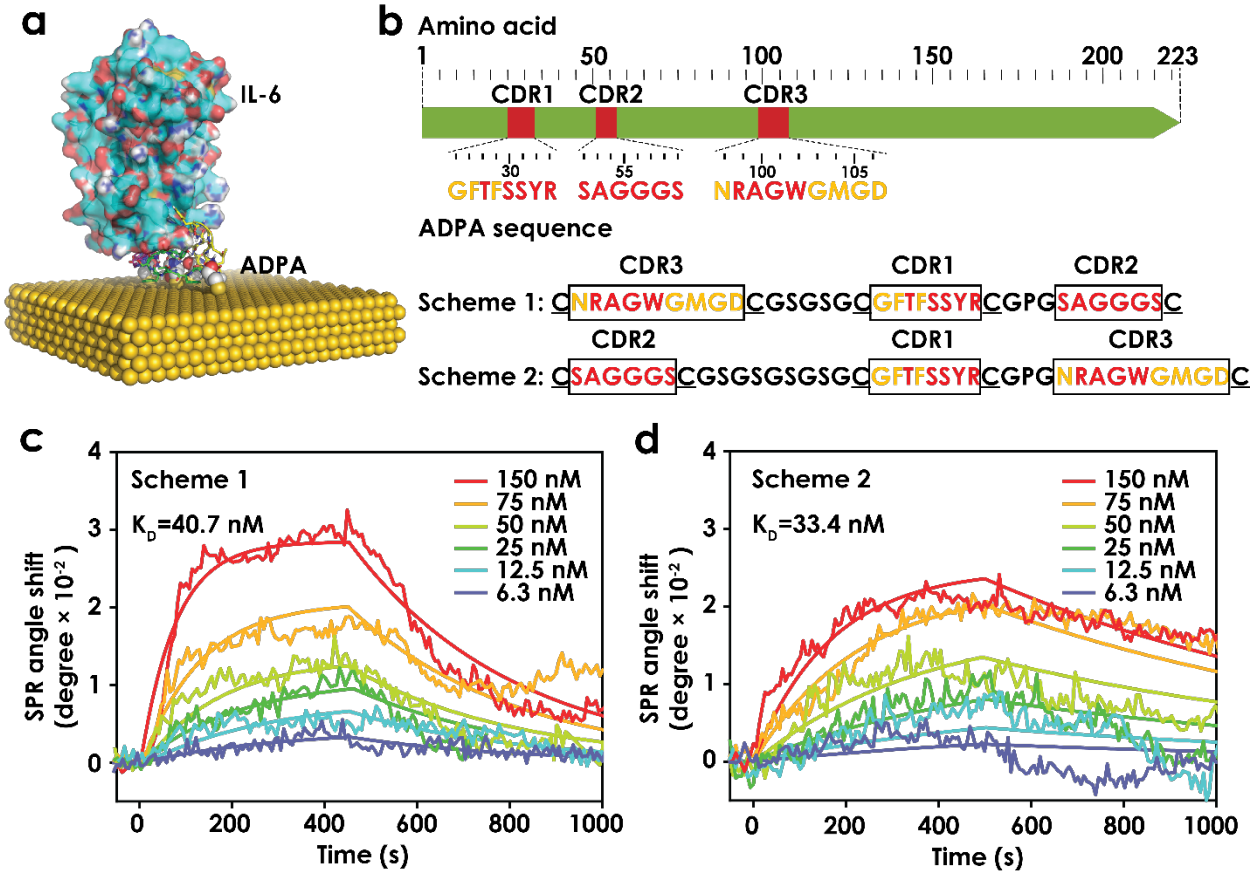

Figure 3.2 Rational design of ADPA. (a) Predicted 3D structure of ADPA-IL-6 complex on a gold surface. (b) Three CDR loops were calculated from a full sequence of anti-IL-6 antibody (PDB ID: 4o9h). Two ADPA schemes were designed by joining three CDR loops with linkers and cystine residues were introduced for directed immobilization on gold surface. (c-d) SPR kinetics of interaction between two ADPA schemes and human IL-6. Scheme1 and scheme2 showed an equilibrium dissociation constant of 40.7 nM and 33.4 nM, respectively.

3.3.2 Characterization of ADPA

The affinities of ADPA for human IL-6 were characterized by SPR analysis. To perform SPR measurements, we flowed a series of human IL-6 samples with different concentrations into the SPR sensing chamber and the kinetic curves for the interaction between two ADPA schemes and IL-6 were recorded. By fitting the curves into the one-to-one binding model, the kinetic parameters of scheme1 were determined as an association constant (K_a) of 6.93×10^4 $M^{-1} \cdot s^{-1}$, a dissociation constant (K_d) of $2.82 \times 10^{-3} \cdot s^{-1}$, and an equilibrium dissociation constant (K_D) of 40.7 nM (**Figure 3.2c** and **Table 3.1**), while scheme2 showed an association constant of 3.29×10^4 $M^{-1} \cdot s^{-1}$, a dissociation constant of $1.10 \times 10^{-3} \cdot s^{-1}$ and an equilibrium dissociation constant of 33.4 nM (**Figure 3.2d** and **Table 3.1**). Therefore, the specific recognition capacities of both ADPA were confirmed.

Table 3.1 The properties and kinetic constants of ADPA

	Molecular weight (kDa)	Isoelectric point	K_a ($M^{-1} \cdot s^{-1}$)	K_d (s^{-1})	K_D (M)
S1	3.40	7.54	6.93×10^4	2.82×10^{-3}	4.07×10^{-8}
S2	3.69	7.54	3.29×10^4	1.10×10^{-3}	3.34×10^{-8}

3.3.3 Targeted immobilization of ADPA on AuNR

Conventional functionalization of biomolecular probes is achieved through the standard EDC/NHS coupling chemistry, which forms stable covalent bonds between primary amines on antibodies and carboxyl groups on AuNRs (**Figure 3.3a** top). However, antibodies exhibit multiple primary amine binding sites, therefore the resulting random orientations of antibody potentially affected the accessibility of antibody binding regions.[114-115] In this regard, we explored a cystine-targeted direct functionalization strategy for ADPA immobilization (**Figure 3.3a** bottom).

Specifically, cystine residues were inserted between neighboring CDR loops, thus the antigen-binding sites in our ADPA design, i.e., CDR loops, being free from steric hindrance. As shown in **Figure 3.2a**, ADPA was targeted immobilized on a gold surface through Au-S bonding with the desired orientation. More importantly, our cystine targeted immobilization strategy that eliminates the use of thiolated ligands typically involved in the traditional EDC/NHS coupling method. Associated with a characteristically small-sized ADPA (1.5 nm in size), a minimized thickness of the recognition layer can be formed, which is critical in the LSPR sensing scenario (**Figure 3.2b** and **f**). In LSPR sensing theory, the highly localized electric field is sensitive to subtle refractive index variations of the local environment. The strength of the aforementioned electric field exponentially decays with the distance from nanoparticle-medium interface. Such nature suggests that the LSPR sensitivity is expected to vary by the location of antigen-antibody binding events. To approximate such relation, an equation derived from Mie scattering is given by following:

$$R = m\Delta\eta e^{-\frac{d_1}{l_d}}\left(1 - e^{-\frac{d_2}{l_d}}\right) \quad (1)$$

Where R is the plasmonic response, m is the refractive-index response from the plasmonic nanoparticle, Δη is the refractive index difference induced from adsorbed layer, ld is the decay length, and d1 and d2 are the thickness of recognition layer and analyte layer, respectively.[116] Analysis of eq. 1 implies, for a given system, LSPR sensitivity rises with a thinner recognition layer and thicker analyte layer. As a result, the application of small-sized ADPA in the LSPR sensing scheme together with the cystine residue targeted immobilization strategy exploits the space in close proximity of the AuNR surface, where the electric field is exponentially stronger.

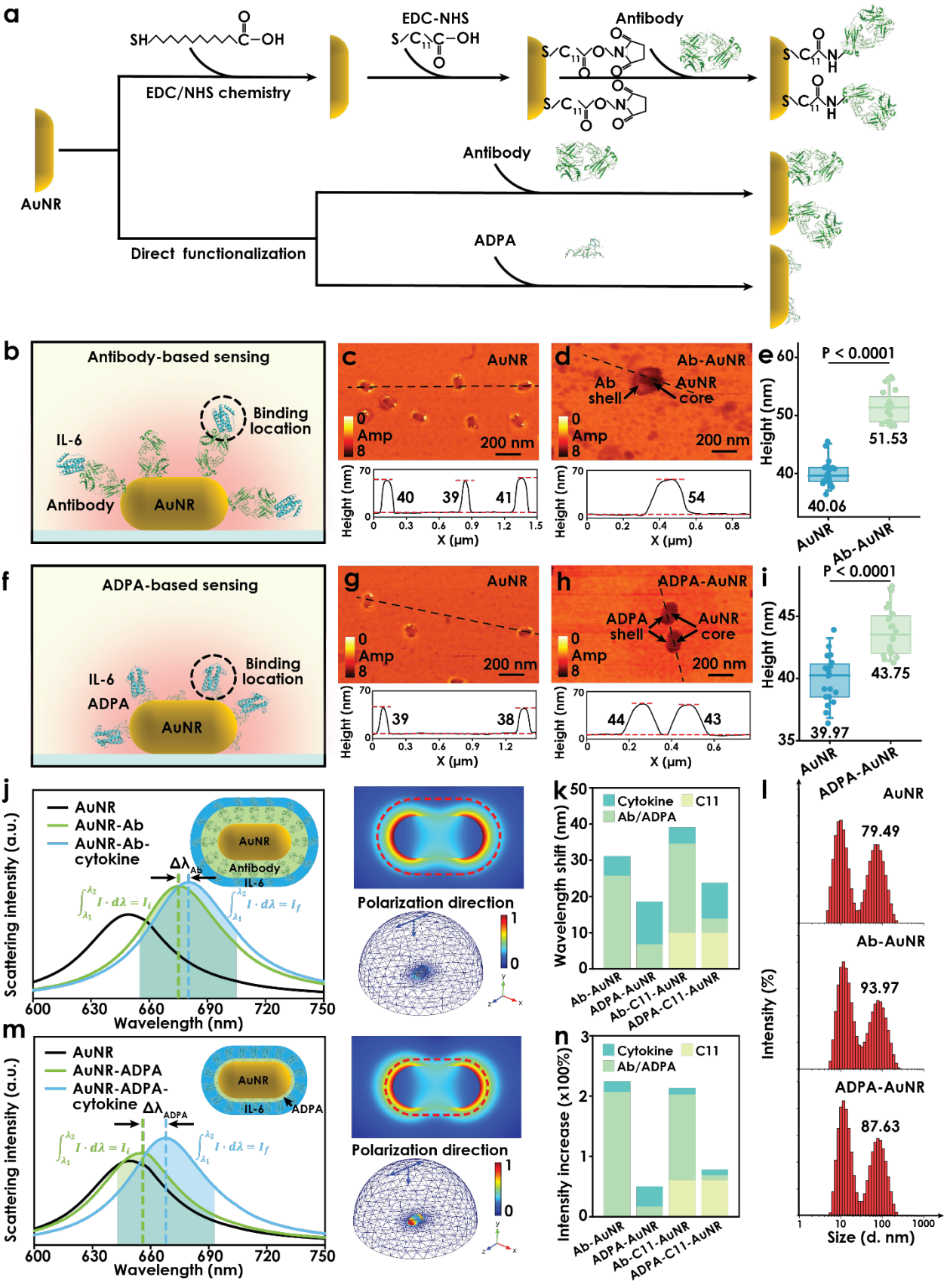
a
SH
C–OH
O
EDC/NHS chemistry
EDC-NHS
S/C11C–OH
O
Antibody
AuNR
Antibody
Direct functionalization
ADPA
b
Antibody-based sensing
Binding location
IL-6
Antibody
AuNR
c
AuNR
0
Amp
8
200 nm
Height (nm)
70
0
40
39
41
0
0.3
0.6
0.9
1.2
1.5
X (μm)
d
Ab-AuNR
Ab shell
AuNR core
0
Amp
8
200 nm
Height (nm)
70
0
54
0
0.2
0.4
0.6
0.8
X (μm)
e
P < 0.0001
Height (nm)
60
50
40
51.53
40.06
AuNR
Ab-AuNR
f
ADPA-based sensing
Binding location
IL-6
ADPA
AuNR
g
AuNR
0
Amp
8
200 nm
Height (nm)
70
0
39
38
0
0.3
0.6
0.9
1.2
X (μm)
h
ADPA-AuNR
ADPA shell
AuNR core
0
Amp
8
200 nm
Height (nm)
70
0
44
43
0
0.2
0.4
0.6
X (μm)
i
P < 0.0001
Height (nm)
45
40
35
43.75
39.97
AuNR
ADPA-AuNR
j
AuNR
AuNR-Ab
AuNR-Ab-cytokine
AuNR
Antibody
IL-6
Δλ Ab
Scattering intensity (a.u.)
600
630
660
690
720
750
Wavelength (nm)
Polarization direction
1
0
k
Cytokine
C11
Ab/ADPA
Wavelength shift (nm)
50
40
30
20
10
0
Ab-AuNR
ADPA-AuNR
Ab-C11-AuNR
ADPA-C11-AuNR
l
AuNR
79.49
Ab-AuNR
93.97
ADPA-AuNR
87.63
Intensity (%)
1
10
100
1000
Size (d. nm)
m
AuNR
AuNR-ADPA
AuNR-ADPA-cytokine
AuNR
IL-6
ADPA
Δλ ADPA
Scattering intensity (a.u.)
600
630
660
690
720
750
Wavelength (nm)
Polarization direction
1
0
n
Cytokine
C11
Ab/ADPA
Intensity increase (x100%)
3
2
1
0
Ab-AuNR
ADPA-AuNR
Ab-C11-AuNR
ADPA-C11-AuNR

Figure 3.3 Illustration of two immobilization strategies and characterization of AuNR, ab-AuNR, and ADPA-AuNR. (a) Schematic representation of antibody/ADPA surface functionalization strategies, i.e., covalent bonding through standard EDC/NHS coupling chemistry and cystine targeted immobilization. (b) Illustration of a typical antibody-antigen binding scenario in LSPR sensing scheme, where the binding locations are far from AuNR-dielectric interface. (c-d) Representative s-SNOM images of isolated AuNRs patterned on the substrate and antibody directly functionalized on AuNR. Bottom: cross-section profile of particles taken along the dashed line. (e) Statistics of particle heights. Individual dots correspond to the individual particles (n=20). Box plots depict the 25th percentile, median, and 75th percentile, whiskers show the 95% confidence intervals. (f) Illustration of a typical APDA-antigen binding scenario in LSPR sensing scheme, where the binding locations are close to AuNR-dielectric interface. (g-h) Representative s-SNOM images of isolated AuNRs patterned on the substrate and ADPA directly functionalized on AuNR. Bottom: cross-section profile of particles taken along the dashed line. (i) Statistics of particle heights. Individual dots correspond to the individual particles (n=20). Box plots depict the 25th percentile, median, and 75th percentile, whiskers show the 95% confidence intervals. (j) Predicted scattering spectra of AuNR, AuNR-Ab, and AuNR-Ab-cytokine. A 2D illustration of the model is given in the top-right corner of the plot. 2D (top-right) and 3D (bottom-right) electromagnetic field distribution. (k) Comparison of scattering resonance wavelength shift induced in each step. (l) Dynamic light scattering (DLS) analysis to confirm the assembly of antibody and ADPA on AuNR. (m) Predicted scattering spectra of AuNR, AuNR-ADPA, and AuNR-ADPA-cytokine. A 2D illustration of the model is given in the top-right corner of the plot. 2D (top-right) and 3D (bottom-right) electromagnetic field distribution. (k) Comparison of relative scattering intensity increase induced in each step.

SEM was firstly employed to validate the monodispersity of as-patterned Cit-AuNRs (**Figure 3.4a**) and the statistics of dimension were presented in **Figure 3.4b**. Cit-AuNRs were then directly functionalized by two schemes of ADPA and anti-IL-6 antibody. The three conjugates were characterized in terms of size and surface properties using DLS, zeta potential (ξ), and s-SNOM.[15, 115] As shown in **Figure 3.3i** and **Table 3.2**, our DLS measurements show AuNR has an average size of 79.49 nm in length. The immobilization of ADPA results in an 8.14 and 6.80 nm larger hydrodynamic size for scheme 1 and scheme 2, respectively, while antibody leads to a 14.48 nm increase. The surface charges were evaluated by zeta potential analysis, which shows a ξ value of -10.64, +19.50, and +11.70 mV at pH 7.4 for anti-IL-6 antibody, scheme 1 and scheme 2, respectively. After surface functionalization, the net negative charge was maintained for all three conjugates (**Table 3.2** and **Figure 3.4c-d**). Notably, both ADPAs was positively charged at pH 7.4, therefore their targeted immobilization was firstly driven by long-range electrostatic attractions, followed by the formation of Au-S bonding.[109] In order to examine the thickness of the recognition layer, we performed s-SNOM imaging at 1660 cm^{-1}, corresponding to the characteristic amide I band of peptide infrared spectrum.[78] The s-SNOM amplitude images (**Figure 3.3c-d**, **g-h**) were related to the electromagnetic field over the sample surface at a nanoscale spatial resolution and allowed the direct visualization of the recognition layer. Isolated AuNRs exhibited excellent monodispersity in the s-SNOM images (**Figure 3.3c** and **g**), in accord with our SEM results. A bright ring with enhanced amplitude signal at the apexes were observed around bare AuNRs due to the antenna effect. The existence of the recognition layer was supported in s-SNOM images: a significant thicker antibody layer was imaged in the ab-AuNR (**Figure 3.3d**), comparison with that in the ADPA-AuNR (**Figure 3.3h**). It is also noteworthy that the dimension of particles imaged by s-SNOM appeared slightly larger than our SEM results. This was explained by the tip

apex used in our experiment had a radius of *ca.* 35 nm.[78] In this regard, to precisely characterize as-formed probe-element layer thickness, we plotted the height profiles of each individual particles, instead of length/width. As illustrated in **Figure 3.3e**, an average height of 40.06 nm was obtained from AuNRs, while antibody functionalization resulted in a 51.53 nm height. In contrast, the formation of the ADPA layer only increased the height of AuNR from 39.97 nm to 43.75 nm (**Figure 3.3i**). Therefore, our s-SNOM results demonstrated the recognition layer thickness difference resulted from varying dimensions of the probe element.

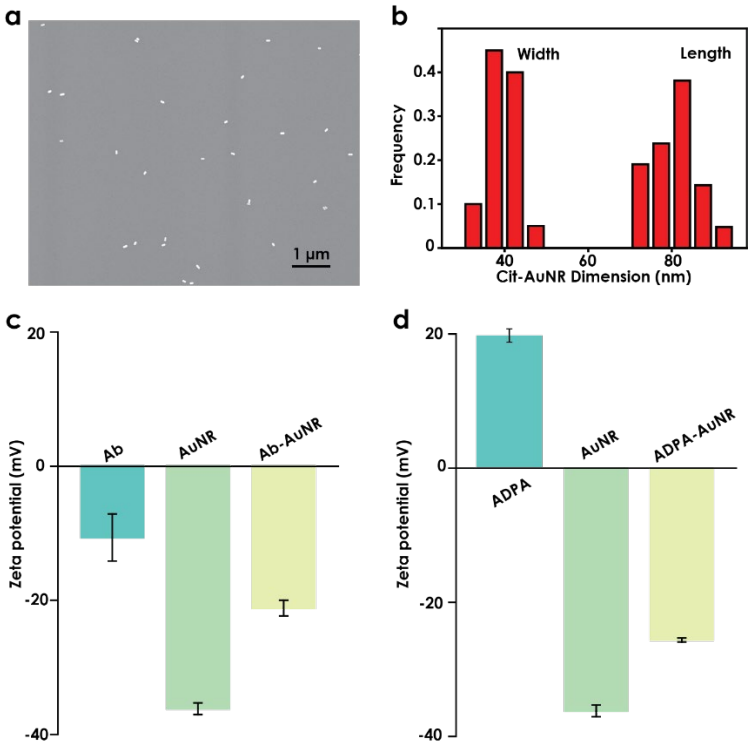

Figure 3.4 Characterization of Cit-AuNR, ab-AuNR, and ADPA-AuNR. (a) A representative SEM image of as-patterned Cit-AuNR on the glass slide. AuNRs were isolated so that plasmonic coupling between neighboring AuNRs was suppressed. (b) Statistics of AuNR width and length measured from (a). (c) Zeta potential of ab, AuNR, and ab-AuNR. (d) Zeta potential of ADPA, AuNR, and ADPA-AuNR.

Table 3.2 The hydrodynamic size and zeta potential of antibody, peptide aptamer, AuNR, and corresponding conjugates.

	Antibody	S1	S2	AuNR	Antibody-AuNR	S1-AuNR	S2-AuNR
Size (nm)	23.62 ± 0.34	2.43 ± 0.83	2.83 ± 0.97	79.49 ± 0.80	93.97 ± 1.53	86.29 ± 2.56	87.63 ± 1.56
Zeta Potential (mV)	-10.64 ± 3.50	19.50 ± 0.98	11.70 ± 2.13	-36.17 ± 0.87	-21.17 ± 1.17	-25.60 ± 0.30	-31.17 ± 1.04

Finally, we performed a finite element analysis (FEA) simulation to investigate the plasmonic signals that arose from different sized probe elements. Based on our SEM and s-SNOM results, a 40 nm × 80 nm AuNR model was firstly constructed, and its scattering resonance peak was computed at 649 nm (**Figure 3.3j** and **m**). The attachment of a probe element layer induced a shift in resonance wavelength ($\Delta\lambda$) and an overall increase in scattering intensity (ΔI) due to the dielectric property change in the local environment. Conventional spectrum-based LSPR biosensing platform measures the scattering light wavelength shifting and correlates that to analyte concentrations. Suffering from limited resolution of the spectrometer, spectrum-based detection typically yielded a signal variance of 0.3 nm, while our recently reported intensity-based LSPR biosensing platform equipped with a high-resolution EMCCD camera, exhibited a 10 times lower limit of detection.[6] Recent studies also found that for a gold nanorod with a scattering resonance wavelength below 700 nm, d-electrons (interband damping) induced an overall intensity increase which dominated plasmonic response, rendering intensity-based LSPR detection more advantageous to improve sensing performance.[117] Therefore we evaluated the influence of recognition layer thickness on both plasmonic signals, i.e., resonance wavelength shifting ($\Delta\lambda$) for spectrum-based detection and relative scattering intensity change ($\Delta I/I_i$) for intensity-based detection. **Figure 3.3j** revealed a major wavelength shift (25.8 nm) resulted from the formation of a uniform and closely packed antibody layer, while the following attachment of an analyte layer

only induced a 5.3 nm resonance peak shift and a 16.39% relative intensity increase (**Figure 3.3j** and **m**). On the contrary, analyte layer formation on the ADPA layer, considering its significantly smaller dimension, contributed to a red-shifting of 11.6 nm and a relative intensity change of 32.14% (**Figure 3.3j**, and **m**). We constructed another model to predict plasmonic signals from the immunoassay where probe elements were covalently functionalized through conventional EDC/NHS coupling chemistry. A 2 nm thiolated alkane layer was defined over AuNR.[118] In our previous study, a self-assembled monolayer of thiolated alkane HS-$(CH_2)_{11}$-COOH was functionalized on the gold surface so that EDC/NHS provided practical conjugation to carboxylic acids (-COOH).[6, 15] In this case, analytes attached to antibody led to only 4.4 nm peak shift and 9.66% relative intensity increase (**Figure 3.5**a), while a 9.7 nm red-shifting and 8.71% intensity increase was simulated for ADPA sensor (**Figure 3.5b**). As depicted in **Figure 3.3k** and **2n**, our simulation results indicate: (i) small-sized ADPA based sensor induces stronger plasmonic signals than conventional antibody, except for intensity increase from C11 functionalized LSPR sensor; (ii) direct functionalization yields higher signals in all models; (iii) intensity-based sensing scheme contributes to 3 times and 1 times improvement for direct ADPA and antibody functionalization method, respectively, while only a slight enhancement (less than 0.3) for resonance wavelength-based sensing. Therefore, our results suggest taking advantage of the intensity-based sensing scheme, directly functionalized ADPA based plasmonic immunoassay maximizes LSPR sensing performance.

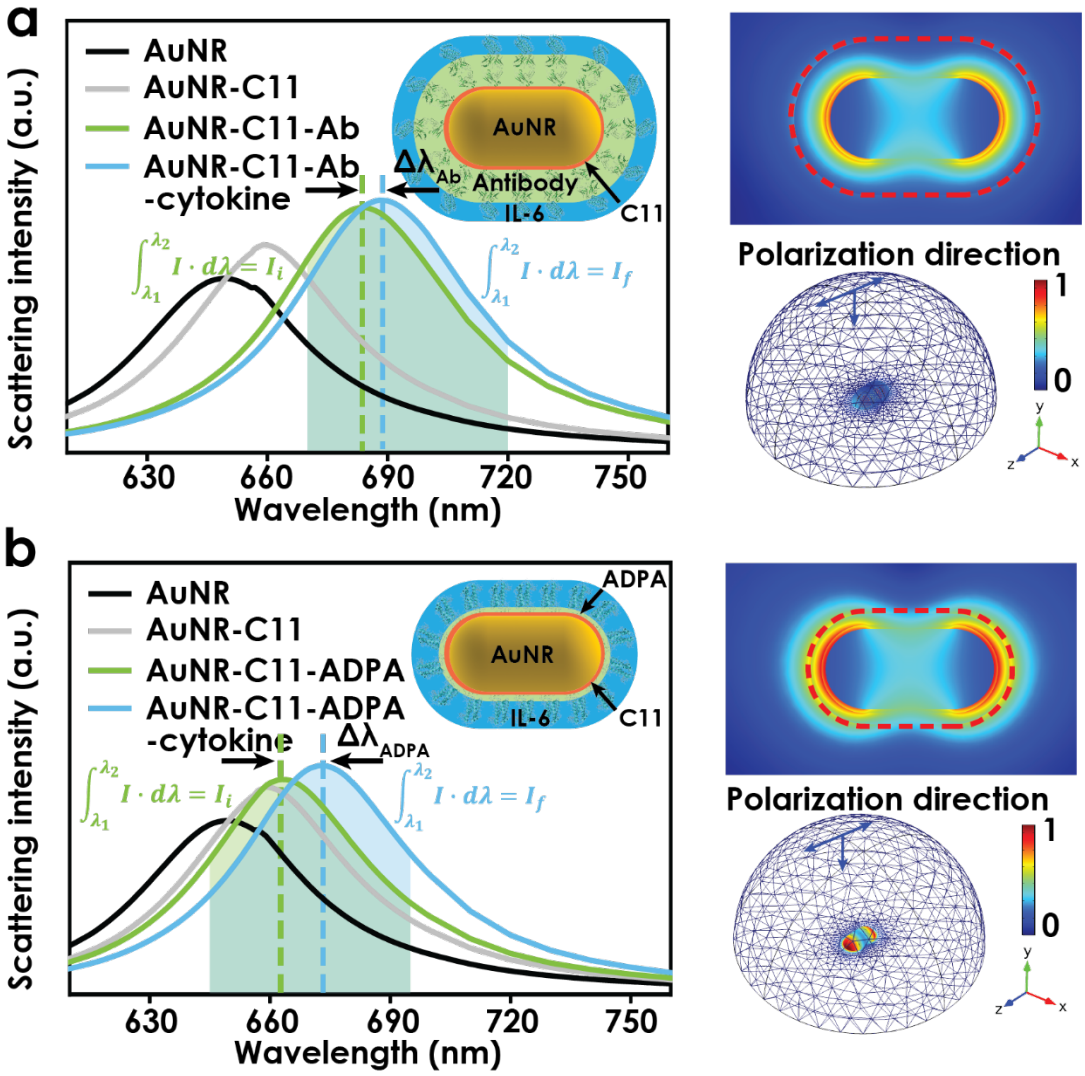

Figure 3.5 The FEA simulation of scattering spectra. (a) Predicted scattering spectra of AuNR, AuNR-C11, AuNR-ab, and AuNR-ab-cytokine. A 2D illustration of the model is given in the top-right corner of the plot. 2D (top-right) and 3D (bottom-right) electromagnetic field distribution. (b) Predicted scattering spectra of AuNR, AuNR-C11, AuNR-ADPA, and AuNR-ADPA -cytokine. A 2D illustration of the model is given on the top-right corner of the plot. 2D (top-right) and 3D (bottom-right) electromagnetic field distribution.

3.3.4 ADPA-based LSPR assay protocol

To evaluate the utility of ADPA in intensity-based LSPR sensing, we investigated the ability of both ADPA schemes to interrogate human IL-6 in serum and compared that with commercially available antibody (**Figure 3.1c**). Compared with the current gold standard method ELISA that requires multiple steps of labeling and washing along with a large volume of sample; our LSPR sensing platform integrated with a microfluidic system eliminates the need for bulky optics and is more advantageous for real-time signal readout and point-of-care analysis with a much smaller sample consumption (~3 μL).[6, 15, 54, 97] However, the LOD of our previously reported LSPR platform ranges from 11.3 pg/mL to 45.6 pg/mL, depending on the selection of nanotransducer, e.g., composition, aspect ratio, capping agent and the affinity of commercialized antibodies, while the level of one of the key biomarkers, IL-6, in healthy individuals is typically below 10 pg/mL. Therefore, ADPA-based LSPR immunoassay may find it useful in discerning subtle IL-6 concentration differences. **Figure 3.6a** depicts the workflow of our LSPR immunoassay, which involves AuNR immobilization, direct ADPA functionalization, and on-chip sensing. Notably, with the prefabrication of massive AuNR patterned chips that can be stored for weeks, our platform requires only one hour for ADPA functionalization and 35 min for on-chip protein quantification. Analytes captured by ADPA induced a resonance wavelength shift and an overall intensity increase. By utilizing a high-resolution EMCCD camera, dark-field images were recorded in a 10 second temporal resolution, and scattering light intensities on the area of interest were analyzed by our customized Matlab algorithm in a real-time manner. The LSPR signal ($\Delta I/I_i$) was thus given by the scattering light intensity change (ΔI) from the area of interest divided by the initial scattering light intensity of the same area (I_i).

To perform the assay, we fabricated LSPR chips functionalized by three different probe elements, i.e., antibody, ADPA-S1, and ADPA-S2. Prior to each measurement, PBS buffer was flowed through channels to stabilize the assay. Then we flowed a series of standard IL-6 spiked in human serum through our sample loading channels for 30 mins (**Figure 3.6a** bottom) and LSPR signals were read out in real-time. Nonspecifically bound serum constituents were washed from sensor surfaces. This resulted a final LSPR signal of 2.53% (ADPA-S1), 2.10% (ADPA-S2) and 0.67% (antibody) for 100 pg/mL IL-6 (**Figure 3.6b**). **Figure 3.3d** illustrated the mapping of relative intensity changes ($\Delta I/I_i$) after the assay and three calibration curves were established for future estimates (**Figure 3.6c**). Antibody functionalized LSPR immunoassay exhibited a narrow dynamic range, potentially explained by fewer antibodies, given to their large size, immobilized on AuNR surface, and the lower accessibility to analytes due to their random orientations (**Figure 3.6c** bottom). Analysis of eq.1, when spiked IL-6 concentration was below 10 pg/mL, the undetectable plasmonic response was explained by the greater recognition layer thickness (d_1/l_d) as compared to a smaller analyte layer thickness (d_2/l_d). In contrast, a wider dynamic range was observed from both schemes of ADPA (**Figure 3.6c**). The enhanced sensing performance on the lower level of IL-6 can be ascribed to a thinner recognition layer, owing to the smaller dimension of ADPAs, therefore a stronger plasmonic signal was induced from a subtle localized refractive index change. Moreover, cysteine-targeted immobilization strategy enabled ADPA to show the desired orientation and its characteristically smaller size offered more binding sites. Taken together, ADPA-based LSPR immunoassay exhibited a wider dynamic range. The LOD that was defined by three times standard deviations of a blank sample over the slope of calibration curve for antibody functionalized LSPR sensor was determined as 37.37 pg/mL. By minimizing recognition layer thickness, our ADPA-based LSPR sensor exhibited a lower LOD of 4.56 pg/mL for ADPA-

S1 and 6.73 pg/mL for ADPA-S2. Compared to antibody-based LSPR sensing, ADPA-based LSPR immunoassay showed an 8-times lower LOD, being well-suited for the early identification of those patients who are likely to progress to critically ill.[91] Furthermore, utilizing our ADPA-based LSPR immunoassay in a blind test, we measured the IL-6 levels in 10 unknown samples. The levels measured from our platform are in good agreement with the values measured from the commercialized ELISA kit (**Figure 3.6e**).

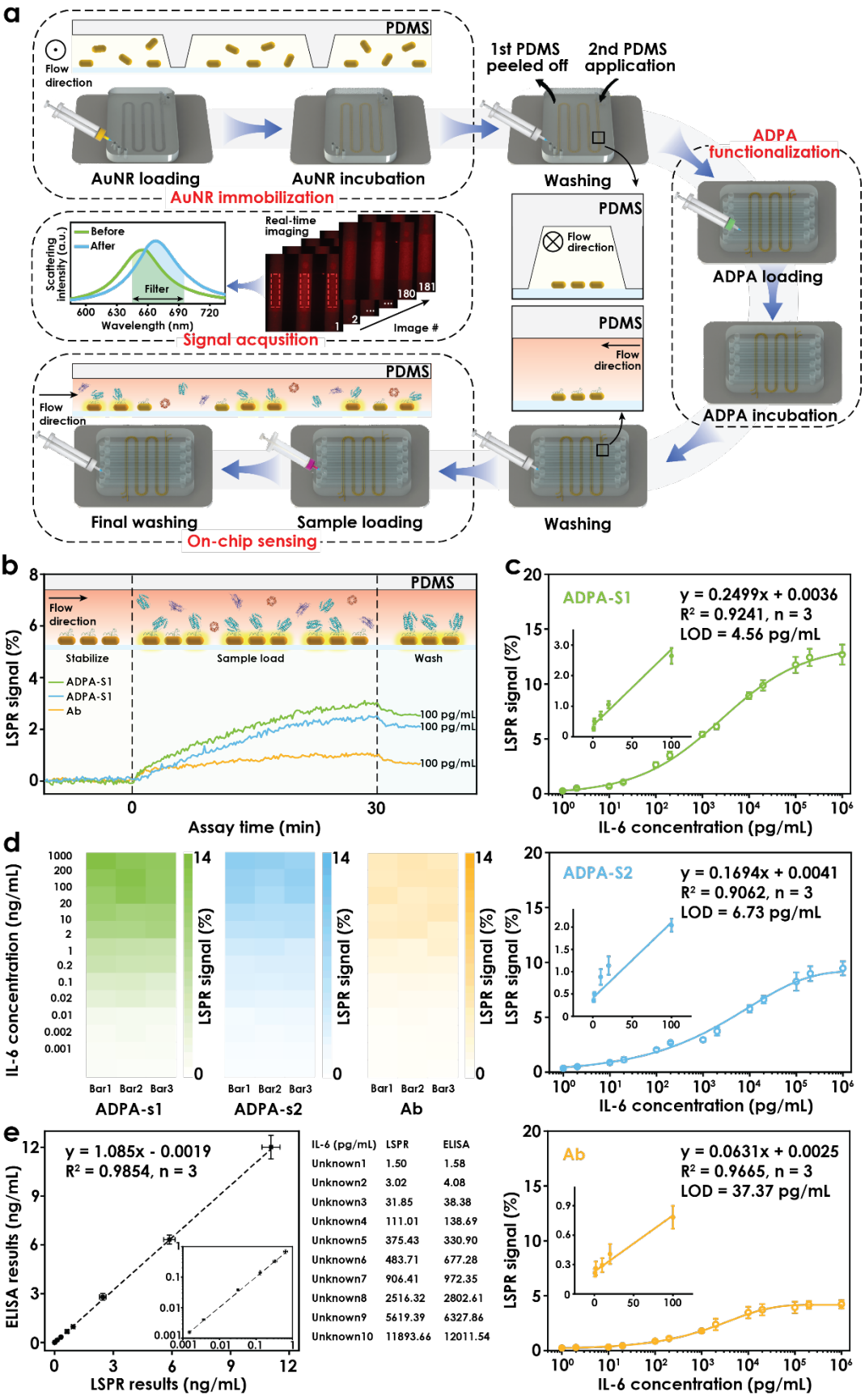
a
PDMS
Flow direction
AuNR loading
AuNR incubation
AuNR immobilization
1st PDMS peeled off
2nd PDMS application
Washing
ADPA functionalization
ADPA loading
ADPA incubation
Real-time imaging
Before
After
Scattering intensity (a.u.)
Filter
Wavelength (nm)
Image #
Signal acquisition
Final washing
Sample loading
On-chip sensing
b
LSPR signal (%)
Stabilize
Sample load
Wash
ADPA-S1
ADPA-S1
Ab
100 pg/mL
100 pg/mL
100 pg/mL
Assay time (min)
c
ADPA-S1
y = 0.2499x + 0.0036
R² = 0.9241, n = 3
LOD = 4.56 pg/mL
IL-6 concentration (pg/mL)
d
IL-6 concentration (ng/mL)
LSPR signal (%)
Bar1 Bar2 Bar3
ADPA-s1
ADPA-s2
Ab
ADPA-S2
y = 0.1694x + 0.0041
R² = 0.9062, n = 3
LOD = 6.73 pg/mL
e
y = 1.085x - 0.0019
R² = 0.9854, n = 3
ELISA results (ng/mL)
LSPR results (ng/mL)
IL-6 (pg/mL) LSPR ELISA
Unknown1 1.50 1.58
Unknown2 3.02 4.08
Unknown3 31.85 38.38
Unknown4 111.01 138.69
Unknown5 375.43 330.90
Unknown6 483.71 677.28
Unknown7 906.41 972.35
Unknown8 2516.32 2802.61
Unknown9 5619.39 6327.86
Unknown10 11893.66 12011.54
Ab
y = 0.0631x + 0.0025
R² = 0.9665, n = 3
LOD = 37.37 pg/mL

Figure 3.6 Illustration and results of LSPR immunoassay. (a) Workflow of intensity-based LSPR biosensing platform. The workflow includes three steps: (1) AuNRs immobilization on a glass substrate through electrostatic interactions; (2) ADPA functionalization through a cysteine-targeted immobilization method; (3) On-chip LSPR sensing by recording dark-field images every 10 seconds. (b) Real-time monitoring of scattering light intensity variations from LSPR chip. Top: cross-section view of the channel during stabilizing, sample load, and wash process. (c) Calibration curves of ADPA-S1 (top), ADPA-S2 (middle), and Ab (bottom) based LSPR immunoassay. Insets show the corresponding linear range regions of the calibration curves. (d) Heatmaps of LSPR signal measured from ADPA-S1 (left), ADPA-S2 (middle), and Ab (right) based LSPR immunoassay. (e) Correlation analysis between the developed ADPA-based LSPR immunoassay and commercialized ELISA kit in measuring IL-6 from 10 unknown samples.

3.3.5 IL-6 secretion profiling from SARS-CoV-2 surface protein stimulated epithelial cells and macrophages

The ongoing spread of SARS-CoV-2 along with its new variant that emerged at the end of 2020 has posed continuous challenges to global public health. By Jun 2021, more than 178 million people have been infected globally. Therefore, understanding how the immune system responds to SARS-CoV-2 infection is critical. As illustrated in **Figure 3.7a**, the first step in viral infection was that the surface (S) proteins on the virus bound to host cells mainly through angiotensin-converting enzyme 2 (ACE2).[119] Then activated series of intercellular pathway, pro-inflammatory cytokines, e.g. IL-6 were upregulated by host cells, which attracted more macrophages to the infection site. Further inflammation was promoted by macrophages thereby establishing a positive feedback loop. In this regard, the IL-6 secreted by epithelial cells and macrophages in response to SARS-CoV-2 surface protein stimulation was investigated by our ADPA-based LSPR

immunoassay (**Figure 3.7b**). **Figure 3.7c** showed IL-6 secretion by epithelial cells and macrophage was in a dose-dependent manner after S protein stimulation. When epithelial cells were cocultured with macrophages, a significantly higher level of IL-6 secretion was measured after S protein stimulation, this potentially resulted from the positive feedback loop between them. From **Figure 3.7d**, IL-6 secretion by epithelial cells did not significantly increase up until 48 hours, while macrophages secreted IL-6 was in the first 12 hours. All the cell samples were independently tested by a commercialized IL-6 ELISA kit and the results were in good agreement (**Figure 3.7 e-f**). **Figure 3.8** revealed an excellent linear correlation between results measured from our ADPA-based LSPR platform and commercialized ELISA kit. These results were consistent with previous SARS-CoV studies.[120-121]

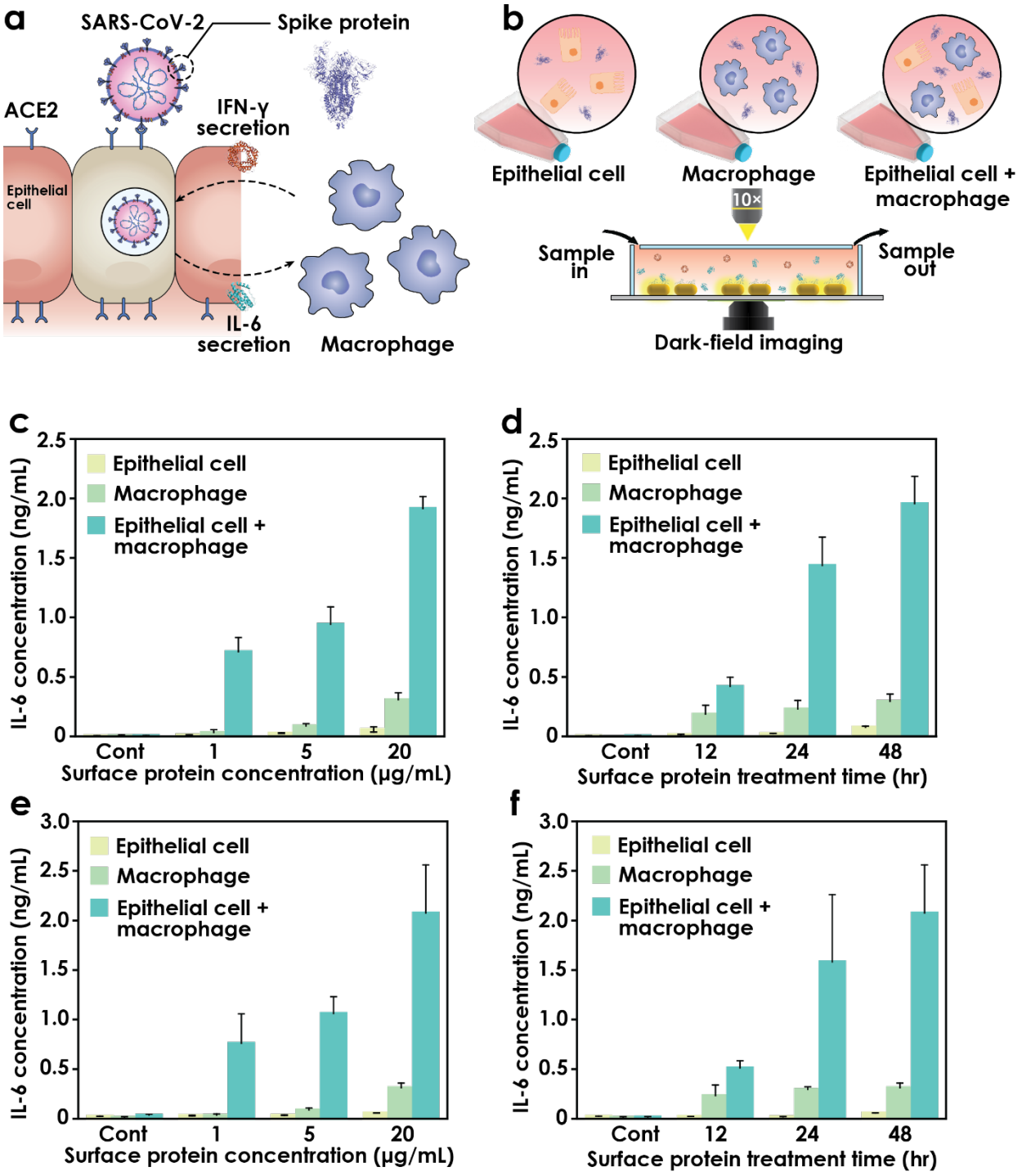

Figure 3.7 Profiling IL-6 secretion level from SARS-CoV-2 surface protein stimulated epithelial cells and macrophages. (a) SARS-CoV-2 infected host cells that expressed ACE2, triggering the production of proinflammatory cytokines, i.e., IL-6. Consequently, macrophages were attracted to

the site of the infection and released IFN-γ, thus forming a positive feedback loop. (b) Macrophages cocultured with epithelial cells were stimulated by SARS-CoV-2 surface protein and the resulting cell medium was collected for LSPR sensing. IL-6 secretion levels measured by ADPA-based LSPR immunoassay under (c) different concentrations of surface protein and (d) incubation times were investigated. IL-6 secretion levels measured by commercialized ELISA kit under (e) different concentrations of surface protein and (f) incubation times were investigated.

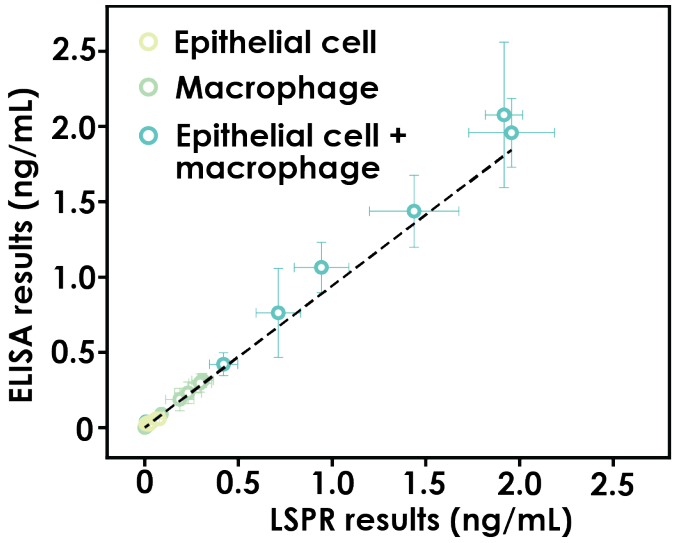

Figure 3.8 Correlation between data measured from ADPA-based LSPR immunoassay and commercialized ELISA kit. IL-6 secretion levels measured by commercialized ELISA kit.

3.4 Conclusion

In summary, we have demonstrated the rational design of two anti-IL-6 peptide aptamer derived from anti-IL-6 antibody 4o9h and explored the utility of ADPA based LSPR immunoassay for the label-free detection of IL-6 spiked in human serum and secreted from epithelial cells and macrophages in a rapid and sensitive manner. The enhanced sensing performance of ADPA-based LSPR immunoassay is attributed to: (i) binding locations in closer proximity of nanoparticle-medium interface due to the small-sized ADPA and (ii) cysteine-targeted direct immobilization strategy. To the best of our knowledge, this is the first study to demonstrate the design of ADPA and its practical application in the intensity-based LSPR immunoassay for low-concentration cytokine detection. Our technique allowed the inexpensive and rapid design of a small dimension recognition element, ADPA. Its functionality was confirmed by SPR and ELISA measurements. As directly visualized by s-SNOM, a minimized peptide aptamer layer was formed through our direct functionalization strategy. Furthermore, the integration of ADPA into our intensity-based LSRP immunoassay exhibited a wide dynamic range and a remarkable LOD of 4.56 pg/mL, 8 times lower than that of our previously reported antibody-based LSPR immunoassay. Such excellent sensing performance renders our peptide aptamer-based LSPR immunoassay well-suited for routine measurements of low-concentration cytokines. Moreover, our ADPA-based LSPR immunoassay was employed to profile the responses of SARS-CoV-2 surface protein stimulated epithelial cells macrophages, rendering the cellular functional monitoring capability.

Chapter 4

Machine-Learning-Assisted Microfluidic Nanoplasmonic Digital Immunoassay for Cytokine Storm Profiling in COVID-19 Patients

4.1 Introduction

COVID-19, an infectious disease caused by SARS-CoV-2, has emerged as a mounting threat to global health since December 2019.[122] COVID-19 infection is accompanied by an aggressive inflammatory response, known as a "cytokine storm", resulted from complex interplays between lymphocytes and myeloid cells.[122-124] Excessive production of proinflammatory cytokines in COVID-19 patients can further lead to acute respiratory distress syndrome (ARDS), multiple organ failures (MOFs), and death.[92, 123-124] Hence, early detection and close monitoring of cytokine storms is critical for rapid identification of high-risk COVID-19 patients and the development of prompt guidelines for anti-inflammatory therapies to improve survival rates. Due to the dynamic and time-sensitive clinical features of COVID-19, characterization of cytokine storms requires fast analysis of cytokines across a wide dynamic range in a small amount of patient serum with high sensitivity, selectivity, throughput, and multiplex capacity. Current gold standard clinical tools to

test blood circulating cytokines are based primarily on ELISA. The laborious and lengthy procedures, large sample consumption, and required centralized facility greatly impede its practical usage for monitoring cytokine storms in COVID-19 patients. As such, there is an urgent need for effective cytokine detection strategies that satisfy the stringent requirements to provide rapid and informative insights for COVID-19 diagnosis, monitoring, and treatment.

Over the past two decades, the microfluidic immunoassay has become an emerging technology for rapid analysis of biomolecules in complex biological samples.[57, 125-126] Microfluidics offer significant advantages in controllable fluid handling, low reagent consumption, and confined microenvironment analysis.[57, 125-127] The integration of immunoassays to the microfluidic scale shows greatly improved analytical performance at point-of-care, such as reduced assay time, small sample volume, high throughput and multiplexity, and semi automation.[57, 125-127] Recent advancements in a variety of microfluidic immunoassays have demonstrated promising features for cytokine detection, including a sample-to-answer time shortened to ~30 min, a sample volume reduced to a few μL, a throughput improved to hundreds of parallel tests, a multiplex capacity up to dozens of targets, and so on.[6, 128-130] However, accumulating evidence suggests that the cytokine concentrations in plasma of COVID-19 patients span across a wide dynamic range (1-40,000 pg mL-1) with a few key inflammatory cytokines at sub-pg mL-1 level.[122] Current microfluidic immunoassays rely mainly on conventional signal transduction technologies based on measurement of ensemble average signals, which often require numerous captured signaling molecules to generate a detectable signal over background noise. Hence, the majority of these platforms could not afford sufficient sensitivity in a multiplex, high throughput scheme to accurately detect cytokines at ultra-low levels and across a wide concentration range.

The ever-increasing demand for ultrasensitive and accurate detection has driven the development of advanced bioanalytical methods such as the digital (or single-molecule) imaging assay, where the binding of a single biomolecule to the corresponding affinity biomolecule can be individually visualized via a single signal label.[131-135] In contrast to the conventional ensemble average measurements, digital imaging approaches enable the measurement of individual biomolecule binding events with extremely high signal-to-noise ratio, resulting in the highest class of sensitivity down to single-molecule level. [131-135] Up to this time, various digital imaging technologies have been exploited based on different labeling agents (i.e., enzymes, fluorescent dyes, upconversion nanoparticles (NPs), and plasmonic metal NPs).[131, 134-141] Among them, nanoplasmonic digital imaging has received considerable attention owing to the superior physicochemical properties of plasmonic metal NPs.[138-151] The strong Rayleigh scattering of individual plasmonic NPs allows sub-diffraction imaging with extremely high spatial resolution under dark-field microscope.[141-148] The scattering intensity and the extinction spectra of the NPs can be tuned at will via precise control over NPs' size, shape, and dielectric properties.[150-152] Since signal transduction is based on light scattering, plasmonic NPs display excellent photophysical stability, allowing continuous, intermittence-free measurement.[141-148] While a few recent studies have demonstrated the use of nanoplasmonic imaging for digital biomarker detection,[139-147] the sensing performance has been greatly limited by conventional imaging analysis and manual particle counting methods. When integrating nanoplasmonic digital imaging with microfluidic immunoassays, the inability to perform rapid and accurate digital signal processing for a large amount of image data has thereby become a major challenge for sensitive high-throughput multiplex detection of cytokines in clinical settings.

Herein, we developed a nanoplasmonic digital immunoassay by integrating a machine learning assisted nanoplasmonic imaging method with a microfluidic immunoassay platform that overcomes major constraints for cytokine profiling in real patient samples (**Figure 4.1**). The immunoassay exploits a one-step sandwich microarray format utilizing anti-cytokine capture antibody (CAb) arrays as the primary capture layer, and Ag nanocubes (AgNCs) conjugated with paired detection antibodies (DAbs) as the signal transducers for massive parallel detection of multiple cytokines in a small sample volume. The formed sandwich immunocomplex can be imaged individually under dark-field microscope due to the strong plasmonic scattering of the AgNCs. The generated highly sensitive and selective digital signals can be readily counted by a customized machine-learning-based image processing method. By establishing the correlation between digital signal count and the cytokine concentration, our immunoassay allows simultaneous detection of six cytokines across a wide dynamic range of 1-10,000 pg mL^{-1} with a limit of detection down to sub-pg mL^{-1}. The integrated microfluidic platform enables high-throughput analysis of 8 different samples per chip with a total of 288 tests using only 3 μL serum samples. Using ELISA as a benchmark method, the immunoassay was validated for practical application in serum cytokine measurement with excellent accuracy and reliability and was successfully applied for profiling cytokine storms in COVID-19 patients.

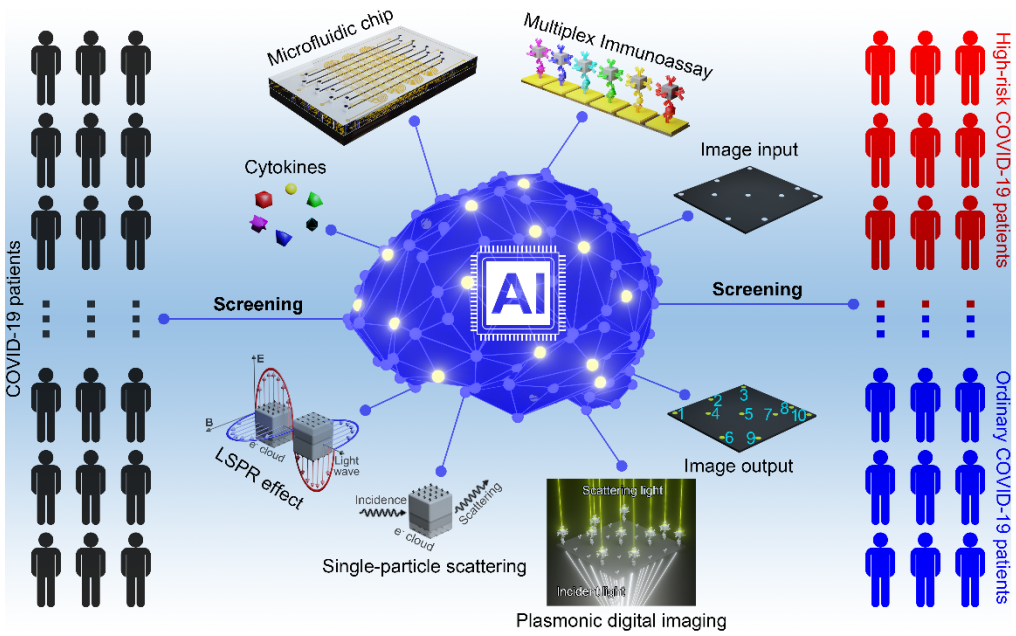

Figure 4.1 The design of machine-learning-assisted microfluidic nanoplasmonic digital immunoassay

4.2 Materials and Methods

4.2.1 Preparation of microfluidic flow mask layers made of PDMS

Two types of microfluidic flow PDMS mask layers (i.e., antibody-patterning and sample-flow PDMS mask layers) were designed in this work. The antibody-patterning PDMS mask layer contained 7 sets of parallel meandering microfluidic channels (**Figure 4.2 a-b**). The first channel was used for patterning 100 nm AgNCs as reference microarrays, and the other six channels were used for patterning multi-antibody microarrays. The width (W) and height (H) of each channel were 200 μm and 50 μm, respectively. The distance between adjacent channels was 200 μm. The sample-flow PDMS mask layer contained 8 sets of parallel straight sample-flow microfluidic channels for loading of detection samples (**Figure 4.2 c-d**). The dimensions of each channel were 3.0 cm (L) □ 200 μm (W) □ 50 μm(H), and the distance between adjacent channels was 2 mm. These two PDMS mask layers were prepared using soft lithography according to our recently published procedures with minor modifications.[6, 97] Briefly, the mold for the PDMS mask layer was first manufactured on the surface of a silicon substrate by using deep reactive-ion etching (Deep Silicon Etcher, Surface Technology Systems, Allenton, PA). Then, the PDMS prepolymer was prepared by thoroughly mixing a base monomer with a curing agent at a mass ratio of 10:1 and poured onto the surface of the silicon mold. After curing at 65 °C for 6 h, the PDMS mask layer was peeled from the silicon mold, cut into a square, and punched to form channel inlets and outlets. Finally, each of the prepared PDMS mask layers was stored at room temperature for future use.

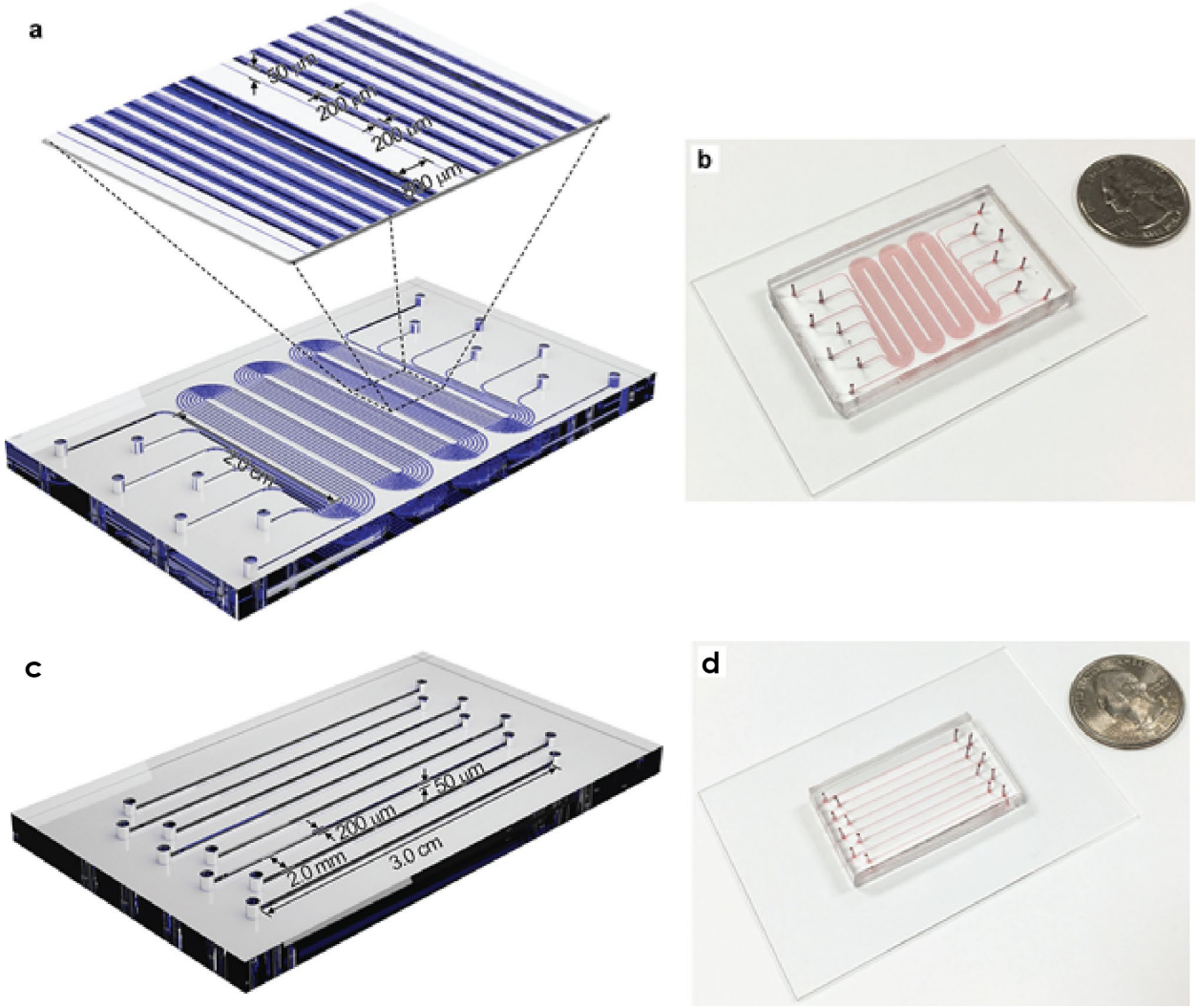

Figure 4.2 3D illustrations and photographs of PDMS mask layer used in this chapter. (a) 3D model and (b) photograph of the antibody-patterning PDMS mask layer used in this study. In (b), the antibody-patterning PDMS mask layer is attached on a glass substrate, and the microfluidic channels are loaded with red-colored gold nanoparticles. A US quarter is pictured next the PDMS mask layer to indicate scale. (c) 3D model and (d) photograph of the sample-flow PDMS mask layer used in this study. In (d), the sample-flow PDMS mask layer is attached on a glass substrate, and the microfluidic channels are loaded with red-colored gold nanoparticles. A US quarter is pictured next the PDMS mask layer to indicate scale.

4.2.2 Fabrication of multi-capture-antibody microarray chip

The multi-capture-antibody microarray chip was fabricated using a microfluidic patterning technique through a glutaraldehyde-mediated conjugation protocol.[6, 153] In a standard fabrication process, a glass slide was treated with Piranha solution (H_2O_2 (30%) / H_2SO_4 (98%) = 1/3, v/v) for 15 min, rinsed thoroughly with ultrapure water, and ultrasonicated in ethanol for 20 min. After drying in an oven at 65 °C for 10 min, the glass slide was put inside a clean glass bottle containing 200 μL of APTES. The bottle was placed in a vacuum vessel at room temperature for 3 days and then dried at 100 °C for 2 h, resulting in the formation of an amino-terminated silane monolayer on the glass surface. Subsequently, the antibody-patterning PDMS mask layer prepared above was non-permanently bonded onto the amino-silanized glass slide, and 8 μL of 100 nm AgNCs (0.01 nM) was loaded into the first channel at a flow rate of 2 μL min^{-1}. After incubation at room temperature for 10 min, the first channel was washed with ultrapure water. Then, 8 μL of 5% glutaraldehyde solution in 10 mM carbonate buffer (pH 9.6) was loaded into each of the remaining 6 channels at a flow rate of 2 μL min^{-1}. After incubation at room temperature for 6 h, the channels were washed with 10 mM carbonate buffer (pH 9.6), and 6 different types of anti-cytokine capture antibody solutions (8 μL, including anti-IL-1β, anti-IL-2, anti-IL-6, anti-IL-10, anti-TNF-□, and anti-IFN-γ capture antibodies at a concentration of 100 μg mL^{-1} in 10 mM carbonate buffer (pH 9.6)) were loaded into the 6 individual channels, respectively. After incubation at 4 °C overnight, the channels were washed with the carbonate buffer again, and 8 μL of 1% $NaBH_4$ solution in 10 mM carbonate buffer (pH 9.6) was loaded into each channel, followed by incubation at room temperature for 1 h. Afterwards, the channels were blocked with 8 μL of blocking buffer at room temperature for 1 h and then washed with washing buffer. This microfluidic patterning procedure leaded to the formation of 6 different meandering capture antibody stripes with 6 turns on a glass

substrate, along with a 100 nm AgNC stripe with the same shape. Following this, the antibody-patterning PDMS mask layer was removed from the glass substrate and immediately replaced with the sample-flow PDMS mask layer. The sample-flow microfluidic channels of the new PDMS layer were placed perpendicular to the capture antibody stripes. The channels were loaded with PBST containing 2% BSA, 5% sucrose, and 0.02% NaN_3. After incubation at room temperature for 2 h, the channels were washed with washing buffer and dried overnight at room temperature. Finally, the fabricated multi-capture-antibody microarray chip was stored at 4 °C for future use. This fabrication process resulted in the creation of 288 antibody arrays (200 μm × 200 μm) on the surface of the chip, which included 8 sample channels and 6 segments of 6 collocating parallel multiplex antibody arrays in each channel. In addition, there were also 6 AgNC arrays in each channel, which were used as references for locating the regions of antibody arrays.

4.2.3 Synthesis of the 100 nm AgNCs

The Ag NCs of ~42 nm in edge length were prepared using a one-pot synthesis method.[154] Initially, 6.0 mL of ethylene glycol (EG) was added into a glass vial and preheated at 150 °C under magnetic stirring for 60 min. Subsequently, 0.08 mL of 3.0 mM NaHS solution in EG, 1.5 mL of 20 mg mL^{-1} poly(vinylpyrrolidone) (PVP) solution in EG, and 0.5 mL of 48 mg mL-1 $AgNO_3$ solution in EG were sequentially added into the vial with a pipette. The reaction was allowed to proceed at 150 °C for 10 min and then quenched with an ice-water bath. The ~42 nm AgNCs were washed once with each acetone then ultrapure water, collected via centrifugation, and finally stored in 4.0 mL of EG for further use (~8.1 nM in particle concentration). Then, 3.0 mL of EG was added into a glass vial and preheated to 150 °C under magnetic stirring. After 25 min of preheating, 0.9 mL of 20 mg mL-1 PVP solution in EG, 0.2 mL of the ~42 nm AgNC seeds in EG, and 0.6 mL of 36 mg mL-1 $AgNO_3$ solution in EG were pipetted into the vial sequentially. The ~100 nm

AgNCs were obtained by cooling the reaction solution with an ice-water bath after the reaction had proceeded for ~90 min with the major extinction peak of the reaction solution reaching ~585 nm.[155] After being washed once with acetone and then ultrapure water via centrifugation, the ~100 nm AgNCs were stored in 4.0 mL of ultrapure water for future use (~0.4 nM in particle concentration).

4.2.4 Preparation of Anti-Cytokine Detection Antibody Conjugated 100 nm AgNCs (AgNC-DAb Conjugates)

The six AgNC-DAb conjugates were prepared by conjugating 100 nm AgNCs with six types of anti-cytokine detection antibodies using HS-PEG_{3400}-COOH and EDC/NHS as the linker and the coupling agents, respectively.[4, 153] In brief, 400 μL of 10 mg mL^{-1} HS-PEG_{3400}-COOH aqueous solution was mixed with 100 μL of the as-synthesized 100 nm AgNCs (0.4 nM), followed by incubation at room temperature for 5 h under gentle shaking. The mixture was then centrifuged at 1,000 rpm for 10 min, and the obtained precipitates (i.e., AgNC-S-PEG_{3400}-COOH) were washed twice with ultrapure water and dispersed in 300 μL of 10 mM phosphate-buffered saline (PBS, pH 7.4). Subsequently, 100 μL of 25 mM EDC aqueous solution and 100 μL of 50 mM NHS aqueous solution were simultaneously added into the AgNC-S-PEG_{3400}-COOH suspension. After incubation at room temperature for 20 min under gentle shaking, the nanoparticles (i.e., EDC/NHS-activated AgNC-S-PEG_{3400}-COOH) were washed three times with ultrapure water and dispersed in 400 μL of PBS. 100 μL of anti-cytokine detection antibody solution (at a concentration of 200 μg mL-1) was added into the nanoparticle suspension and incubated at 4 °C overnight with gentle shaking. Thereafter, 200 μL of 10% BSA in PBS was added into the nanoparticle suspension and incubated at room temperature for 60 min. After centrifugation, the products (i.e., AgNC-DAb

conjugates) were dispersed in 100 μL of PBS containing 0.05% Tween 20, 1% BSA, and 0.02% NaN_3, and were finally stored at 4 °C for future use (0.4 nM).

4.2.5 Convolutional neural network (CNN) training

The architecture of the CNN contains a downsampling process from a 512×512 dark-field AgNC image for category classification (nanoparticles as class "1", background as class "0"), and an upsampling process for nanoparticle segmentation. The downsampling process consists of 6 layers, including an image input layer, two convolution 2D layers (Conv2D, 6 filters, kernel of 3 × 3), two rectified linear unit layers (ReLU), and one max-pooling layer (stride of 2). The upsampling process consists of 5 layers, including one transposed convolution 2D layer (Trans Conv2D), one ReLu layer, one Conv2D layer, one softmax layer, and one pixel classification layer which contains class weight balance.

The training of the CNN involves dataset labeling, class weight balance, network training, and result evaluation. **Figure 4.3** shows the schematic of the data annotation workflow for training dataset labeling. For the training dataset, we selected 252 representative dark-field images that covered a wide range of cytokine concentrations from assay blank, 0 pg mL^{-1} to 10,000 pg mL^{-1}. To enhance the dataset labeling speed, we wrote a thresholding algorithm that computed a global threshold T from a grayscale image, using Otsu's method.[156] Using this global threshold together with the standard image erosions and dilations, we labeled the recognized AgNC spot pixel as class "1" and the background pixel as class "0" to generate a binary image mask called "Labeled image". Note that this labeled image was still preliminary and failed to detect the AgNC spots that had large intensity variance or that were aggregated. We then used several correction algorithms to manually add or remove the falsely recognized area. We used a 5×5 pixel unit size for normalizing the labeling of all the recognized AgNC spots including individual, aggregated, bright,

and dim spots. In addition to the average individual spots, this normalization labeling process will not only help the neutral network to recognize the very deem spots but also be able to separate the aggregated spots with strong intensity compared to the global thresholding method (Otsu's Method). The human corrected "Labeled image" was later used to train the neural network. In addition, we considered the class weight balance using the inverse frequency weighting method which gives more weight to less frequently appearing classes (AgNC class). The class weight was defined as

$$\text{Classweight} = \frac{N_{image\ total\ pixels}}{N_{class\ pixels}} \quad (2)$$

where Nimage total pixels is the number of total image pixels of 512×512 = 262,144, and the Nclass pixels is the number of pixels for each class. This class weighting strategy was added into the neural network training process to enhance the pixel identification accuracy because the number of AgNC class pixels was significantly smaller than the number of background pixels. For the network training options, we used the stochastic gradient descent with momentum (SGDM) algorithm to minimize the loss function and set the total epoch number to be 200 with 20 samples for each mini-batch. We then selected four candidate networks with training accuracy above 98% and further evaluated their performance using 126 well-selected test images and then finalized the currently used CNN. Finally, the pre-trained CNN algorithm was integrated into the developed CNN-based image processing method and applied to recognize all the area of AgNC spots in an image. The AgNC spot number (i.e., particle number) in the image as the final output result was simply calculated by area-size sorting, which is equal to the recognized AgNC spot area divided by the 5×5 pixel unit size.

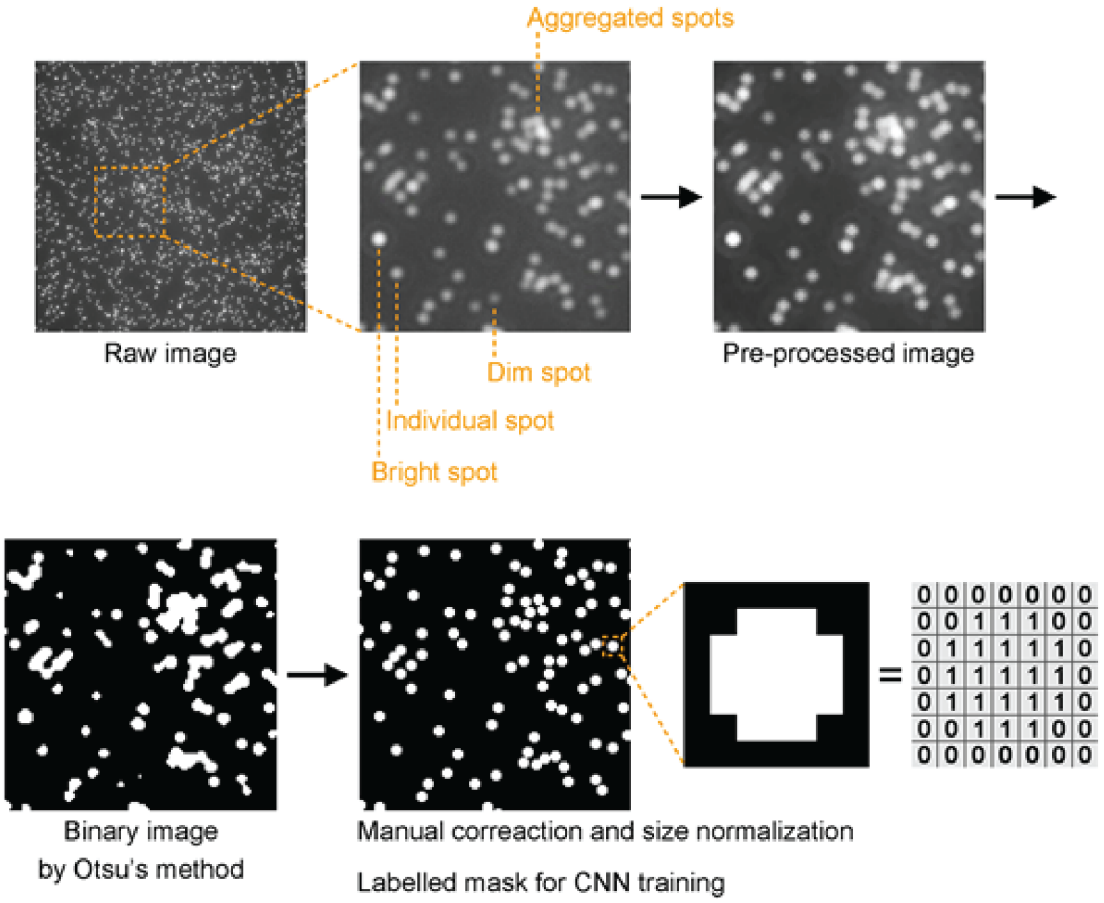

Figure 4.3 Schematic of the data annotation workflow for labeling training images.

4.2.6 Machine-learning assisted microfluidic nanoplasmonic digital immunoassay assay protocol

Prior to detection, multi-cytokine standards with various concentrations (ranging from 0 to 10,000 pg mL^{-1}) were prepared by dissolving IL-1β, IL-2, IL-6, IL-10, TNF-α, and IFN-γ together in PBS containing 0.05% Tween 20 and 1% BSA (dilution buffer), and a mixed AgNC-DAb conjugate solution (0.1 nM) was prepared by dissolving the same amounts of the as-prepared six types of AgNC-DAb conjugates together in dilution buffer. In a standard detection procedure, 3 μL of the multi-cytokine standards or human serum samples was mixed with 3 μL of the AgNC-DAb conjugate mixture (0.1 nM) and loaded into the multi-antibody microarray chip. After incubation at room temperature for 60 min, the channels were washed with PBST. The images of

the antibody arrays in each channel were semi-automatically taken using a dark-field LSPR microscope for ~25 min to complete the acquisition of the 288 images. The number of AgNCs on each image was recorded as the detection signal using the CNN-based image processing method and took ~30 seconds to process the 288 images. A view area of 138 μm × 138 μm (center part) from the 200 μm × 200 μm antibody arrays was captured as the detection results for analysis to ensure a high quality of obtained single-particle nanoplasmonic scattering images and to avoid the background scattering signals and interference from the PDMS layer along the edge of the microfluidic channel.

4.2.7 Cytokine concentrations measured by commercialized ELISA kits.

The detection was performed according to the protocol provided by the manufacturer Fisher Scientific, Inc. The cytokines detected in this experiment included IL-1β, IL-2, IL-6, IL-10, TNF-α, and IFN-γ. Briefly, 100 μL of cytokine standards or human serum samples was initially added into appropriate wells of the microplate, whose surface was immobilized with anti-cytokine capture antibodies. Then, 50 μL of biotin-modified anti-cytokine detection antibody was added into each well. After incubation at room temperature for 2 h, the wells were washed five times with washing buffer, and 100 μL of streptavidin-modified horseradish peroxidase was added, followed by incubation at room temperature for 30 min. After washing five times, 100 μL of 3,3',5,5'-tetramethylbenzidine (TMB)-H_2O_2 substrate solution was added. After 20-min incubation at room temperature, 100 μL of stop solution (2 M H_2SO_4) was added to each well. The absorbance of each well was read at 450 nm using a microplate reader.

4.2.8 Characterizations

AFM images, TEM images, and SEM images were taken using a neaSNOM microscope, a Zeiss EM10 transmission electron microscope, and a JEOL JSM-7000F microscope, respectively. DLS data was obtained using a Zetasizer Nano ZS90, Malvern. The dark-field images and scattering spectra of samples were recorded using an upright dark-field microscope (Eclipse Ni-U, Nikon) outfitted with an electron-multiplying charge-coupled device (EMCCD, Photometrics) camera and a spectrometer (HR4000, Ocean Optics). Polarized light from a 100 W halogen lamp (NI-LH, Nikon) was epi-illuminated onto samples via an oil immersion dark-field condenser (C-DO, Nikon). A crossed polarizer was used to reduce the background contribution from substrate-scattered light. The light scattered from samples was collected by a 60× objective lens (Plan Pro, Nikon), imaged by the EMCCD camera, and recorded using the NIS-Element BR analysis software. The obtained images were analyzed by a customized Matlab program. The absorbance of samples in microplates was read using a SpectraMax M5 Multi-Mode Microplate Reader (Molecular Devices).

4.2.9 Finite element method (FEM) simulation

The FEM simulation was performed on a single 100 nm AgNC for the calculation of its scattering cross-section spectrum using COMSOL. In this simulation, an electromagnetic pulse with the wavelength ranging from 400 to 800 nm was launched into a box containing a single AgNC. The AgNC and its surrounding space were divided into 1-nm meshes. The refractive index of the surrounding medium was set to be the same as that of water, 1.33. The dielectric function of Ag was taken from a previously measured value.[157] The AgNC was modeled as a cube of 100 nm in edge length with rounded edges and corners of 13-nm radii, according to the TEM data.

4.3 Results and Discussion

4.3.1 Design and principle of machine-learning-assisted microfluidic nanoplasmonic digital immunoassay

Figure 4.4 illustrates the sensing principle of the machine-learning-assisted microfluidic nanoplasmonic digital immunoassay for multiplex cytokine detection. Interleukin-1 beta (IL-1β), interleukin-2 (IL-2), interleukin-6 (IL-6), interleukin-10 (IL-10), tumor-necrosis-factor alpha (TNF-α), and interferon-gamma (IFN-γ) are selected as the target cytokines due to their abnormal expression levels in the serum of COVID-19 patients.[122-124] The proposed immunoassay consists of three main components: a multi-capture-antibody microarray chip for the microfluidic immunoassay (**Figure 4.4a**), detection-antibody-conjugated 100 nm AgNCs (AgNC-DAb conjugates) for nanoplasmonic digital imaging (**Figure 4.4b**), and a machine-learning-based image processing method for digital signal counting (**Figure 4.4c**). The antibody microarray chip contains 8 parallel microfluidic sample channels (300 nL sample volume for each channel), which lie perpendicular to the 6 meandering capture antibody stripes with 6 turns on a glass substrate. This chip is thus designed to allow a 6-plex cytokine detection with 6 segments of parallel collocating antibody arrays in each channel and a total array of 288 square immunosensing areas (200 × 200 μm) for the entire chip. It should be noted that a reference stripe of pristine 100 nm AgNCs is added in parallel to the capture antibody stripes for easy localization of the antibody microarrays under dark-field imaging and provision of reference signals. The microfluidic immunoassay is carried out using a rapid one-step sandwich format. The AgNC-DAb conjugates with the six cytokine detection antibodies are mixed with the target samples and then introduced into the microfluidic immunoassay system, forming six types of sandwiched immunocomplexes (i.e., capture antibody/cytokine/detection-antibody-AgNC) on their corresponding capture

antibody arrays (**Figure 4.4a**). The 100 nm AgNCs are selected as the labeling reagent to provide the light-scattering signal for nanoplasmonic digital imaging (**Figure 4.4b**) owing to the following four important advantages: (i) they can be readily produced with ultra-high purity and uniformity, ensuring good reproducibility of the immunoassay;[154, 158] (ii) they show excellent stability in assay buffers during the functionalization, reaction, and imaging processes, offering high robustness for the immunoassay;[140, 159] (iii) they can be readily modified with functional groups like -COOH through Ag-thiol bonding for antibody conjugations with tunable configurations;[159] and (iv) most importantly, they could provide extremely intense light-scattering signals under dark-field imaging with superior signal-to-noise ratio, enabling record high sensitivity for the nanoplasmonic cytokine immunoassay.[151] The image of every capture antibody array (288 images in total) is taken using an EMCCD camera under a dark-field microscope, and the number of the captured AgNCs on the surface of each antibody array is counted using the machine-learning-based image processing method, which can be converted to the concentrations of target cytokines accordingly (**Figure 4.4c**). The machine-learning-based image processing method is a customized MATLAB code developed using convolutional neural network (CNN) algorithm. The CNN method can process the dark-field image data automatically, distinguish the detection signals (i.e., the scattering spots of AgNCs) from background noise precisely, and provide rapid analysis of the particle number of AgNCs with high statistical accuracy and throughput. Such an efficient image processing method dramatically reduces the time required for data analysis and thus enables the practical application of the nanoplasmonic digital imaging technology for cytokine profiling.

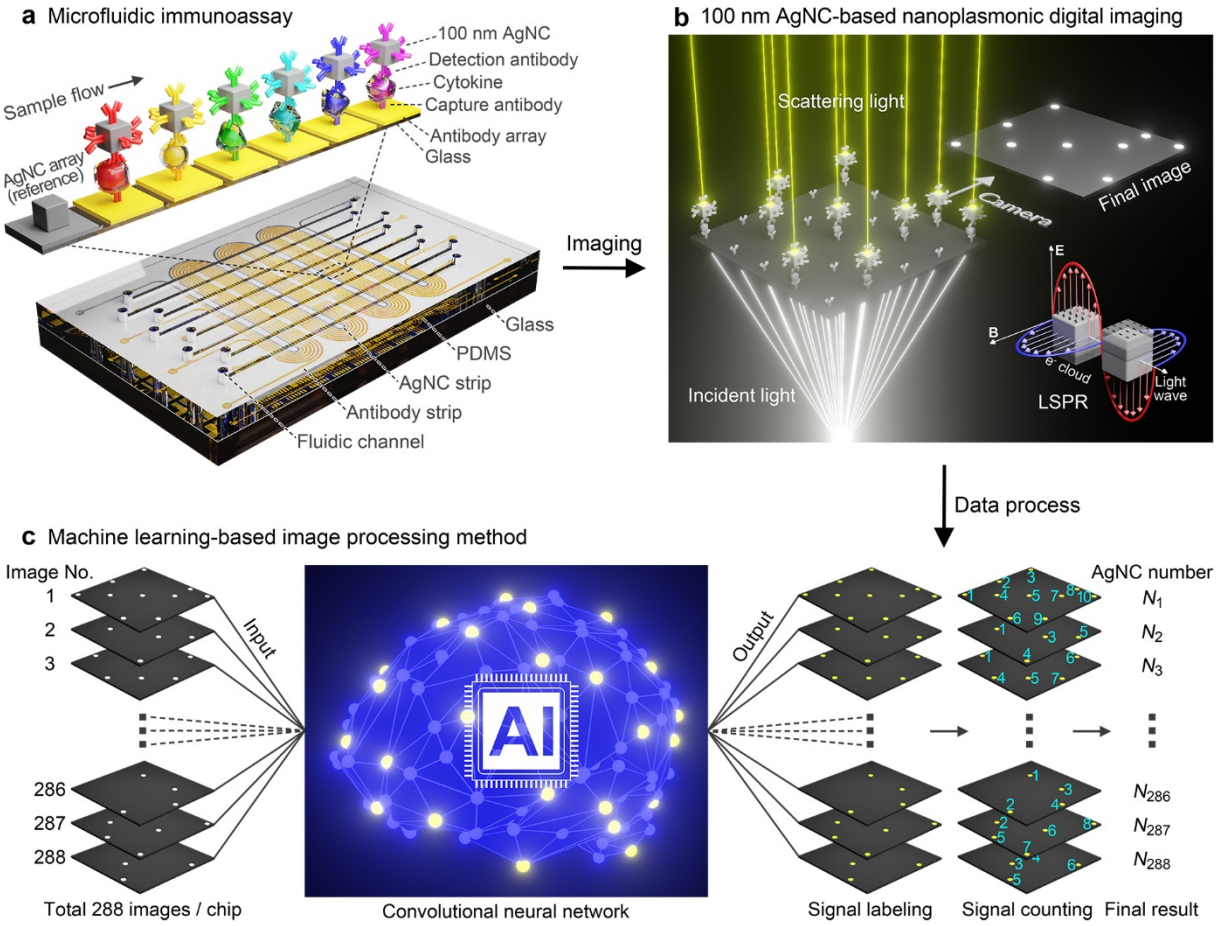

Figure 4.4 Schematic illustration of the machine-learning-assisted microfluidic nanoplasmonic digital immunoassay for high throughput, multiplex cytokine detection (including IL-1β, IL-2, IL-6, IL-10, TNF-α, and IFN-γ). The immunoassay involves three key components: the microfluidic immunoassay platform (a), the nanoplasmonic digital imaging technology (b), and the machine-learning-based image processing method (c).

4.3.2 Fabrication and characterization of microfluidic nanoplasmonic digital immunoassay

The multi-capture-antibody microarray chip was fabricated using a microfluidic flow-patterning technique.[6] Briefly, an amino-modified glass substrate was patterned with 6 different meandering capture antibody stripes using a PDMS mask layer via a glutaraldehyde-mediated conjugation protocol.[153] Subsequently, a sample-flow PDMS layer was attached onto the glass

substrate perpendicularly to the 6 capture antibody stripes, resulting in a micromosaic immunoassay for the multi-capture-antibody microarray chip. **Figure 4.5 a-b** shows the AFM topographic images of the surface of the glass substrate before and after the antibody microarray fabrication. It can be observed that the surface of the glass substrate became rougher after the immobilization of capture antibodies, suggesting the presence of antibodies on the microarray surface. We also acquired the AFM phase images of the same region of the antibody microarray to further verify the surface functionalization. As shown in **Figure 4.5 c-d**, the texture of the antibody microarray surface presented a uniformly distributed needle-like texture with a higher phase angle compared to that of a clean glass substrate, due to the much softer feature of antibodies compared with the glass.[160-161] These results confirm the successful immobilization of uniformly distributed antibodies on the surface of the glass substrate for the multi-capture-antibody microarray chip.

We then synthesized 100 nm AgNCs using a seed-mediated growth method and functionalized them with the six different detection antibodies to produce the AgNC-DAb conjugates as the signal transducers.[158] As shown by the TEM images of the 100 nm AgNCs obtained from a batch of the standard synthesis (**Figures 4.5e**), the AgNCs displayed a uniform size distribution and well-defined cubic shapes. The edge length of the AgNCs synthesized from this batch was measured to be 100.3 × 4.8 nm by analysis of 300 randomly selected nanoparticles. Meanwhile, the edge length of the AgNCs synthesized from three different batches were analyzed to be 100.6 ± 5.4 nm. The coefficient of variation of the edge length for the inter-batch measurement (n=3) was calculated to be as low as 5.4%, indicating that the AgNCs can be readily reproduced with high uniformity. In addition, the amount (4 mL at 0.4 nM) of 100 nm AgNCs obtained per batch of the standard synthesis could allow up to 5333 microfluidic nanoplasmonic digital immunoassay (3 μL of 0.1

nM per assay) as proposed ((4 mL × 0.4 nM) / (3 μL × 0.1 nM) = 5333). The synthesis process could be scaled up by 10 times to produce a much larger quantity of the AgNCs per batch without compromising the sample quality, making it possible for large-scale production of the digital immunoassay. The 100 nm AgNCs were deposited on a glass substrate for characterization under dark-field imaging, and their representative dark-field image and scattering spectrum were taken and recorded as shown in **Figure 4.5f-g**, respectively. The AgNCs exhibited extremely strong light-scattering with a major plasmonic scattering peak at ~568 nm. The scattering cross-section was calculated to be as high as 1.04×10^5 nm^2 according to the finite element method (FEM) simulation, which is the highest among various nanoscale optical materials with dimensions smaller than 100 nm.[162] More importantly, each of the scattering spots under dark-field imaging (**Figure 4.5f**) represented one isolated AgNC, confirmed by the SEM image of the same region (insets in **Figure 4.5f**). The AgNCs displayed similar scattering intensity and resonance spectra, indicating the successful synthesis of high-quality AgNCs with extremely intense and highly uniform single-particle scattering characteristics. Furthermore, the synthesized AgNCs can be stored in DI water at room temperature for at least 18 months without significant changes to the size, shape, and the plasmonic properties, revealing the high storage stability of our AgNCs. Following that, the as-synthesized AgNCs were modified with HS-PEG_{3400}-COOH on their surfaces, and then conjugated with anti-cytokine detection antibodies via EDC/NHS chemistry.[4, 153] To verify the successful conjugation of the AgNC-DAb, we performed DLS to measure the hydrodynamic sizes of the AgNCs before and after the antibody functionalization, showing an evident increase from 136.7 nm to 157.9 nm (**Figure 4.5h**). The size increase suggests the presence of antibodies on the surface of the AgNCs as the mean size of common immunoglobulin antibodies is ~11 nm.[163] It is worth noting that the light-scattering behavior of AgNCs was very well preserved

after the conjugation of detection antibodies and can be stored for more than 6 months, devising the AgNC-DAb conjugates as the labelling reagent for the nanoplasmonic immunoassay. Here, the 100 nm Ag nanocubes were intentionally employed in our sandwich nanoplasmonic digital biosensor instead of Au nanorods, which have been widely utilized in many previous reported label-free nanoplasmonic digital biosensors.[142-147] This is mainly because of the completely two different sensing principles between these nanoplasmonic digital biosensors. Label-free nanoplasmonic biosensors primarily rely on the refractive index change surrounding the plasmonic nanomaterials before and after target binding. Au nanorods with an anisotropic shape exhibit a LSPR that is highly sensitive to the local refractive index and thus are more suitable for label-free sensing. While our sandwich nanoplasmonic digital biosensor requires strong single-particle scattering signals from the captured plasmonic nanomaterials after the formation of the sandwich immune complexes. The 100 nm Ag nanocubes with a symmetric geometry and much larger scattering cross-section provide highly stable and intense scattering signals, rendering them the ideal plasmonic nanomaterials for high-quality single-particle imaging in our sandwich nanoplasmonic digital sensing.

To demonstrate the feasibility of the as-proposed microfluidic nanoplasmonic digital immunoassay, we evaluated the platform in response to a mixed cytokine solution containing IL-1β, IL-2, IL-6, IL-10, TNF-α, and IFN-γ at a concentration of 100 pg mL^{-1}. The cytokine solution was mixed with the AgNC-DAb conjugates and then injected into the microfluidic sample channel for 60-min incubation. The images of the multi-antibody arrays before and after the assay were obtained using a dark-field microscope. The antibody arrays showed a very clean background with no scattering signals detected before sample loading (**Figure 4.5i(*i*)**). After the detection, numerous of bright spots were observed on the surface of the multi-antibody microarrays (**Figure**

4.5i(*ii*)), which originated from the single-particle light-scattering of the AgNCs due to the sandwich immunocomplex formation. The number of the scattering spots (i.e., particle numbers of AgNCs) on the antibody microarrays of IL-1β, IL-2, IL-6, IL-10, TNF-α, and IFN-γ were counted to be 251.0 ± 10.8, 482.0 ± 19.1, 490.2 ± 15.7, 189.0 ± 7.3, 361.8 ± 14.7, and 221.2 ± 7.7 (n = 6), respectively (**Figure 4.5j(*ii*)**). In contrast, the spot numbers on the microarrays for the detection of blank cytokine solution (0 pg mL^{-1}) were counted to be 2.0 ± 0.9, 2.8 ± 0.8, 2.5 ± 0.5, 2.0 ± 0.6, 2.3 ± 0.8, and 2.2 ± 0.4 (n = 6), respectively (**Figure 4.5i(*iii*), j(*iii*)**), suggesting negligible non-specific signals for the immunoassay.

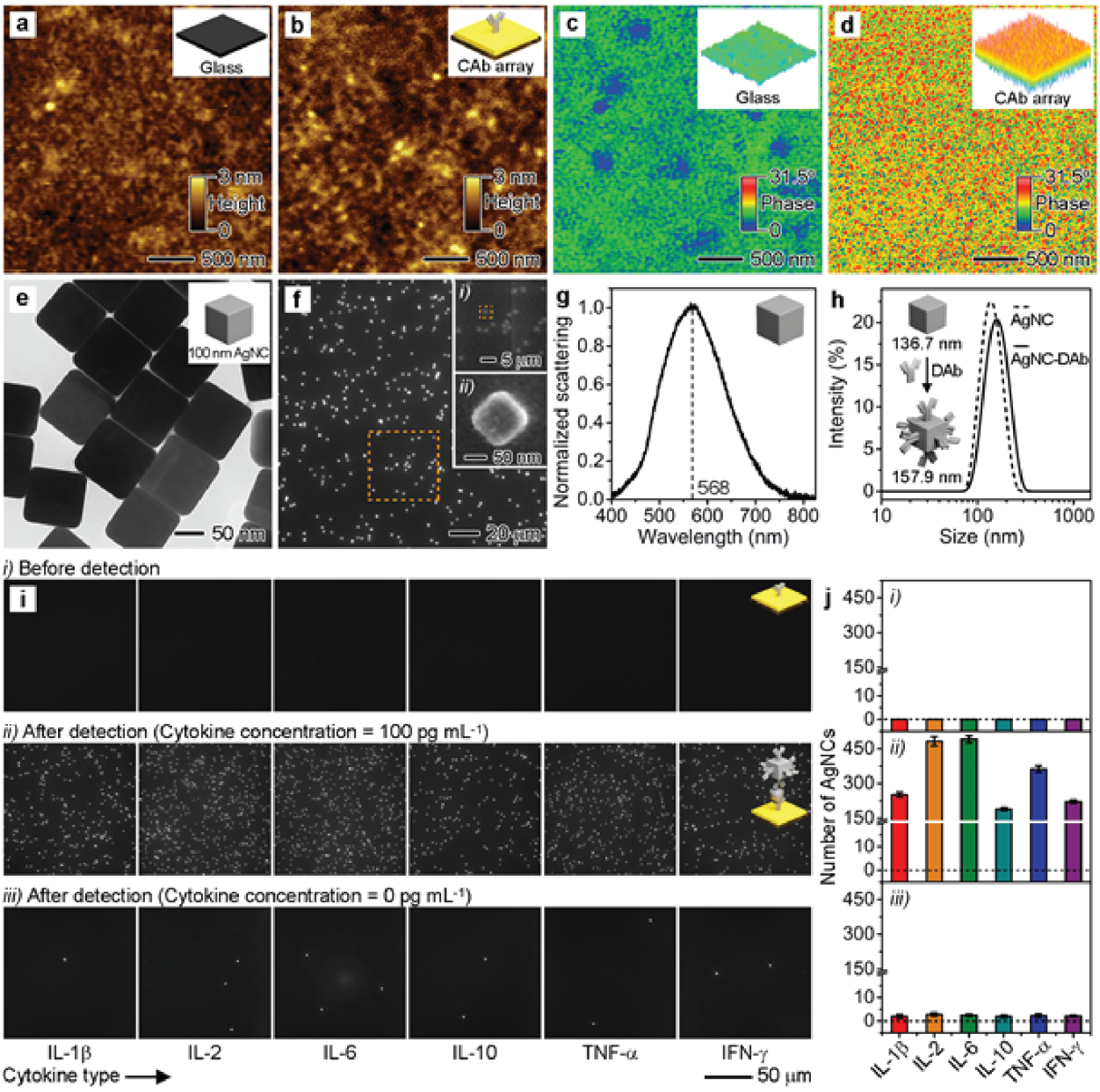

Figure 4.5 Characterization of the microfluidic nanoplasmonic digital immunoassay. (a-d) AFM topographic (a,b) and phase (c,d) images of the surfaces of glass substrates before (a,c) and after (b,d) the immobilization of capture antibodies. Insets in a-d show the corresponding images in three-dimensional (3D) models. (e) TEM image of AgNCs with an average edge length of 100 nm. (f,g) Dark-field image (f) and scattering spectrum (g) of 100 nm AgNCs deposited on a glass substrate. In (f), Insets (i) and (ii) show the SEM images taken on the region marked by a yellow

box in (f) and Inset (i), respectively. (h) DLS size distribution of 100 nm AgNCs (dashed curve) and AgNC-DAb conjugates (solid curve) dispersed in ultrapure water. (i) Dark-field images of antibody microarrays taken before the detection of cytokines (i) and after the detection of 100 pg mL-1 (ii) and 0 pg mL-1 (iii) cytokines. (j) Bar graph showing the intensity of the detection signal (i.e., particle number of AgNCs) obtained from (i).

4.3.3 Machine-learning-based image processing method for nanoplasmonic digital counting

To achieve rapid and high-throughput cytokine detection for real sample measurement, the nanoplasmonic digital immunoassay ultimately requires a simple, accurate, and ultrafast image processing method that can automatically identify and count the captured AgNCs on the 288 multi-antibody microarrays per chip. More importantly, the signal counting process needs to clearly distinguish the detection signals (i.e., the scattering spots of AgNCs) from false signals/background noise (including aggregated/neighboring spots) and acquire the desired readout in a large scattering intensity variance (including bright and dim spots). Manual counting of the particle number of AgNCs on each image by human eyes is cumbersome and time-consuming, apparently impractical for high-throughput imaging analysis. Commercial software (e.g., ImageJ and Image-Pro Plus) and conventional image processing methods (e.g., global thresholding and segmentation (GTS)) are limited mainly by poor accuracy in recognizing the aggregated/neighboring and dim spots on the dark-field images, yielding a low signal-to-noise ratio in the immunoassay. To address this issue, we developed a machine-learning-based image processing method using convolutional neural network (CNN) visualization for particle counting (named "CNN method").[164-166] **Figure 4.6a** shows the algorithm architecture of the CNN method. It involves dark-field image data read-in/pre-processing (including noise filtering and contrast enhancement), detection signal/background image segmentation by pre-trained CNN, post-

processing, and result output. CNN as the key component was pre-trained to classify and segment image pixels by labels of the detection and background signals. **Figure 4.6b** shows three representative images acquired by our digital immunoassay with AgNC spot numbers ranging from low to high levels, and the corresponding image processing results obtained by Image-Pro Plus, GTS, and CNN methods. As indicated by **Figure 4.6b**, all three methods could accurately count the detection signals for the monodispersed bright spots at a low AgNC count. However, Image-Pro Plus and GTS methods fall short in precise image labeling and accurate signal counting for the aggregated/neighboring and dim spots compared to the CNN method, especially at high AgNC counts. To further verify the accuracy of our CNN method, we analyzed 288 test images containing different particle numbers of AgNCs in the range of 0-2,000. It should be noted that these images were different from those used for CNN training. The obtained counting results were compared with those analyzed by Image-Pro-Plus-assisted manual counting as the benchmark. As shown in **Figure 4.6c(*i*)**, the AgNC counts from the two methods display an excellent linear regression with a slope of 0.9902, a small intercept of 3.1140, and a coefficient of determination of $R^2 = 0.9972$. It is worth pointing out that the accuracy of our CNN-based method could be further improved with the AgNC number in the range of 0-800 (Slope = 1.0004, Intercept = -0.2588, and $R^2 = 0.9998$; **Figure 4.6c(*ii*)**), which was later determined to be the linear range of detection for our digital immunoassay. Moreover, the CNN image processing shows excellent accuracy and consistency for analysis of images acquired from different experiments performed on different days, indicating the high robustness of our CNN method. Notably, it only took ~30 seconds to process a total of 288 images obtained from one immunoassay chip and produce the corresponding detection results (central processing unit (CPU): AMD Ryzen 5 1600 Six-Core Processor) using the customized MATLAB code. In contrast, the Image-Pro-Plus-assisted manual

counting method requires up to ~6,000 times as long (~50 h) to accomplish the same task with much more complicated procedures.

In addition, as seen from the dark-field images in **Figure 4.6b** and many other dark-field images in this study (especially those with high densities of AgNC scattering spots), the spots in certain regions were much bigger and brighter than other "normal" spots (spots in average), and some of them were in irregular shapes in comparison to those with rounded shapes. These phenomena could be ascribed to the known Abbe diffraction limit, where a diffuse spot can be formed when two objects are in close proximity (distance shorter than ~200 nm).[167-168] Therefore, those bigger, brighter, and non-circular spots might consist of multiple AgNC particles, resulting in underestimation of the AgNC counting in the images. With the advancement in super-resolution nanoplasmonic imaging and enhanced CNN algorithm for in-depth information on spot brightness and size, we believe the CNN image processing could break the fundamental limit and become an enabling method for simple, rapid, accurate, robust and high throughput digital counting in nanoplasmonic digital immunoassay and many other imaging analysis applications.[148]

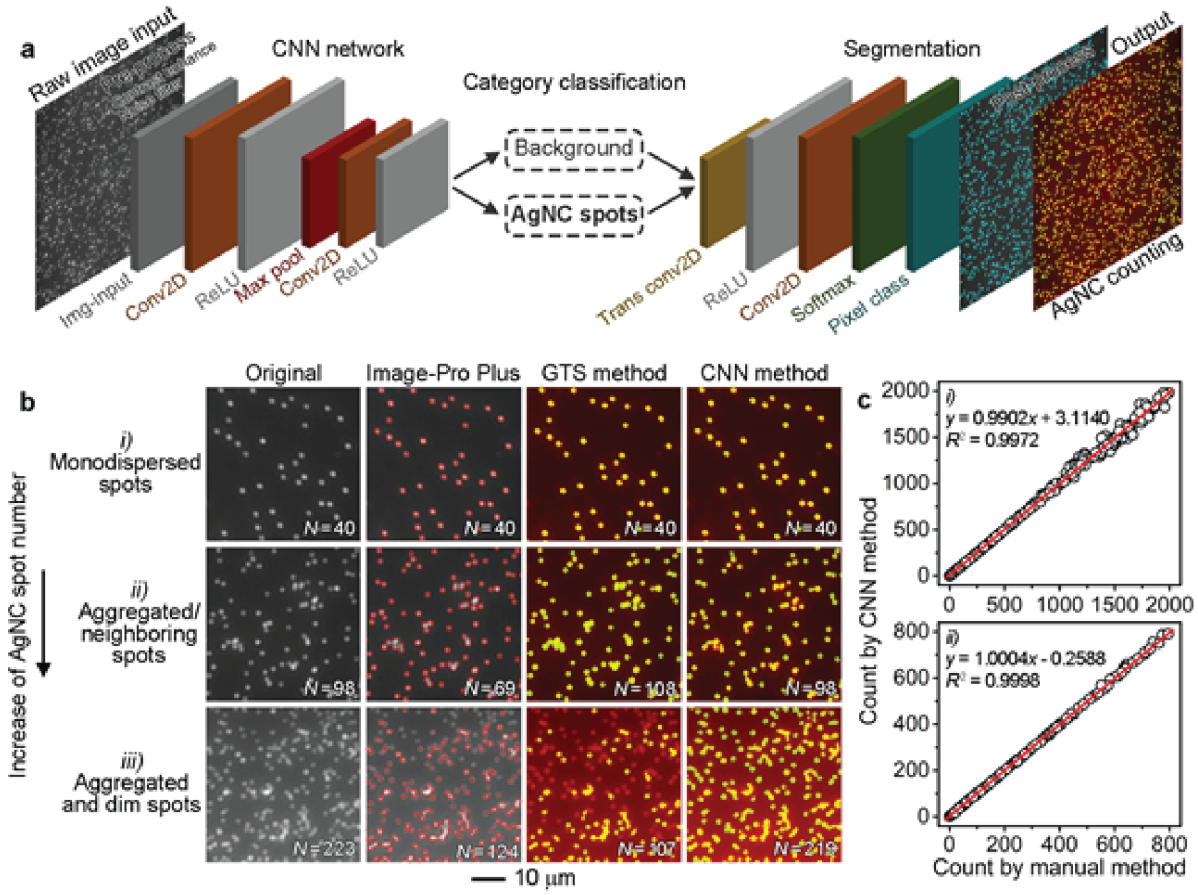

Figure 4.6 Evaluation of CNN method for counting particle numbers of AgNCs. (a) Schematics showing the algorithm architecture of the CNN method, where Img-input is the image input layer, Conv2D is the convolution 2D layer, ReLU is the rectified linear unit layer, Max pool is the max pooling 2D layer, Trans conv2D is the transposed convolution 2D layer, Softmax is the softmax layer, and Pixel class is the pixel classification layer. (b) Three representative images were obtained from our digital immunoassay with AgNC spot number ranging from low to high and their corresponding image processing results obtained by Image-Pro Plus, GTS, and CNN methods. Note that: (*i*) when the AgNC spot number was low, the spots were monodispersed on the image; (*ii*) with the increase of the AgNC spot number, some of the spots became aggregated; and (*iii*) at very high number of AgNCs, some of the spots became dim in addition to aggregated. (c) Correlation analysis between the CNN method and standard Image-Pro-Plus-assisted manual

counting method in counting AgNC number in the ranges of 0-2,000 (*i*) and 0-800 (*ii*) from 288 test images.

4.3.4 Analytical performance of machine-learning-assisted microfluidic nanoplasmonic digital immunoassay

Prior to evaluation of the analytical performance of the immunoassay, the experimental procedures were optimized to inject a concentration of 0.1 nM for AgNC-DAb conjugates and incubate with target analytes for 60 min for thorough antigen-antibody reaction (**Figure 4.7**). The evaluation was then carried out using the following standard detection procedures: (i) the multi-antibody microarray chip was incubated with a mixture containing multi-cytokine standards (or samples) and AgNC-DAb conjugates at room temperature for 60 min; and (ii) after the incubation and washing, the images of multi-antibody microarrays were recorded using a dark-field microscope and then analyzed by the CNN-based image-processing algorithm. We evaluated the analytical performance including the sensitivity, sensing dynamic range, reproducibility, specificity, and cross-reactivity for the nanoplasmonic digital immunoassay.

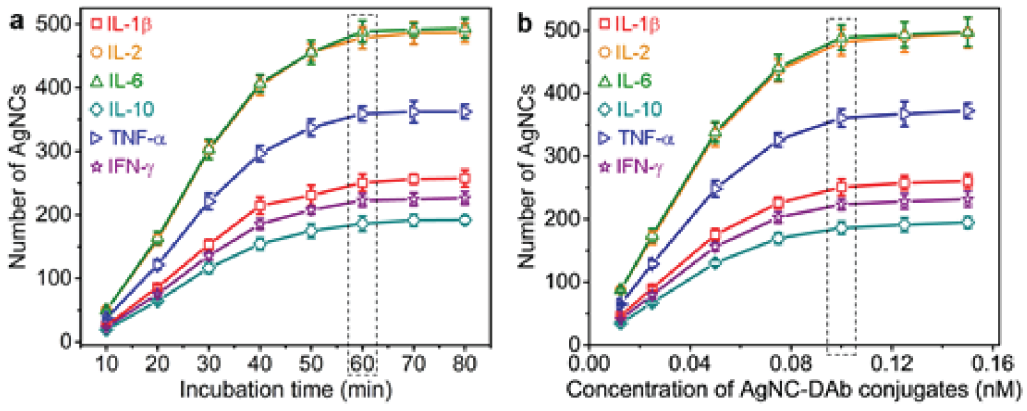

Figure 4.7 Optimization of the experimental conditions for the proposed immunoassay. Effects of (a) incubation time for antigen-antibody reaction and (b) concentration for 100 nm AgNC-DAb

conjugates on the sensitivity of the immunoassay. In all experiments, a 100 pg mL^{-1} cytokine standard was chosen as an example for optimization of the detection system. To make the proposed system more applicable in practical clinical applications, room temperature (~25 °C) was chosen as the operating temperature throughout all the experiments. All other conditions were kept the same as those in the standard detection procedure.

We first determined the sensitivity and dynamic range of the immunoassay by analyzing multi-cytokine standards containing IL-1β, IL-2, IL-6, IL-10, TNF-α, and IFN-γ at different concentrations. **Figure 4.8a** shows the dark-field images of the final multi-antibody microarrays for detection of multi-cytokine standards ranging in concentration from 0 to 10,000 pg mL^{-1}. It can be seen that for each type of cytokine, the number of scattering spots of AgNCs on the multi-antibody microarray increased as the cytokine concentration increased. By plotting the particle number of AgNCs as the detection signal against the cytokine concentration, calibration curves for the six target cytokines were established (**Figure 4.8b-g**). We can clearly and distinctly differentiate positive detection signals for all six cytokines in the concentration range of 1-10,000 pg mL^{-1} (4 orders of magnitude), suggesting a wide response range of the immunoassay for multiplex cytokine detection. As indicated by the insets of **Figure 4.8b-g**, high-quality linear relationships were observed in the ranges of 1-200 pg mL^{-1} for IL-1β (R^2 = 0.998), 1-100 pg mL^{-1} for IL-2 (R^2 = 0.999), 1-100 pg mL^{-1} for IL-6 (R^2 = 0.999), 1-200 pg mL^{-1} for IL-10 (R^2 = 0.995), 1-200 pg mL^{-1} for TNF-α (R^2 = 0.998), and 1-200 pg mL^{-1} for IFN-γ (R^2 = 0.998). Here, different slopes of the calibration linear curves (insets in **Figure 4.8b-g**, 2.489 mL pg^{-1} for IL-1β, 4.768 mL pg^{-1} for IL-2, 4.916 mL pg^{-1} for IL-6, 1.805 mL pg^{-1} for IL-10, 3.462 mL pg^{-1} for TNF-α, and 2.274 mL pg^{-1} for IFN-γ) were obtained that could be explained by the difference in cytokine-antibody binding affinities and the cytokines molar masses. The higher cytokine-antibody affinities could

allow more binding for the immune sandwich formation, leading to more AgNC scattering spots on the sensing arrays and thus steeper slopes in the calibration linear curves. While for cytokines with lower molar masses, larger binding possibilities driven by the higher molar concentrations (under the same mass concentration) are anticipated, resulting in more AgNC counting and corresponding slope difference. By comparing the slopes of the calibration curves ($Slope_{IL\text{-}6} > Slope_{IL\text{-}2} > Slope_{TNF\text{-}\alpha} > Slope_{IL\text{-}1\beta} > Slope_{IFN\text{-}\gamma} > Slope_{IL\text{-}10}$) and the molar masses of the cytokines ($M_{IL\text{-}2}$ (15.5 kDa) < $M_{IFN\text{-}\gamma}$ (16.7 kDa) < $M_{IL\text{-}1\beta}$ (17.3 kDa) < $M_{TNF\text{-}\alpha}$ (17.4 kDa) < $M_{IL\text{-}10}$ (18.6 kDa) < $M_{IL\text{-}6}$ (20.9 kDa), we did not observe a strong correlation between these two factors, indicating the cytokine molar mass effect on the calibration slope values could be ruled out.

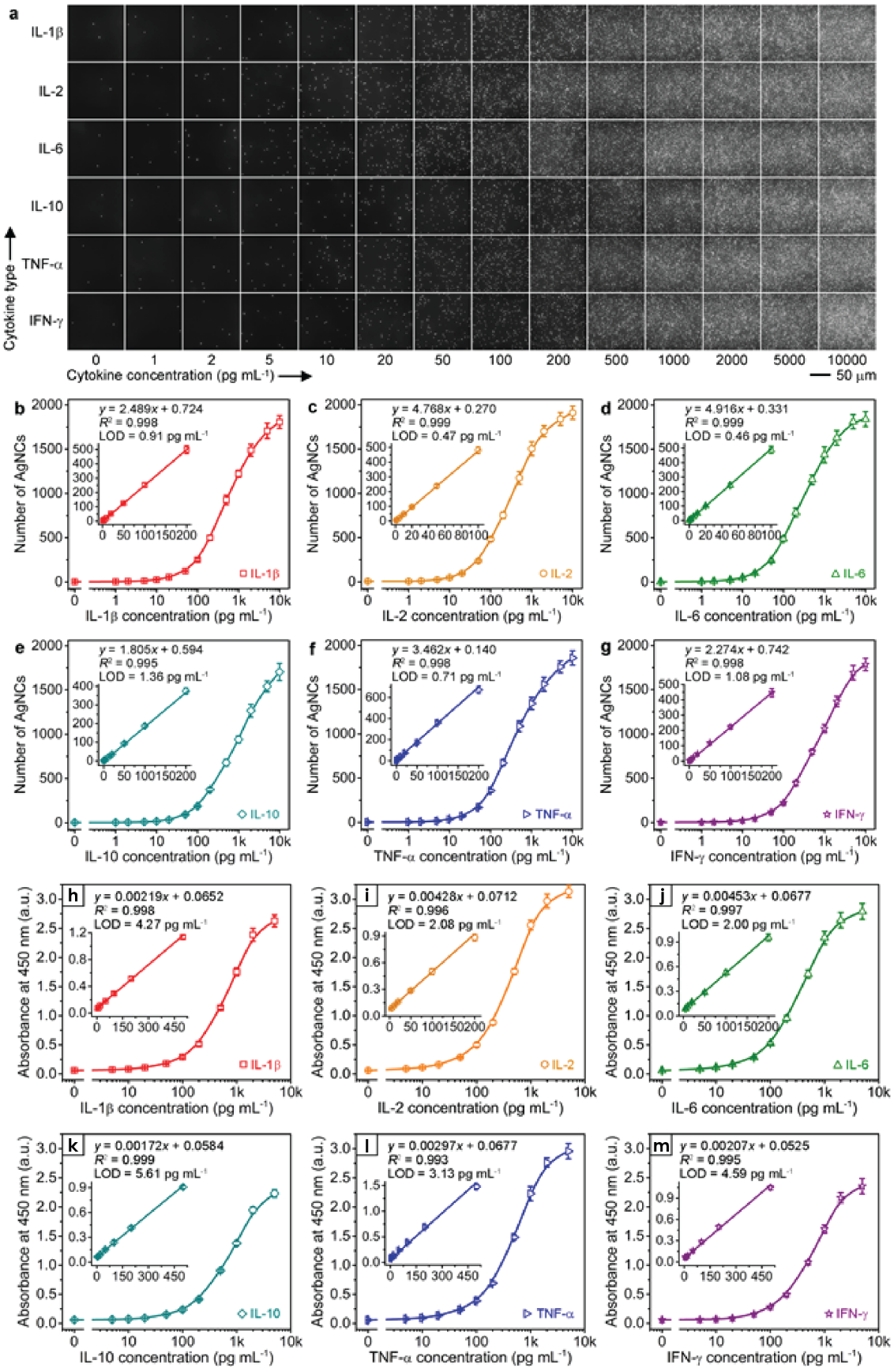
a
IL-1β
IL-2
IL-6
IL-10
TNF-α
IFN-γ
Cytokine type
0 1 2 5 10 20 50 100 200 500 1000 2000 5000 10000
Cytokine concentration (pg mL⁻¹)
50 μm
b
y = 2.489x + 0.724
R² = 0.998
LOD = 0.91 pg mL⁻¹
Number of AgNCs
IL-1β concentration (pg mL⁻¹)
IL-1β
c
y = 4.768x + 0.270
R² = 0.999
LOD = 0.47 pg mL⁻¹
IL-2 concentration (pg mL⁻¹)
IL-2
d
y = 4.916x + 0.331
R² = 0.999
LOD = 0.46 pg mL⁻¹
IL-6 concentration (pg mL⁻¹)
IL-6
e
y = 1.805x + 0.594
R² = 0.995
LOD = 1.36 pg mL⁻¹
IL-10 concentration (pg mL⁻¹)
IL-10
f
y = 3.462x + 0.140
R² = 0.998
LOD = 0.71 pg mL⁻¹
TNF-α concentration (pg mL⁻¹)
TNF-α
g
y = 2.274x + 0.742
R² = 0.998
LOD = 1.08 pg mL⁻¹
IFN-γ concentration (pg mL⁻¹)
IFN-γ
h
y = 0.00219x + 0.0652
R² = 0.998
LOD = 4.27 pg mL⁻¹
Absorbance at 450 nm (a.u.)
IL-1β concentration (pg mL⁻¹)
IL-1β
i
y = 0.00428x + 0.0712
R² = 0.996
LOD = 2.08 pg mL⁻¹
IL-2 concentration (pg mL⁻¹)
IL-2
j
y = 0.00453x + 0.0677
R² = 0.997
LOD = 2.00 pg mL⁻¹
IL-6 concentration (pg mL⁻¹)
IL-6
k
y = 0.00172x + 0.0584
R² = 0.999
LOD = 5.61 pg mL⁻¹
IL-10 concentration (pg mL⁻¹)
IL-10
l
y = 0.00297x + 0.0677
R² = 0.993
LOD = 3.13 pg mL⁻¹
TNF-α concentration (pg mL⁻¹)
TNF-α
m
y = 0.00207x + 0.0525
R² = 0.995
LOD = 4.59 pg mL⁻¹
IFN-γ concentration (pg mL⁻¹)
IFN-γ

Figure 4.8 Detection of multi-cytokine standards using the machine-learning-assisted microfluidic nanoplasmonic digital immunoassay and ELISA. (a) Dark-field images of antibody microarrays taken from the detection of multi-cytokine standards containing IL-1β, IL-2, IL-6, IL-10, TNF-α, and IFN-γ with various concentrations in the range of 0-10,000 pg mL^{-1}. (b-g) Calibration curves of IL-1β (b), IL-2 (c), IL-6 (d), IL-10 (e), TNF-α (f), and IFN-γ (g) generated by plotting the particle number of AgNCs against corresponding cytokine concentration. Insets show the corresponding linear regions of the calibration curves. Note that six images (six replicated sensing areas in one channel) were used for each concentration of each cytokine to establish the calibration curves. Calibration curves of (h) IL-1β, (i) IL-2, (j) IL-6, (k) IL-10, (l) TNF-α, and (m) IFN-γ obtained from the detection of cytokine standards using commercial cytokine ELISA kits (Fisher Scientific, Inc.). Insets show the corresponding linear regions of the calibration curves.

The LODs for the six cytokines were determined to be 0.91 pg mL^{-1} (IL-1β), 0.47 pg mL^{-1} (IL-2), 0.46 pg mL^{-1} (IL-6), 1.36 pg mL^{-1} (IL-10), 0.71 pg mL^{-1} (TNF-α), and 1.08 pg mL^{-1} (IFN-γ) based on the 3σ/kslope, where σ and kslope are the standard deviation of background signal acquired from a blank control (n = 6) and the regression slope of each linear curve, respectively. The determined sensing dynamic ranges for the target cytokines by our multiplex immunoassay are one order magnitude wider than the standard single-plex cytokine ELISA method (dynamic ranges: 5-5,000 pg mL^{-1} for all six cyokines, **Figure 4.8h-m**). The achieved LODs down to sub-pg mL^{-1} represent the highest class of sensitivity in nanoplasmonic biosensors for multiplex cytokine detection without signal amplification. Since the serum cytokine concentrations in COVID-19 severe patients span across the dynamic ranges of 1-10,000 pg mL^{-1} including 0.5-130 pg mL^{-1} for IL-1β, 1-18 pg mL^{-1} for IL-2, 1-10,000 pg mL^{-1} for IL-6, 1-20 pg mL^{-1} for IL-10, 1-1,000 pg mL^{-}

[1] for TNF-α, and 4-80 pg mL^{-1} for IFN-γ our immunoassay provides a well suitable sensing dynamic range and LODs for profiling the serum cytokines in COVID-19 patients.[63, 122]

To highlight the advantages of our CNN method on digital counting in the immunoassay, we compared the sensing dynamic ranges and LODs of the immunoassay using the CNN method and the Image-Pro Plus method. **Figure 4.9** shows the calibration curves of the immunoassay for the six target cytokines obtained from the Image-Pro Plus method. The sensing dynamic ranges of the immunoassay using Image-Pro Plus method were determined to be 1-5,000 pg mL^{-1} for IL-1β, 1-1,000 pg mL^{-1} for IL-2, 1-2,000 pg mL^{-1} for IL-6, 1-5,000 pg mL^{-1} for IL-10, 1-2,000 pg mL^{-1} for TNF-α, and 1-5,000 pg mL^{-1} for IFN-γ, which were 2-10-fold narrower than those using the CNN method. The calculated LODs of the immunoassays by Image-Pro Plus method (1.01 pg mL^{-1} for IL-1β, 0.51 pg mL^{-1} for IL-2, 0.50 pg mL^{-1} for IL-6, 1.44 pg mL^{-1} for IL-10, 0.83 pg mL^{-1} for TNF-α, and 1.16 pg mL^{-1} for IFN-γ) were also compromised as the Image-Pro Plus method cannot provide accurate counting on the aggregated/neighboring and dim spots, leading to the underestimation and miscounting of the AgNCs, especially at high AgNC counts. These results further demonstrate the advantages of our CNN method in accurate and robust digital counting that enhances the analytical performance of the nanoplasmonic digital immunoassay.

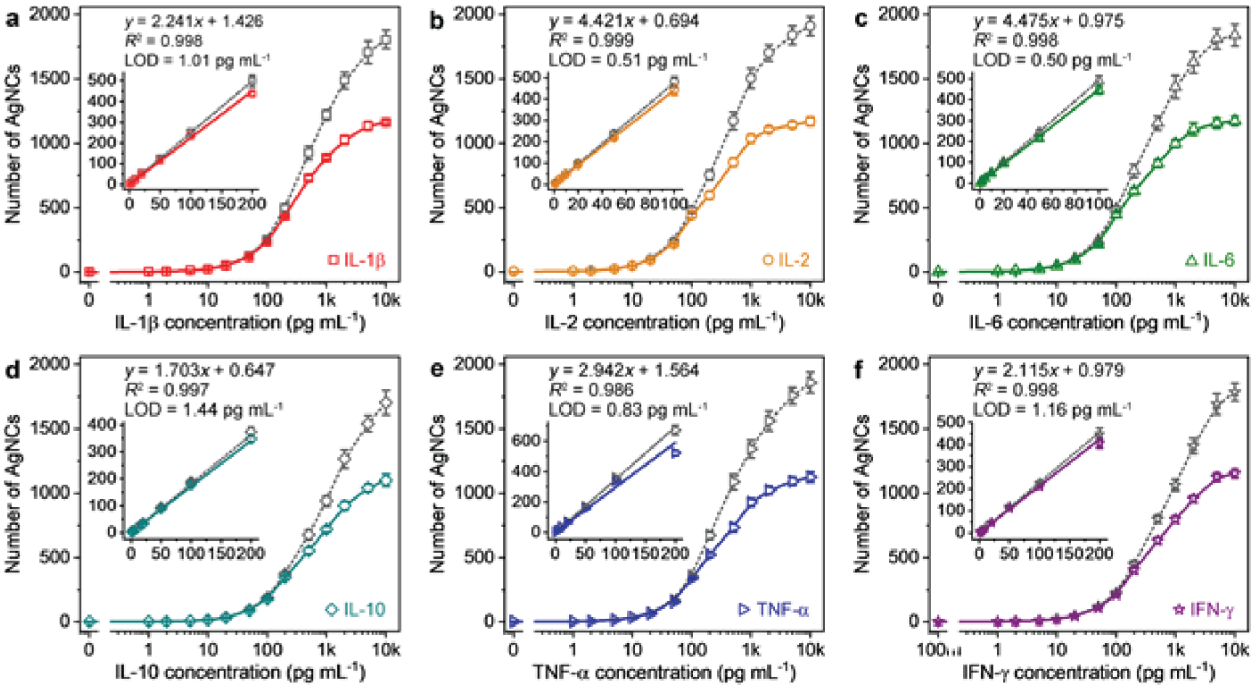

Figure 4.9 Comparison of calibrations curves calculated by Image-Pro Plus (solid curves) and CNN method (dashed curves). Insets show the corresponding linear regions for the calibration curves.

The reproducibility of our digital immunoassay was studied by replicate determinations on three different multi-cytokine standards with low, medium, and high concentrations (10, 100, and 1,000 pg mL^{-1}) using the same- and different-batches of multi-antibody microarray chips and AgNC-DAb conjugates. The evaluation was based on the calculation of intra- and inter-batch coefficients of variation (CVs, n = 6). Experimental results show that the intra- and inter-batch CVs using the same- and different-batches of the chips and conjugates were in the ranges of 3.27-8.87% and 5.14-10.8%, respectively, for all six cytokines at 10, 100, and 1,000 pg mL^{-1}. The low CVs suggest excellent reproducibility and repeatability of the nanoplasmonic digital immunoassay for large-scale production towards clinical usage.

From a clinical perspective, another key issue for practical application of a multiplex cytokine immunoassay is the specificity and cross-reactivity, considering that human serum is an inherently complex, multi-component mixture. To evaluate the specificity and cross-reactivity of our multiplex cytokine immunoassay, we conducted three control tests as follows: (*i*) a negative human serum sample without target cytokines (i.e., heat-inactivated and sterile-filtered human serum); (*ii*) positive serum samples containing only single analyte (negative human serum spiked with IL-1β, IL-2, IL-6, IL-10, TNF-α, or IFN-γ at a concentration of 100 pg mL^{-1}); and (*iii*) positive serum samples containing all the six target cytokines (negative human serum spiked with all the six cytokines at a concentration of 100 pg mL^{-1}). In all three control tests, only with the presence of target cytokines in the serum samples can we observe a noticeable number of AgNCs on the corresponding microarrays (**Figure 4.10a, b**). The measured particle numbers of AgNCs were further converted to analyte concentrations according to the calibration curves in **Figure 4.8**. As seen in **Figure 4.10c**, the back-calculated cytokine concentrations correlated very well with their corresponding values (100 pg mL^{-1}), showing negligible cross-reactivity of the nanoplasmonic immunoassay for multiplex detection of six cytokines. The minimal cross-reactivity and background noise further confirm that other bio-components coexisting in the human serum did not interfere with the immune sandwich formation, suggesting high specificity of the multiplex immunoassay for target cytokine determination.

It should be emphasized that such excellent analytical performance is attributed to the seamlessly integration of the microfluidic immunoassay platform, the nanoplasmonic digital imaging technology, and the machine-learning-based image processing method. The synergistic combination of the three techniques into an integrated biosensor allows highly sensitive, accurate

cytokine profiling in a high-throughput, multiplex manner, showing significant advantages over many existing cytokine biosensing techniques developed toward clinical applications.[61]

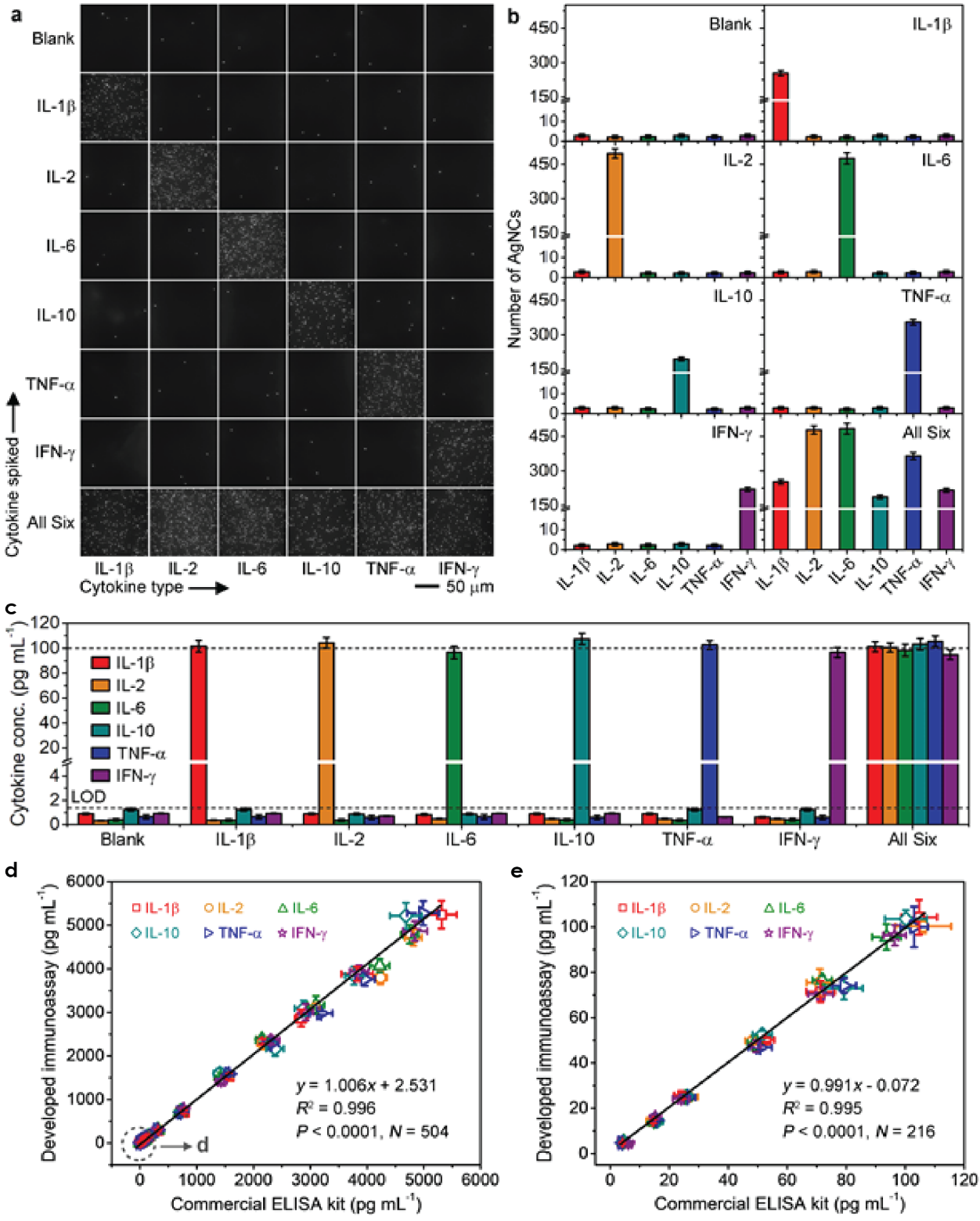

Figure 4.10 Detection of multi-cytokines spiked in negative human serum matrix using the machine-learning-assisted microfluidic nanoplasmonic digital immunoassay. (a) Dark-field images of antibody microarrays taken from the detection of human serum matrix spiked with different mixtures of cytokines. The concentration of each cytokine spiked in the human serum matrix is 100 pg mL^{-1}. (b) Bar graph showing the intensity of the detection signal (i.e., particle number of AgNCs) obtained from (a). (c) Bar graph showing cytokine concentrations quantified for the samples in (a-b). The upper and lower dashed line represents the predetermined value of the analyte concentration (100 pg mL^{-1}) and LOD, respectively. (d,e) Correlation analysis between the developed machine-learning-assisted microfluidic nanoplasmonic digital immunoassay and commercial ELISA kit in quantifying cytokines from human serum matrix spiked with different concentrations of cytokines in the ranges of 5-5,000 pg mL^{-1} (d) and 5-100 pg mL^{-1} (e).

4.3.5 Analysis of human serum samples and method validation

Wide acceptance of an immunoassay requires its full validation in real sample detection scenarios. To demonstrate the potential practical application of our immunoassay in clinical diagnosis, we utilized our immunoassay to analyze 16 cytokine-spiked human serum samples and validated the results with the existing gold-standard method, i.e., ELISA. These human serum samples were prepared by spiking negative human serum samples with a mixture of all the six cytokines at 16 different concentrations ranging across the entire dynamic range of our immunoassay. Cytokines in each sample were quantified based on the calibration curves shown in **Figure 4.8**, and the obtained results were compared with references measured by commercially available cytokine ELISA kits. The comparison was performed using linear regression analysis between the two methods (**Figure 4.10d, e**). A strong positive correlation ($R^2 = 0.996$) was found between the measured cytokine concentrations by the developed immunoassay and the reference

ELISA with a slope of 1.006 and an intercept of 2.531. (**Figure 4.10d**). It is worth mentioning that in a lower cytokine concentration range (5-100 pg mL^{-1}), the measured cytokine concentrations by the developed immunoassay still showed excellent agreement with those by ELISA (Slope = 0.991, Intercept = -0.072, and R^2 = 0.995; **Figure 4.10e**). These results further demonstrated the high accuracy and reliability of our immunoassay in analyzing complex human serum samples even at low cytokine concentrations, implying its great potential in cytokine storm profiling in COVID-19 patients.

4.3.6 Application in serum cytokine profiles and cytokine storm monitoring for COVID-19 patients

Finally, we applied the developed immunoassay for measuring serum cytokines in COVID-19 patients and utilized the cytokine profiles to assist the screening of high-risk patients with cytokine storms. To demonstrate the clinical usage of the nanoplasmonic digital immunoassay, we conducted simultaneous detection of 40 human serum specimens of COVID-19 severe patients collected from the University of Michigan Hospital (Patients or their authorized representatives provided informed consent for the use of biospecimens, as approved by the Institutional Review Board of the University of Michigan (HUM000179668).). These COVID-19 patients were determined to be critically ill as they were experiencing respiratory failure symptom and receiving hospitalization in the intensive care unit (ICU) for either mechanical ventilation or extracorporeal membrane oxygenation (ECMO). Within only 5 hours, we completed six replicate detections of the six target cytokines in the 40 human serum specimens by performing a total of 1440 tests on 5 microfluidic immunochips. The detection results obtained from the 1440 tests were showed in **Figure 4.11a**, manifesting the simplicity, speed, high multiplex, and high throughput features of our immunoassay in performing such massively parallel testing. The concentrations of the six

cytokines in these COVID-19 patient serum samples were calculated by averaging the detection results of the six replicate tests, and their serum cytokine profiles were summarized in **Figure 4.11b** accordingly. The serum cytokine profiles for the COVID-19 patients show a highly diverse range from 0.57-5,497.25 pg mL^{-1} with a few abnormally elevated cytokine secretions. Specifically, the serum samples No. 1-25 were collected from the COVID-19 patients without any treatments, showing serum cytokine concentrations of 1.32-42.23 pg mL^{-1} for IL-1β, 0.57-514.27 pg mL^{-1} for IL-2, 10.71-1,732.71 pg mL^{-1} for IL-6, 1.43-11.95 pg mL^{-1} for IL-10, 1.11-48.92 pg mL^{-1} for TNF-α, and 1.73-16.60 pg mL^{-1} for IFN-γ. According to the previously reported average cytokine levels in healthy donors (IL-1β: ~0.4 pg mL^{-1}, IL-2: ~1.1 pg mL^{-1}, IL-6: ~1.7 pg mL^{-1}, IL-10: ~1.7 pg mL^{-1}, TNF-α: ~7.4 pg mL^{-1}, and IFN-γ: ~0.5 pg mL^{-1}), we observed that all the 25 serum samples from the COVID-19 severe patients contained abnormally high levels of IL-6, while 52%, 60%, 64%, 52%, and 80% of the patients showed elevated secretion of IL-1β, IL-2, IL-10, TNF-α, and IFN-γ, respectively.[63, 122] The observed elevated expressions of pro-inflammatory cytokines (e.g., IL-6, IL-1β, IL-2, TNF-α, and IFN-γ) and anti-inflammatory cytokines (e.g., IL-10) in these COVID-19 patients were broadly consistent with recent studies.[63, 122, 124, 169-170] The elevated serum cytokine levels indicate that the majority of these COVID-19 patients were likely experiencing cytokine storms, who would be at high risk for developing acute respiratory distress and require guided therapies to alleviate this inflammatory state and improve prognosis. [63, 122, 124, 169-170] The serum samples No. 26-35 and No. 36-40 were collected from the COVID-19 patients with treatments of tocilizumab and selective cytopheretic device, respectively. Significantly higher cytokine expressions (e.g., IL-6 (206.60-5,497.25 pg mL^{-1})) were observed especially in patients right after receiving the immunomodulatory treatment of tocilizumab (Samples No. 26-35). The elevated serum IL-6 could be mainly attributed to the initial binding of

tocilizumab to IL-6 receptor that inhibits the receptor mediated clearance, suggesting the importance of dynamic observation of cytokine profiles in understanding the patient response to the immunomodulatory treatment.[171-172] The measured diverse serum cytokine profiles (from sub-pg mL^{-1} to several-ng mL^{-1}) in different patients further demonstrate the high sensitivity, accuracy, multiplexity, and wide dynamic range of our immunoassay in complicated serum cytokine analysis. Such an enabling technology would allow precise and timely monitoring of inflammatory response to reveal the cytokine storm features and immune status in COVID-19 patients, which could facilitate the therapeutic stratification and guide clinicians to treat COVID-19 patients more effectively.

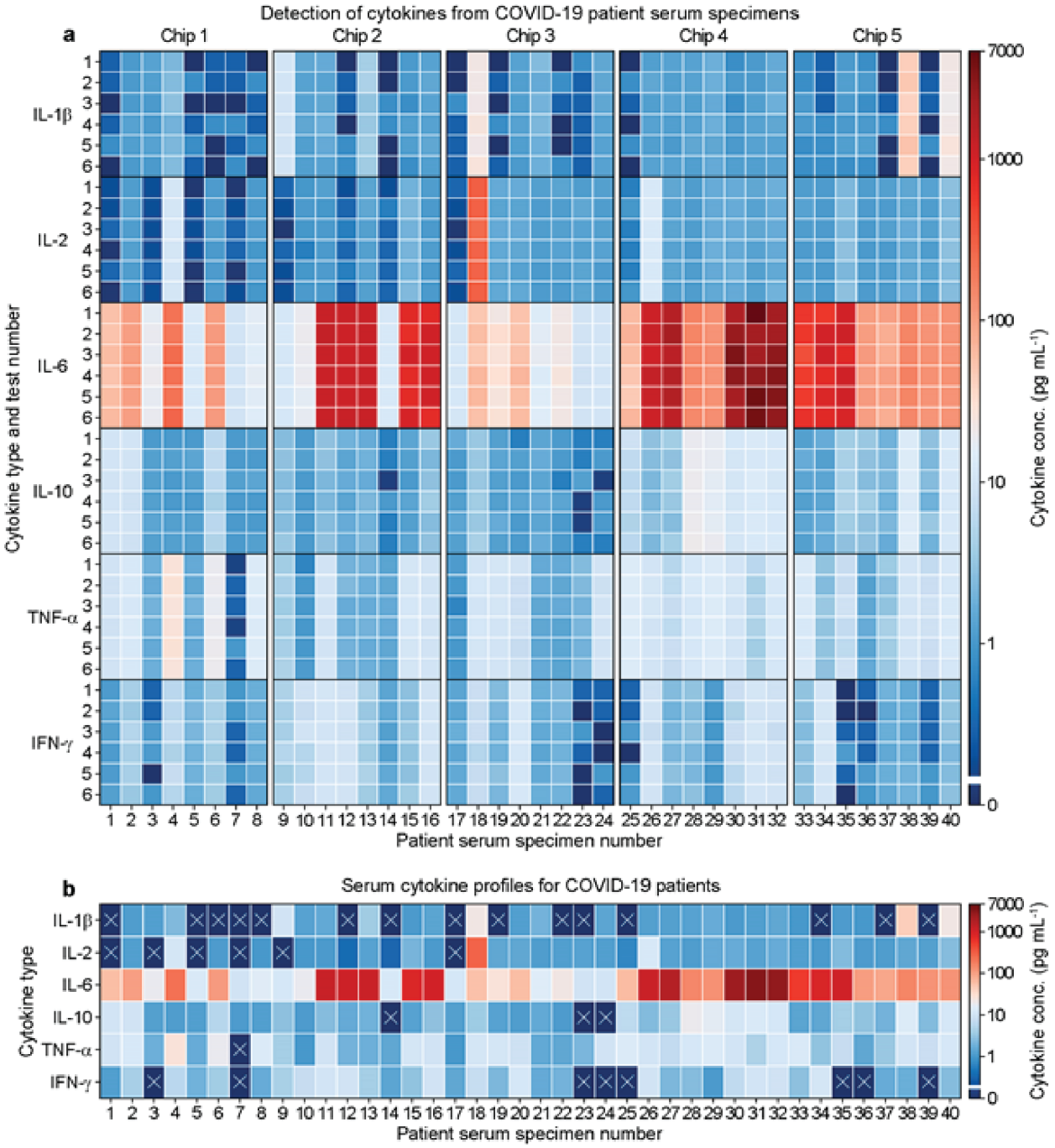

Figure 4.11 Application of the machine-learning-assisted microfluidic nanoplasmonic digital immunoassay for profiling the serum cytokines from COVID-19 patients. (a) Heatmap showing the detection results of cytokines from 40 COVID-19 patient serum samples. Each of the six cytokines in the specimens was detected simultaneously in six repeats with a total of 1440 tests

over 5 microfluidic immunochips. (b) Heatmap showing the summary of the serum cytokine profiles obtained from 40 COVID-19 patient serum specimens. The cytokine levels were based on the average value of six replicate tests. Scales indicate the value of cytokine concentration. Symbol "×" as "not applicable" represents that the cytokine concentration is lower than the LOD of our immunoassay.

4.4 Conclusion

In conclusion, we have demonstrated a high-performance machine-learning-assisted microfluidic nanoplasmonic digital immunoassay that enables high-throughput detection of multiple immune biomarkers in a rapid, sensitive, selective, accurate, and easy-to-implement manner. The key to the success of our strategy can be primarily ascribed to the systematic combination of the high-throughput and multiplex microfluidic immunoassay platform, ultrasensitive nanoplasmonic digital imaging technology, and rapid and accurate machine-learning-based image processing method. Owing to the synergistic effects of the advantages of these technologies, our one-step immunoassay allows simultaneous detection of six cytokines in sextuplicate of 8 different samples (3 μL each) per chip, with a record high detection limit of sub-pg mL^{-1}, a wide linear dynamic range of 4 orders of magnitude and a total assay time under 100 min. The clinical application of such a high-performance immunoassay has been successfully demonstrated in the analysis of cytokine profiles using serum samples from COVID-19 patients, showing high accuracy and reliability in comparison to the commercial gold-standard ELISA. To the best of our knowledge, our study is the first to demonstrate a multiplex nanoplasmonic digital detection strategy that can meet the various stringent requirements for monitoring cytokine profiles in COVID-19 patients. We believe the presented immunoassay is a promising approach to allow continuous characterization of cytokine storms and thus provide timely and reliable information to optimize care for COVID-19 patients. The developed immunoassay can be readily expanded to a highly multiplex (>20) cytokine detection platform for comprehensive immune status analysis of patients in a clinical setting. Through integration with hand-held imaging systems and/or paper testing strips, the nanoplasmonic digital immunoassay can be further exploited as a point-of-care

(POC) detection platform for cytokines and provide clinical significance in disease early diagnosis, management, and prevention.

Chapter 5

Probing the Aggregation and Immune Response of Human Islet Amyloid Polypeptides with Ligand-Stabilized Gold Nanoparticles

5.1 Introduction

Human islet amyloid polypeptide (IAPP) is a 37-residue peptide co-synthesized and co-secreted with insulin by pancreatic β-cell islets.[173-174] In addition to its functional role in glycemic control, IAPP is closely associated with β-cell degeneration in type 2 diabetes (T2D), a metabolic disease and a global epidemic.[175] The aggregation of IAPP involves the transformation of functional IAPP monomers to oligomers, protofibrils and amyloid fibrils. While IAPP monomers are disordered in nature, IAPP oligomers, protofibrils and fibrils are increasingly hydrophobic and rich in beta-sheets.[175] Biologically, IAPP in the oligomeric form is believed to be the most toxic, while IAPP amyloids and plaques have been found in the islets of 90% T2D patients suggesting a causative process.[176-178] Overall, understanding the aggregation of IAPP, in a test tube or in the physiological environment, is of crucial importance for basic research on protein misfolding and for delineating the pathogenesis of T2D.

The kinetics of protein aggregation is often inferred from a thioflavin T (ThT) or a Congo red fluorescence assay, to report on the three stages of protein nucleation, elongation, and saturation on pathway to the amyloid state. Direct observation of the aggregation states of amyloid proteins, in contrast, can be performed ex situ using atomic force microscopy, electron microscopy, nuclear magnetic resonance or X-ray spectroscopies.[179-180] In addition, monoclonal antibodies, such as solanezumab, have been utilized for immunochemical detection of amyloid aggregation, as in the Eli Lilly phase-3 clinical trial against Alzheimer's.[181-183] Antibodies such as aducanumab can bind and clear amyloid plaques, but are selective against the conformation epitopes rather than the sequences of fibrils.[184-187] Overall, these methods, with the exception of the kinetic assays, require labor- and cost-intensive experimentation and data collection.

Recently, we have developed a biomimetic system of coating gold nanoparticles (AuNPs) with the amyloid fragments of whey protein beta lactoglobulin (bLg).[188] The resulting functional bLg-AuNPs intercalated with IAPP through beta-sheet stacking. This scheme, though effective in mitigating IAPP toxicity, did not have the capacity of discerning the three major aggregation states, i.e., monomeric, oligomeric/protofibrillar and fibrillar forms of amyloid proteins (**Figure 5.1**). Hyperspectral imaging (HSI) integrates high signal-to-noise dark field microscopy with high-resolution scattering spectra for each pixel, and has been employed for food quality control and detection of the aggregation, cellular uptake and interaction of nanoparticles with proteins.[189-194] In this study, we first employed HSI to probe the three major aggregation states of IAPP via their interactions with ligand-stabilized AuNPs (**Figure 5.1**) that possessed the hydrodynamic size of 22.7 to 35.1 nm and subsequently induced spectral shifts. Then, the responses of Jurkat human T cells to the three IAPP aggregation states as well as their associations with the AuNPs were examined, taking advantage of the high sensitivity of a localized surface plasmon resonance (LSPR)

immunoassay for real-time, multiplex cytokine detection. These physical and biological characterizations facilitate the study of protein aggregation and therapeutic applications of nanomaterials against the toxicity of amyloid proteins.

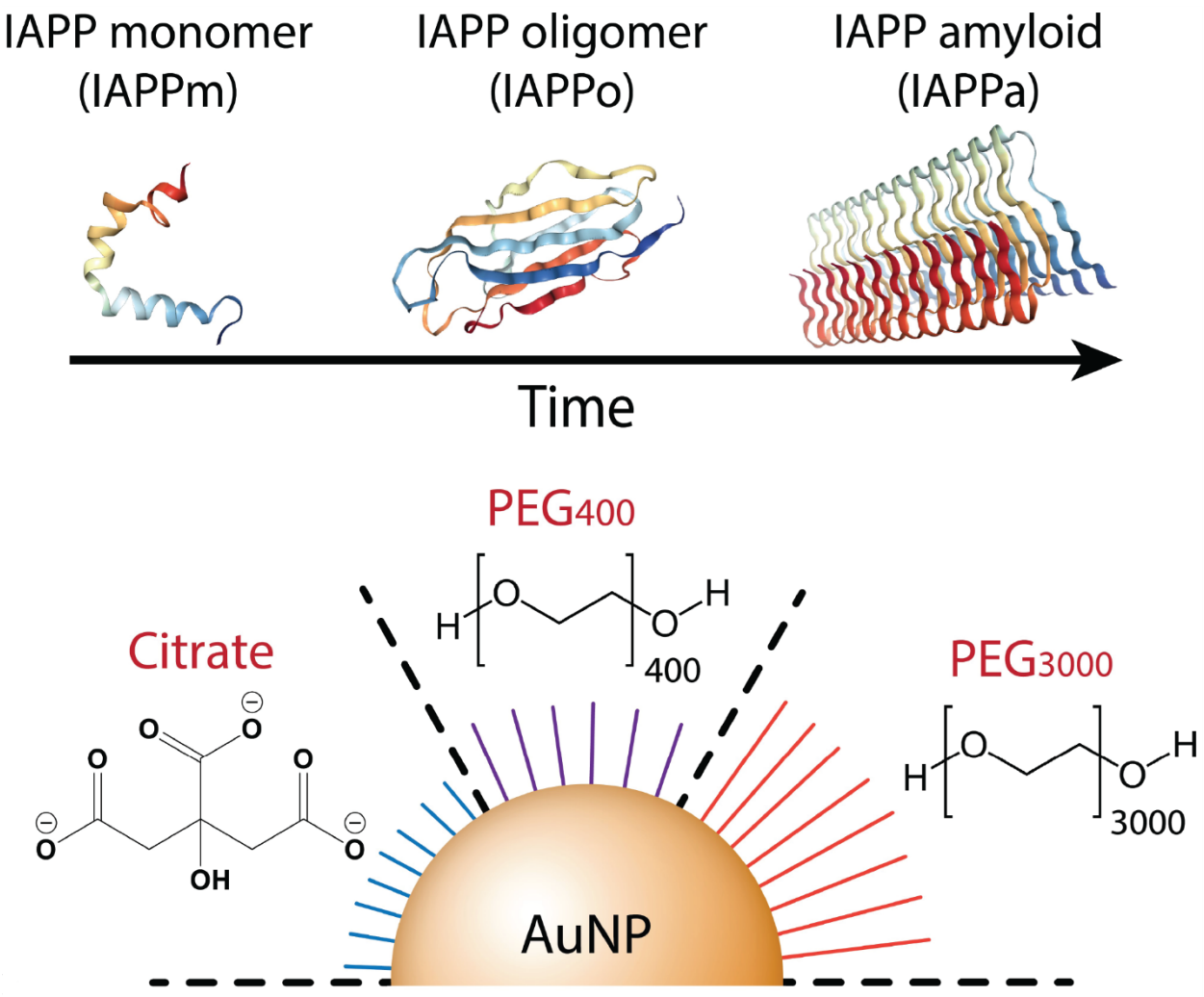

Figure 5.1 Design of the study, where monomeric, oligomeric/protofibrillar and fibrillar IAPP were brought into contact with AuNPs coated with citrate, PEG_{400} and PEG_{3000}.

5.2 Materials and Methods

5.2.1 Synthesis of ligand-stabilized AuNPs

Citrate AuNPs (Cit AuNPs) were synthesized by the direct reduction method.[195] Briefly, 10 mL of 1 mM aqueous solution of $HAuCl_4$ was refluxed at 120 °C and 1 mL of 40 mM trisodium citrate was added into the Au solution. The color of the suspension changed to wine red, indicating the formation of 15-20 nm AuNPs. The PEG-stabilized AuNPs were synthesized by ligand replacement.[196] Specifically, 1 mL of Cit AuNPs were mixed with 10 μL of 10% SH-PEG-COOH solution of molecular weight 400 or 3000 Da. The suspension was kept on stirring overnight. All AuNPs were purified via centrifugal filtration of 100 kDa MWCO. The concentration of AuNPs was calculated by a reported method.[195, 197] The absorbance of the AuNP suspensions was measured with a UV-Vis spectrophotometer (PerkinElmer, Enspire).

5.2.2 Preparations of three IAPP aggregation states

Human islet amyloid polypeptide, IAPP (37 residue, H - Lys - Cys - Asn - Thr - Ala - Thr - Cys - Ala - Thr - Gln - Arg - Leu - Ala - Asn - Phe - Leu - Val - His - Ser - Ser - Asn - Asn - Phe - Gly - Ala - Ile - Leu - Ser - Ser - Thr - Asn - Val - Gly - Ser - Asn - Thr - Tyr – OH, AnaSpec, Inc.) was treated with hexafluoro-2-propanol (HFIP) before use. The HFIP-treated IAPP assumed the monomeric form. Oligomeric IAPP was prepared by incubating the HFIP-treated IAPP at 4 °C for 5 h, while full length mature fibrils of IAPP were prepared by incubation the peptide over 24 h at room temperature. All three fibrillation states were confirmed by transmission electron microscopy (TEM).

5.2.3 Transmission electron microscopy characterization

TEM images were recorded on a Tecnai F20 transmission electron microscope (FEI) at 200 kV with an UltraScan 1000 (2k × 2k) CCD camera (Gatan). Formvar coated copper mesh grid was glow-discharged and a drop of sample was blotted on the grid for 60 s. Negative staining with 1% uranyl acetate was applied to improve image contrast.

5.2.4 Hyperspectral imaging characterization

HSI imaging was performed on a dark-field hyperspectral microscope (CytoViva, USA) fixed with a PixelFly CCD camera (Cooke/PCO, USA/Germany). Images were recorded with 1 s exposure time and analyzed by ENVI 4.8 software. All images were normalized for blank background spectra. SPR spectra for AuNPs were recorded for 10-15 AuNPs across 5 images and averaged together. To study the interactions of AuNPs with different IAPP species, AuNPs (5 μM) were incubated for 5 min with the IAPP species (25 μM), and a drop of sample was sandwiched between a glass slide and a coverslip and sealed with slide sealant.

5.2.5 Thioflavin T kinetic assay

A ThT assay was performed by incubating 100 μL aqueous solution of IAPP (25 μM), ThT (75 μM), and AuNPs (1.25-10 μM) in 96 well micro-plates at 37 °C. ThT fluorescence readings were recorded with light excitation at 440 nm and emission at 485 nm over a period of 6 h after specified intervals (PerkinElmer, Enspire).

5.2.6 Circular dichroism (CD) spectroscopy

CD spectroscopy analysis was performed by mixing the three aggregation states of IAPP, as prepared for TEM, with the three different types of AuNPs. The final concentrations of the IAPP and the AuNPs in the samples were adjusted to 100 and 50 μM. The incubation time was 10 min before the CD reading. 200 μL of the samples were pipetted into a CD cuvette and CD spectra

were recorded from 190 to 240 nm with 1 nm step size at room temperature. The data was analyzed by Dichroweb (Contin/Reference set 4) for estimation of the percentage secondary content.[198]

5.2.7 Finite element analysis simulation

The scattering spectra of Cit AuNPs and the three types of IAPP-Cit AuNPs complexes were simulated by the finite element method using commercial multi-physics simulation software (COMSOL). Briefly, four simulation models of single Cit AuNPs, IAPPm-Cit AuNPs, IAPPo-Cit AuNPs, and IAPPa-Cit AuNPs were constructed. The far-field domain was set as a semi-spherical shell with a radius of half the wavelength of incident light. A perfectly matched layer, serving as the boundary condition of light and with the radius of a half incident light wavelength, was then defined on top of the far-field domain. A polarized incident light was set in parallel with the Cit AuNP packing direction. The scattering intensity was evaluated by the scattering cross-section C_{SCS} of AuNP, which is the integration of the scattering wave intensity over the surface of far-domain Ω,

$$C_{SCS} = \int \frac{I_{AuNP}}{I_{background}} d\Omega, \quad (3)$$

where I_AuNP is the scattering intensity from the AuNPs and I_background the background signal without the presence of AuNPs. To simplify computation, Cit AuNPs were treated as single nanospheres with a radius of 11.3 nm. IAPP oligomers/profibrils and amyloids were simplified as cylinders with radii of 2 and 5 nm, respectively. The frequency-dependent dielectric constant of gold, ϵ_1, was derived from the Lorentz-Drude model,

$$\epsilon_1 = 1 - \frac{\omega_p^2}{\omega^2+\gamma^2}, \quad (4)$$

where ω_p is the bulk metal plasmon frequency and γ is the bulk metal damping frequency.[199] The relative permittivity of water and IAPP was fixed as 1.77 and 2.25, respectively.[6] Due to the

relatively small dimensions of IAPP monomers, the IAPPm-Cit AuNPs model was constructed as pure Cit AuNP aggregates, consisting of 12 Cit AuNPs, while Cit AuNPs were assumed to be adsorbed on the fibrils in IAPPa-Cit AuNPs and IAPPo-Cit AuNPs models. The distances between neighboring AuNPs of the IAPPa-Cit AuNPs, IAPPo-Cit AuNPs, and IAPPm-Cit AuNPs models

5.2.8 LSPR assay protocol

Jurkat human T cells (CRL-2901TM, ATCC) were cultured in RPMI-1640 with 200 mcg/mL G428 and 10% fetal bovine serum. The cells were incubated at 37 °C with 5% CO_2 in a Cell Culture Incubator (Thermo Scientific). The culture medium was replaced two to three times per week to maintain the suitable concentration of 1×10^5 to 1×10^6 cells/mL. The cells were collected through centrifugation at 125 g for 5 min with subsequent resuspension in a fresh culture medium.

For the IAPP control experiments, freshly prepared IAPP was diluted in 1× PBS to 50 μM. One μL IAPPm solution was immediately added to 1 mL culture medium with T cells at 1×10^6 cells/mL and incubated for 2 h. The remaining IAPPm solutions were incubated at 4 °C for 5 h (IAPPo) and 24 h (IAPPa). After that, 10 μL supernatant was collected from the T-cell culture medium for the LSPR immunoassay. The same procedure was repeated for IAPPo and IAPPa stimulated T cells. For the AuNP-IAPP corona experiments, 9 types of IAPP-AuNP complexes were prepared by mixing 100 μM IAPP solution with 1 mM AuNP solution at a 1:1 molar ratio and incubated for 5 min. The same steps were conducted to activate the T cells and perform the LSPR immunoassay.

5.2.9 Toxicities of ligand-stabilized AuNPs and IAPP aggregates

Pancreatic βTC-6 (ATCC) beta cells were growth in complete Dulbecco's modified Eagle’s medium (DMEM) with 15% fetal bovine serum (FBS). To perform the viability experiment, 96

well plate (Costar black/clear bottom) was coated with 70 μL Poly-L-lysine (Sigma, 0.01%) for 30 min at 37 °C. The wells were washed 3 times with phosphate buffered saline, and ~60,000 cells in 200 μL DMEM with 15% FBS were added to each well. The cells were incubated for 2 days at 37 °C and 5% CO_2 to reach ~80% confluency. The cell culture medium was then refreshed, and 1 μM propidium iodide (PI) dye in complete DMEM was added to the wells and incubated for 30 min. For the treatment, 20 μM IAPP (0 h as monomers and 1 h aged as oligomers), 20 μM of Cit AuNPs, PEG_{400} AuNPs and PEG_{3000} AuNPs and IAPP pre-incubated with the AuNPs were added into the wells. After 14 h of treatment, samples were measured by Operetta (PerkinElmer, 20× PlanApo microscope objective, numerical aperture NA=0.7) in a live cell chamber (37 ºC, 5% CO_2). The percentage of dead cells (PI-positive) relative to total cell count was determined by a built-in bright-field mapping function of Harmony High-Content Imaging and Analysis software (PerkinElmer). The measurement was conducted at 5 reads per well and all were performed in triplicate. Untreated cells were recorded as controls.

5.3 Results and Discussion

5.3.1 Synthesis of ligand-stabilized AuNPs

The AuNPs used in this study were stabilized by three types of hydrophilic ligands – citrate (molecular weight: 189) and linear polyethylene glycol (PEG) of 400 Da (PEG_{400}) and 3,000 Da (PEG_{3000}) in molecular weight. Citrate can stochastically adsorb and desorb from nanoparticles in suspension, providing hydration to the AuNPs as well as competitive binding between the ligand and IAPP.[200] PEG is a stealth polymer offering a steric separation of nanoparticles in aqueous and preventing their recognition by opsonins of the immune system for prolonged blood circulation.[201-203] Here PEG_{400} and PEG_{3000} rendered flexibility in modulating the aggregation of AuNPs as well as their interactions with IAPP. AuNPs, meanwhile, induced surface plasmon resonance (SPR) upon light excitation, which served as reporters of their immediate nano-environments, including that of adsorbed IAPP species.

5.3.2 Probing IAPP aggregation states and their physical interactions with AuNPs

The interactions of AuNPs with monomeric (abbreviated as IAPPm hereafter), oligomeric/protofibrillar (IAPPo) and fibrillar IAPP (IAPPa) imparted changes to the dielectric environment of the AuNPs and consequently induced SPR spectral shifts. The citrate- (Cit-), PEG_{400}- and PEG_{3000}-coated AuNPs possessed increasing hydrodynamic sizes of 22.7 to 35.1 nm and similar zeta potentials of -35.8 to -31.9 mV, indicating good suspensibility of all three types of nanoparticles (**Table 5.1**).

Table 5.1 Hydrodynamic size, polydispersity index (PDI) and zeta potential of the three types of AuNPs. Also tabulated are the SPR spectra shifts of the AuNPs when incubated with IAPP monomers (Δλm), oligomers/protofibrils (Δλo) and amyloid fibrils (Δλa).

Parameters	Cit AuNPs	PEG_{400} AuNPs	PEG_{3000} AuNPs
Size (nm)	22.7 ± 2.4	28.4 ± 1.9	35.1 ± 2.2
PDI	0.165	0.114	0.124
Zeta potential (mV)	-35.8 ± 2.8	-33.7 ± 2.6	-31.9 ± 3.1
$\Delta\lambda_m$ (nm)	122 ± 6	92 ± 7	76 ± 5
$\Delta\lambda_o$ (nm)	81 ± 5	53 ± 6	35 ± 4
$\Delta\lambda_a$ (nm)	22 ± 3	14 ± 4	9 ± 4

The Cit, PEG_{400} and PEG_{3000} AuNPs were monodispersed before interacting with IAPP and immediately aggregated into small clusters upon 5 min of incubation with cationic IAPP monomers, driven by electrostatic and hydrophobic interactions (for Cit) as well as hydrogen bonding (for Cit, PEG_{400} and PEG_{3000}). Clustering of the AuNPs by IAPP monomers into chain-like structures was revealed by transmission electron microscopy (TEM) (**Figure 5.2a**), which was accompanied by concomitant color changes in the AuNP suspensions from wine red to purple/light purple (**Figure 5.2e**).

IAPP oligomers/protofibrils and fibrils were prepared by incubating IAPP monomers at 4 °C for 5 h and at room temperature for 24 h, respectively. Incubating AuNPs with IAPP oligomers/thin protofibrils resulted in their association, although the AuNPs were less tightly packed than with IAPP monomers. No intercalation but surface adsorption was observed when incubating AuNPs with IAPP fibrils (**Figure 5.2a**). In addition, the toxicities of IAPPm and IAPPo in the presence and absence of the three types of AuNPs were examined and summarized in **Figure 5.3**, with a 14 h treatment of pancreatic βTC6 cells. As expected, IAPPm and IAPPo elicited significant toxicities to the cells, while their toxicities were alleviated by Cit, PEG_{400} and PEG_{3000} AuNPs by ~50-60%

for the monomers and 40-50% for the oligomers, respectively. No significant toxicity was observed with IAPPa, while the presence of the AuNPs showed no effects on the toxicity of the fibrils.

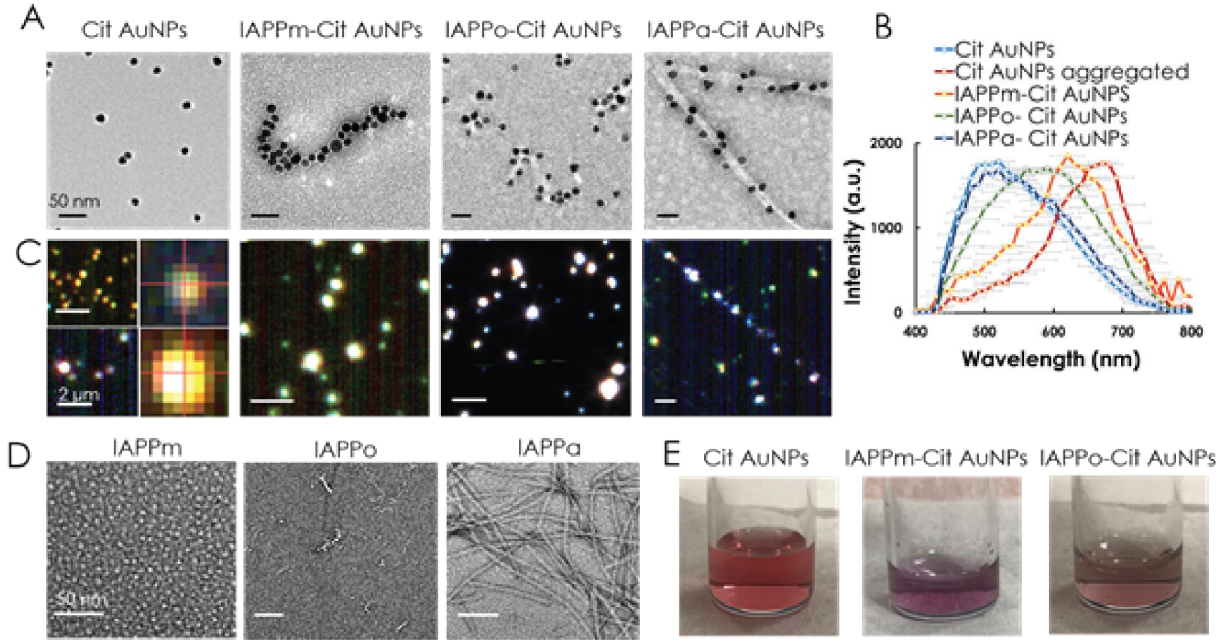

Figure 5.2 Characterization of Cit-AuNPs and Cit-AuNPs interacted with IAPP. Interactions of Cit AuNPs with IAPP monomers (IAPPm), oligomers/protofibrils (IAPPo) and amyloid fibrils (IAPPa), observed with TEM (A) and HSI (B&C). HSI analyses of pixels corresponding to single (up) and aggregated (down) Cit AuNPs are exemplified in the far-left panels of C. TEM of the three types of IAPP control species (D). Incubation of Cit AuNPs with IAPPm (middle) and IAPPo (right) induced color changes of the Cit AuNP suspension from wine red (left) to purple (middle) and light purple (right) (E). Incubation: 5 min. Scale bars in A&D: 50 nm. Scale bars in C: 2 µm.

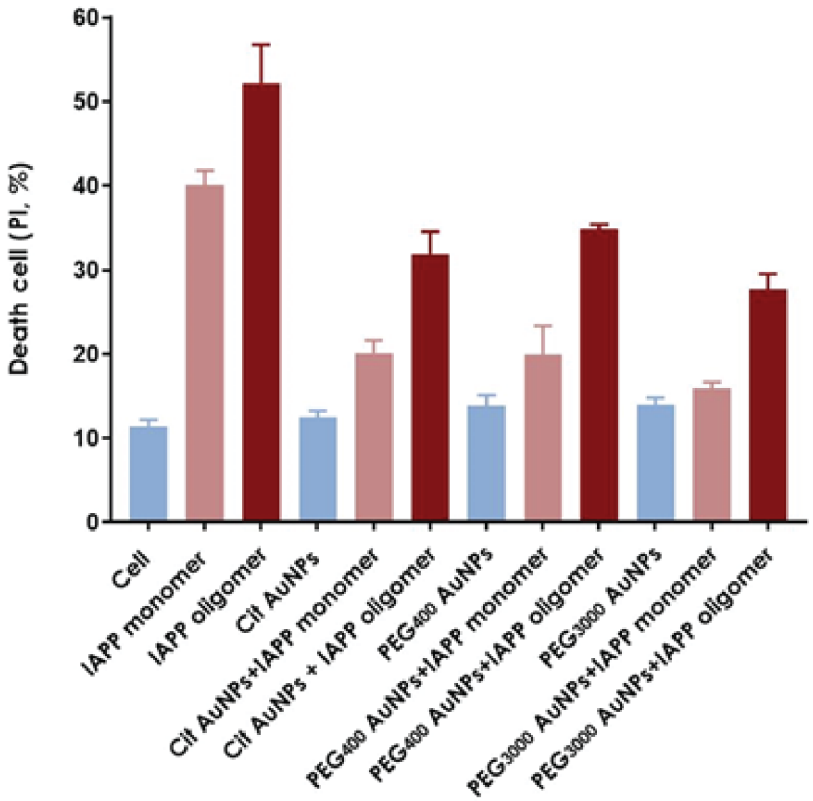

Figure 5.3 In vitro toxicities of IAPPm (0 h) and IAPPo (1 h) (20 μM) in βTC-6 cells in the presence and absence of 20 μM Cit AuNPs, PEG_{400} and PEG_{3000} AuNPs. The assay was carried out in triplicate. The error bars show the standard deviations of the averaged data sets.

Accordingly, HSI revealed the SPR spectral shifts of the AuNPs, following the order of $\Delta\lambda m > \Delta\lambda o > \Delta\lambda a$ for the nanoparticles incubated with IAPP monomers, oligomers/protofibrils and fibrils, respectively (**Figure 5.2b**, **Figure 5.4b**; **Table 1**). Furthermore, the most prominent SPR redshift upon binding with IAPP monomers was observed for Cit AuNPs, followed by that for PEG_{400} and PEG_{3000} AuNPs. The extents of the redshifts can be partially attributed to the different chain lengths/radii of gyration of the surface ligands, with Cit being the shortest and PEG_{3000} the longest. The stronger antifouling capacity of PEG_{3000} than PEG_{400} further discouraged the tight packing of the AuNPs on the IAPP species. On the other hand, IAPP monomers were the most effective for

promoting close packing of AuNPs. Consequently, steric separations between the AuNPs and their associations with the IAPP species translated to different efficiencies of plasmonic coupling upon light excitation.[204-206]

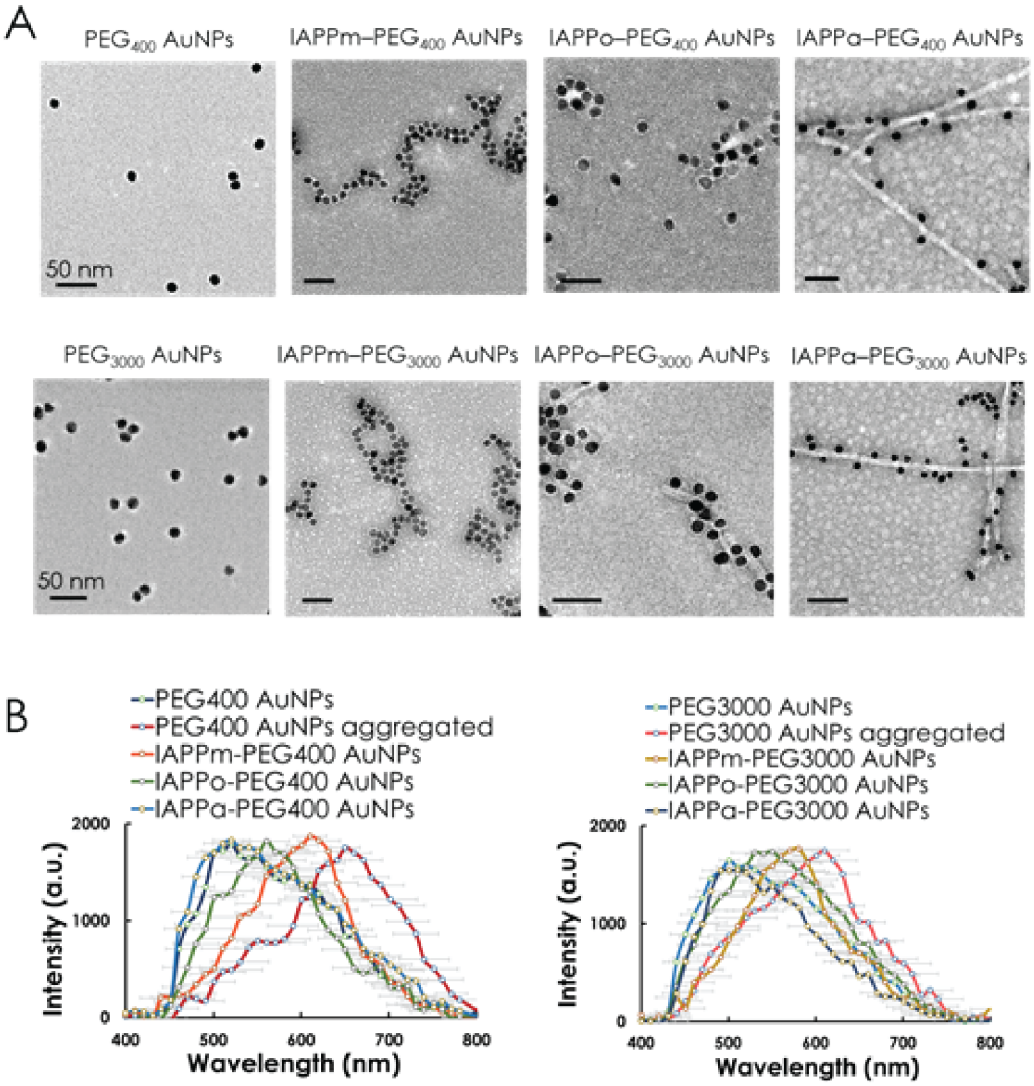

Figure 5.4 Characterization of PEG-AuNPs and PEG-AuNPs interacted with IAPP. Interaction of PEG_{400} and PEG_{3000} AuNPs with IAPP, observed with TEM (A). Corresponding hyperspectral SPR shifts for PEG_{400} and PEG_{3000} AuNPs (B). IAPP: 25 μM. Incubation: 5 min.

The UV-Vis absorbance characteristics of Cit AuNPs, PEG_{400} AuNPs and PEG_{3000} AuNPs are summarized and compared in **Figure 5.5a**. All three samples exhibited an identical extinction peak at circa 520 nm, consistent with our optical simulation results (COMSOL, **Figure 5.5b**, blue traces) suggesting that the AuNPs were well dispersed in the suspensions. Since HSI collects scattered light from samples, the scattering spectra of four models, i.e., a single AuNP, IAPPm-Cit AuNPs, IAPPo-Cit AuNPs and IAPPa-Cit AuNPs, were simulated. A 20 nm redshift of the scattering spectrum was observed for IAPPa-Cit AuNP interaction (**Figure 5.5b**). This redshift could be induced by the attraction between the oppositely charged Cit AuNPs and IAPP fibrils, which reduced the inter-particle distance compared with the nanoparticle control (blue trace) but was still sterically restricted by the large width of IAPPa (circa 7-12 nm).[175] A larger redshift of 77 nm was obtained for IAPPo-Cit AuNP complexes, due to the further reduced AuNP separations resulting from the smaller dimensions of IAPPo than IAPPa. The strongest plasmonic coupling and largest redshift (119 nm) occurred for IAPPm-Cit AuNPs complexes, a logical outcome given the smallest separations between the Cit AuNPs associated with IAPPm. These results corroborated the experimental observations (**Figure 5.2** and **Figure 5.4**, **Table 5.1**) that IAPP species at different aggregation stages can significantly impact the plasmonic coupling between IAPP-associated AuNPs (**Figure 5.5c**). In light of the significant and unidirectional SPR spectral shifts induced by IAPP in aggregation, especially for Cit AuNPs, HSI may serve as a facile alternative to conventional kinetics assays and electron microscopy for reporting the aggregation states of a range of amyloid proteins.

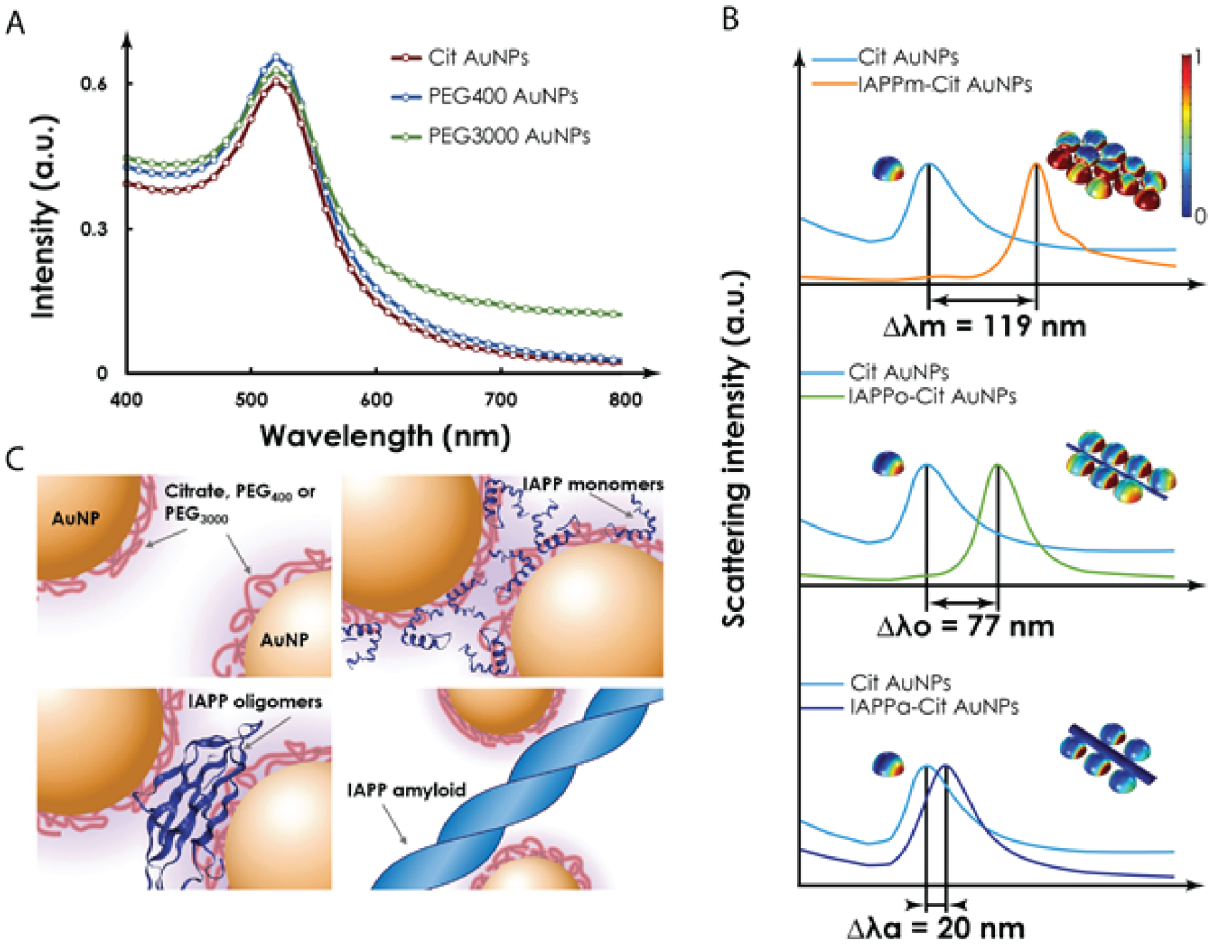

Figure 5.5 UV-Vis spectrometer and COMSOL simulation of AuNRs interacted with IAPPs. Measured UV-Vis absorbance of Cit, PEG400 and PEG3000 AuNPs (A). The simulated scattering spectra (normalized) and near-field scattering intensity distributions (insets) of Cit AuNPs, IAPPm-Cit AuNPs, IAPPo-Cit AuNPs and IAPPa-Cit AuNPs (B). Schematics of the spatial separations of AuNPs and their induced packing by the three types of IAPP species (C).

Circular dichroism (CD) spectroscopy was performed to further probe the secondary structures of the monomeric, oligomeric and fibrillar IAPP species. IAPPm possessed ~18% of both α helices and β sheets (**Figure 5.6a-b**). After binding with Cit AuNPs and PEG_{400} AuNPs, the α-helix content increased to 29% and 27% while the β-sheet content reduced to 14% and 12%, respectively (**Figure 5.6a-b**), which is comparable to the structural composition of IAPPo. IAPPo, upon

binding with Cit AuNPs and PEG_{400} AuNPs, assumed 25% and 27% of β sheets, respectively (**Figure 5.6c-d**). In contrast, PEG3000 AuNPs did not induce any conformational changes in IAPP after binding with IAPPm, IAPPo and IAPPa. In the case of IAPPa, none of the three types of AuNPs were able to trigger any conformational change in tightly packed β-sheets of IAPPa (**Figure 5.6e-f**).

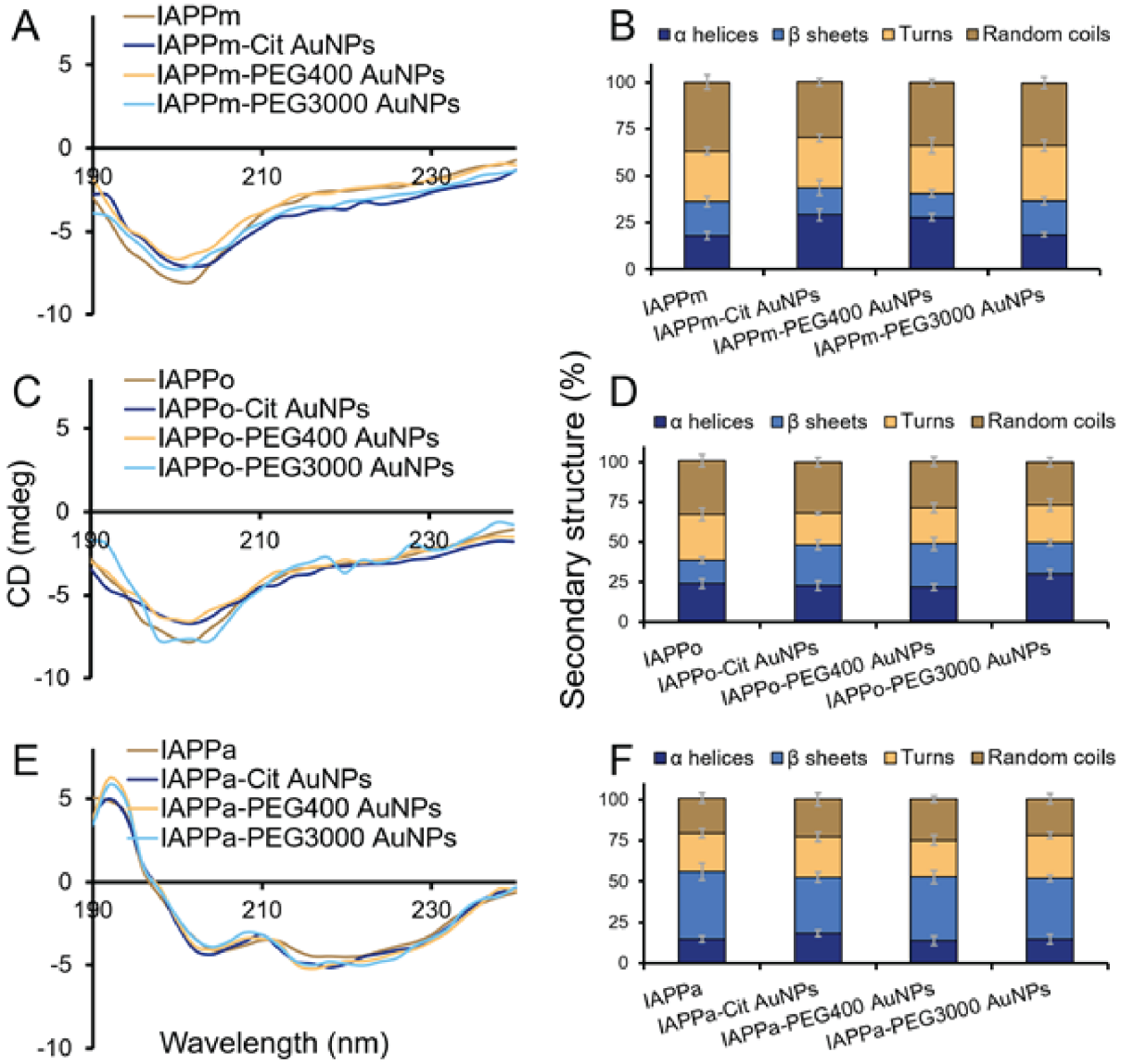

Figure 5.6 CD spectra (A, C, E) and percentage secondary structure (B, D, F) of IAPPm, IAPPo and IAPPa in the presence and absence of Cit AuNPs, PEG_{400} AuNPs and PEG_{3000} AuNPs. 100 μM of IAPP was incubated with 50 μM of AuNPs for 10 min before reading.

5.3.3 Immune response of T cells to three IAPP aggregation states and IAPP-AuNPs

Current *in vitro* studies of IAPP toxicity typically focus on cell viability, while the immune responses to amyloid proteins in various aggregation states, especially in the presence of nanoparticle inhibitors, have rarely been examined. Recent evidence suggests that IAPP aggregates can trigger the up-regulation of pro-inflammatory cytokines to impair β-cell insulin secretion.[207-208] Unveiling the pathological mechanisms of IAPP induced immune response can thus provide an alternative strategy based on anti-inflammatory therapies for protecting IAPP induced β-cell dysfunction.[199] Previous work investigating IAPP-associated immune response mainly relied on the "gold standard" enzyme-linked immunosorbent assay (ELISA), which requires a typical assay time of 4-8 h. The complicated sample preparation and long assay time of ELISA pose significant challenges for monitoring the dynamic secretion of immune cells upon IAPP exposure, especially considering the rapid monomer to fibril transformation of the peptide. Recently, we reported a microfluidic-based LSPR platform, which allowed rapid and sensitive detection of multiple cytokines in biological samples simultaneously.[6] In this study, the label-free and ease of integration characteristics of the LSPR platform provided a near real-time detection scheme for on-chip determination of cellular immune responses to the three IAPP forms as well as their associated AuNP complexes.

Jurkat human T cells were selected as a model system to investigate the IAPP and AuNP-IAPP "corona" induced immune responses.[209] The immune cell secretion after stimulation was assessed by quantifying two critical pro-inflammatory cytokines: tumor necrosis factor-alpha (TNF-α) and

interleukin 6 (IL-6). The three states of IAPP and the AuNP-IAPP complexes were prepared as illustrated in **Figure 5.7a**. After incubation with the T cells, the cell culture medium was collected and loaded into the prepared LSPR chip. The binding of secretory cytokines on antibody functionalized gold nanobipyramids (AuNBPs) led to plasmon resonance spectrum red-shifts and increased scattering intensities (**Figure 5.7b**). The optical signals were collected by an EMCCD in real-time and were converted into cytokine concentrations according to the established standard curves (**Figure 5.7c**). To validate the LSPR immunoassay, phorbol 12-myristate 13-acetate (PMA)/Ionomycin stimulated T cells were used as positive controls, showing significantly higher cytokine secretion levels than non-activated T cells (control) (**Figure 5.7d**).[210] Among the three IAPP species, IAPPo induced pronounced inflammatory responses from T cells, as indicated by the high level of TNF-α secretion (~2,000 pg/mL), while IAPPm and IAPPa elicited no significant cytokine secretions. This is consistent with the finding that IAPP in the low-order of oligomerization form can provide a Toll-like-receptor-2-(TLR2-) dependent stimulus for NF-κB activation, a known pathway for the expression of TNF-α.[199, 211] Interestingly, the T cells displayed a completely different cytokine release after incubating with the three types of AuNP-IAPP protein coronas. As indicated in **Figure 5.7e**, AuNP-IAPPm coronas induced a relatively higher amount of inflammatory cytokine secretions from T cells than the control IAPPm. This could be attributed to the promoted close packing of IAPPm on the AuNPs and thus accelerated oligomerization from IAPPm to IAPPo, as evidenced by our CD and ThT assays where similar structural compositions of α helices and β sheets were observed for AuNP-IAPPm corona and pure IAPPo. In contrast, a noticeable reduction of secretory cytokines was observed from T cells treated with AuNP-IAPPo (**Figure 5.7f**). Such inhibited immune responses may be consequential to the increased peptide dimensions and altered secondary structure of the peptide after AuNP adsorption, thereby

prohibiting the interaction between IAPPo and the T cell surface receptor.[212] The T cells showed minimal immune responses to IAPPa and AuNP-IAPPa coronas, which strongly agrees with our observations that IAPPa was less toxic than oligomers and remained structurally stable after incubating with AuNPs (**Figure 5.7g**).

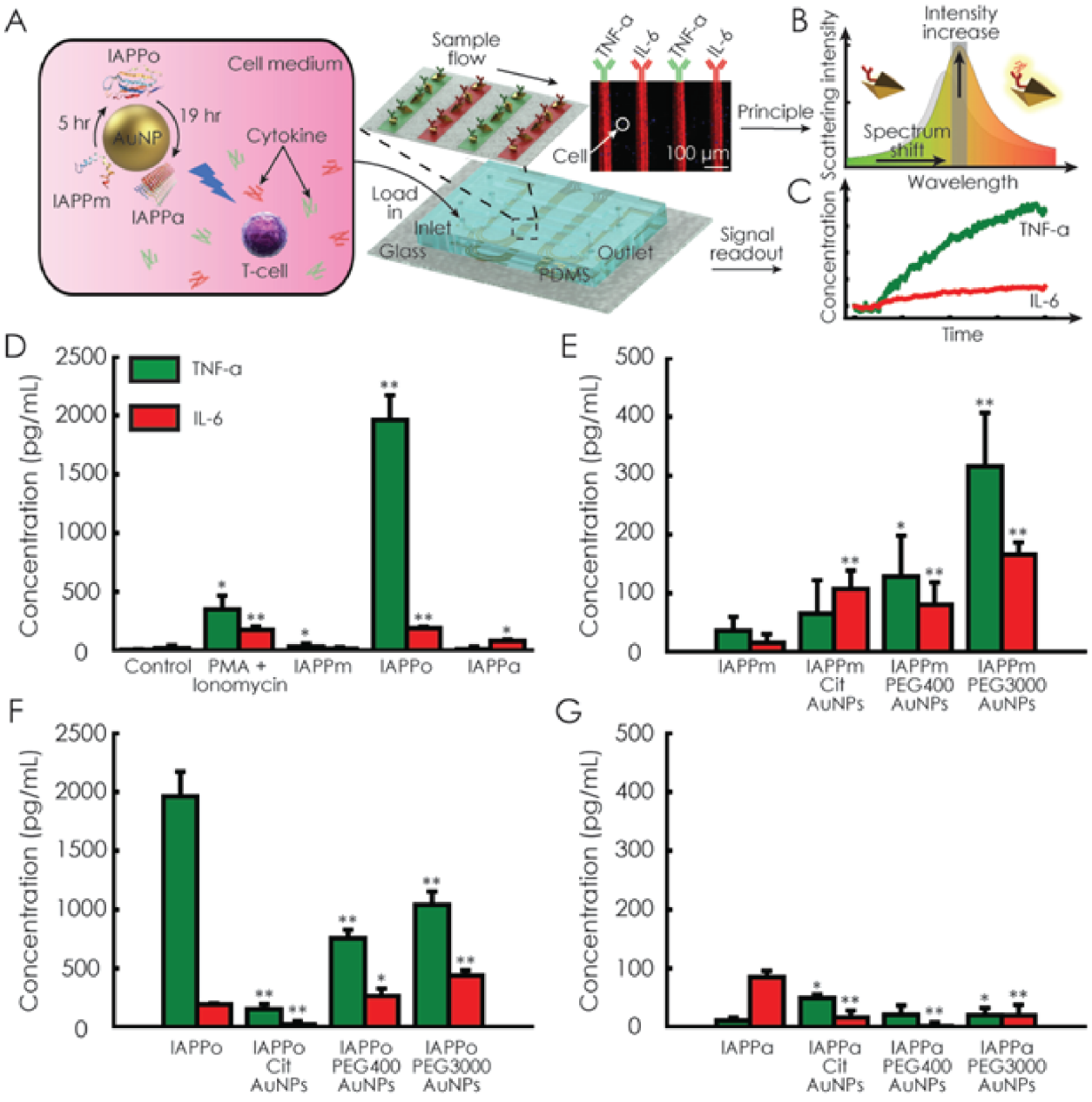

Figure 5.7 The LSPR immunoassay for IAPP and AuNP-IAPP induced T-cell immune response detection. Jurkat T cells were stimulated by as-prepared pure IAPP or AuNP-IAPP coronas, and the cellular immune response was determined by simultaneously measuring the TNF-α and IL-6 concentrations in the collected cell culture medium using the LSPR microfluidic chip (A). The specific binding events that occurred on the AuNBP surface yielded a localized refractive index change and a larger scattering cross-section, resulting in a red-shifted peak and an increased scattering intensity. By employing a band-pass filter (645-695 nm) and an EMCCD, the secretory cytokine levels were quantified by measuring the scattering light intensity changes at the designed resonance wavelengths (B). Representative real-time detection curves of cytokine concentrations for T cells stimulated with IAPPo (C). Cytokine secretion profiles of T cells for the control, PMA + ionomycine (positive control), IAPPm, IAPPo, IAPPa stimulation (D). Cytokine secretion profiles for T cells activated by IAPPm (E), IAPPo (F), IAPPa (G) in the presence of the three types of AuNPs. Data represent the mean ± standard error of the mean with $n \geqslant 3$. P-values were calculated using the student's t-test. *, $P < 0.05$; **, $P < 0.01$.

It is known that the surface morphology and chemistry of AuNPs could elicit physicochemical and pathological changes in protein conformation upon nanoparticle-protein interactions.[213-214] Our results suggest that the smaller sized Cit AuNPs facilitated their interactions with IAPPm and IAPPo with considerable secondary structure changes induced resulting from their larger surface curvatures and higher surface energies as compared to the PEGylated AuNPs. This could lead to the unfolding of IAPP and alter the subsequent T-cell immune responses. The attachment of long PEG chains on the AuNPs imposed a steric hindrance and entailed strong anti-peptide fouling and less protein misfolding. As such, the differential immune responses from T cells triggered by IAPP and AuNP-IAPP species may be understood as consequential to the structural and toxicity profiles

of the three states of IAPP as well as the differential physicochemical properties of the AuNPs derived from their surface ligands.

5.4 Conclusion

In summary, we have demonstrated HSI and LSPR platforms as two new strategies for differentiating the aggregation states of human IAPP and their elicited immune responses in T cells. In the HSI scheme, the monomeric, oligomeric/protofibrillar and fibrillar IAPP states spatially separated ligand-coated AuNPs, which translated to easily discernible, unidirectional SPR spectral shifts upon light excitation. In the LSPR scheme, the SPR shifts of gold nanobipyramids served as reporters of cytokine secretion by immune cells exposed to IAPP aggregates. IAPPo, being the most toxic form of the three aggregation states, elicited the highest level of TNF-α cytokine secretion, while Cit AuNPs were the most effective in suppressing immune response to IAPPo than PEG_{400} or PEG_{3000} AuNPs. This finding suggests that nanoparticles stabilized with ligands of shorter chain lengths and moderate antifouling capacities (e.g., Cit over PEG_{400} and PEG_{3000}) are more effective reporters of protein aggregation and inhibitors against amyloid protein toxicity. These findings have implications for both fundamental research on protein misfolding and therapeutic development against amyloid diseases with nanotechnologies.

Chapter 6

Overall Conclusion and Future Direction

The immune system is a complicated network involving different immune cells and proteins to fight against pathogens and protect the body. It comprises three primary lines of defense: (*i*) physical and chemical barriers; (*ii*) non-specific innate responses; (*iii*) specific adaptive responses. Although the role of the immune system is conceptually clear, the defense mechanism is not fully understood due to the complex functional interactions between biomolecules and immune cells. Among these biomolecules, cytokine, a category of low molecular weight signaling protein secreted by a range of cells in the body, is critical in regulating the activation and inhibition of immune response. Since they are the major communication mechanism for immune cells, the dysregulated release of cytokines can be life-threatening. For example, sepsis is associated with infections that cause immune dysregulation and result in multiple organs failure. Therefore, monitoring cytokine levels reveals transient immune status in different inflammatory diseases, but also provides valuable clinical implications for the early identification of these COVID-19 patients who are likely to progress to critically ill. However, the accurate quantification of cytokines remains challenging due to their low level in circulation and short half-lives. Furthermore, clinical

samples subject to repeated freeze-thaw cycles can induce an inaccurate cytokine concentration. To tackle these challenges, in this work, we have demonstrated the development of next-generation point-of-care nanoplasmonic immunoassays from the following aspects: (*i*) scalable assay manufacturing (**Chapter 2**); (*ii*) improved sensing performance (**Chapter 3** and **4**), and (*iii*) fast assay time (**Chapter 5**).

For fabrication of immunoassay, current challenges are mask-based techniques require the prefabrication of a sophisticated silicon master with patterned micro-feature on the surface, which is costly and time-consuming, while mask-free technologies suffer from low throughput and harsh processing conditions. In **Chapter 2**, we firstly developed a scalable patterning technique utilizing the hierarchically anisotropic microstructure of weasel hair. Liquid can be trapped between the weasel hairs and upon deformation, transferred onto the substrate in a controllable manner. Associated with the solution-based nanoparticle functionalization method, a 3-plex immunoassay with five repeats can be produced in less than three minutes. The developed biosensing platform was employed to profile mouse macrophage immunophenotype. Although the patterning conditions have been carefully investigated and the optimized parameters have been given, the fluid mechanics have not been fully understood. Of particular interest is how Laplace pressure difference and asymmetrical retention force have changed when weasel hairs are mechanically deformed during the patterning process and how such physics can better guide people dispense microliter liquid in a high uniformity. The other future direction is if we can pattern anisotropic nanoparticles with certain self-alignment. Such self-aligned anisotropic nanoparticles can be efficiently activated by polarized incident light, thus providing a higher LSPR signal.

To improve the sensing performance of the current immunoassay, people have adopted: (*i*) subsequent signal amplification process; (*ii*) novel materials with attractive properties, and (*iii*)

efficient mass transportation. In **Chapter 3**, we have improved the sensitivity of the current antibody-based LSPR immunoassay by the design of a new probe element derived from a conventional antibody, i.e., ADPA. Owing to its smaller dimension compared to traditional antibodies, biorecognition events were sensed in a closer proximity on the plasmonic nanoparticle surface, resulting in a larger optical signal (scattering light intensity). FEA simulation has been performed to predict the scattering spectra. We constructed an ADPA-based LSPR biosensing platform and an 8-times lower LOD (4.56pg/mL) has been found in comparison with antibody-based LSPR biosensor. Taking advantage of the ADPA-based sensor, we have characterized the IL-6 level from SARS-CoV-2 spike protein stimulated macrophages and epithelial cells. This project is the first demonstration of ADPA design and ADPA-based LSPR immunoassay. The next step will be the design of more ADPA against targets of interest. Of equivalent importance is the study on how ADPA density on nanoparticle will play a role and how such density will affect affinity and specificity. In **Chapter 4**, we have demonstrated a digital LSPR immunoassay with further enhanced sensing performance to meet the emerging needs for cytokine storm monitoring in COVID-19 patients. We have integrated a highly functional microfluidic device (7 channels, 6 repeats) with a digital LSPR sensing methodology and assisted by CNN-based particle counting algorithm, we are able to simultaneously quantify 6 target cytokines with a LOD down to 0.46 - 1.36 pg/mL. 40 serum samples from hospitalized COVID-19 patients were analyzed in 5 hours with a total of 1440 tests from 5 biochips, rendering our platform being a practical tool for rapid and precise immune monitoring. Future directions of this project will be: (*i*) the development of a more sophisticated microfluidic device with more compact channel design allowing the simultaneous detection of more analytes and (*ii*) the further integration of current platform with different functional modules (sample preparation module and waste collection module) in one

biochip. Eventually, we envision it as an automatic and user-friendly biosensing platform in the near future.

Regarding the rapid detection of cytokine, current "gold standard" method, ELISA, fails to offer final results in a fine temporal resolution. In Chapter 5, taking advantage of our label-free LSPR sensing scheme, we have revealed transient T cell responses to three different aggregation stages of hIAPP and novel drug (AuNP with varying surfactants) treated hIAPP. We have identified IAPPo as the most toxic species as evidenced by highest TNF-α secretion from T cells and Cit-AuNP has been suggested as the most effective hIAPP inhibitor. An attractive direction will be the development of an *in-situ* biosensing platform. Instead of taking out the cell medium and manually assaying, the *in-situ* cytokine measurements will not only reveal the real-time cytokine secretion from specific cell groups but also reflect the original cytokine level.

Reference

(1) Vert, M.; Doi, Y.; Hellwich, K.-H.; Hess, M.; Hodge, P.; Kubisa, P.; Rinaudo, M.; Schué, F. Terminology for Biorelated Polymers and Applications (Iupac Recommendations 2012). *Pure and Applied Chemistry* **2012,** *84* (2), 377-410.

(2) Khan, I.; Saeed, K.; Khan, I. Nanoparticles: Properties, Applications and Toxicities. *Arabian journal of chemistry* **2019,** *12* (7), 908-931.

(3) Pokropivny, V.; Skorokhod, V. Classification of Nanostructures by Dimensionality and Concept of Surface Forms Engineering in Nanomaterial Science. *Materials Science and Engineering: C* **2007,** *27* (5-8), 990-993.

(4) Gao, Z.; Lv, S.; Xu, M.; Tang, D. High-Index {Hk 0} Faceted Platinum Concave Nanocubes with Enhanced Peroxidase-Like Activity for an Ultrasensitive Colorimetric Immunoassay of the Human Prostate-Specific Antigen. *Analyst* **2017,** *142* (6), 911-917.

(5) Gao, Z.; Shao, S.; Gao, W.; Tang, D.; Tang, D.; Zou, S.; Kim, M. J.; Xia, X. Morphology-Invariant Metallic Nanoparticles with Tunable Plasmonic Properties. *ACS nano* **2021,** *15* (2), 2428-2438.

(6) Chen, P.; Chung, M. T.; McHugh, W.; Nidetz, R.; Li, Y.; Fu, J.; Cornell, T. T.; Shanley, T. P.; Kurabayashi, K. Multiplex Serum Cytokine Immunoassay Using Nanoplasmonic Biosensor Microarrays. *ACS nano* **2015,** *9* (4), 4173-4181.

(7) Ogueri, K. S.; Laurencin, C. T. Nanofiber Technology for Regenerative Engineering. *ACS nano* **2020,** *14* (8), 9347-9363.

(8) VahidMohammadi, A.; Mojtabavi, M.; Caffrey, N. M.; Wanunu, M.; Beidaghi, M. Assembling 2d Mxenes into Highly Stable Pseudocapacitive Electrodes with High Power and Energy Densities. *Advanced Materials* **2019,** *31* (8), 1806931.

(9) Jeevanandam, J.; Barhoum, A.; Chan, Y. S.; Dufresne, A.; Danquah, M. K. Review on Nanoparticles and Nanostructured Materials: History, Sources, Toxicity and Regulations. *Beilstein journal of nanotechnology* **2018,** *9* (1), 1050-1074.

(10) Wang, B.; He, J.; Liu, F.; Ding, L. Rapid Synthesis of Cu2o/Cuo/Rgo with Enhanced Sensitivity for Ascorbic Acid Biosensing. *Journal of Alloys and Compounds* **2017,** *693*, 902-908.

(11) C Thomas, S.; Kumar Mishra, P.; Talegaonkar, S. Ceramic Nanoparticles: Fabrication Methods and Applications in Drug Delivery. *Current pharmaceutical design* **2015,** *21* (42), 6165-6188.

(12) Rao, J. P.; Geckeler, K. E. Polymer Nanoparticles: Preparation Techniques and Size-Control Parameters. *Progress in polymer science* **2011,** *36* (7), 887-913.

(13) Schoenmaker, L.; Witzigmann, D.; Kulkarni, J. A.; Verbeke, R.; Kersten, G.; Jiskoot, W.; Crommelin, D. J. Mrna-Lipid Nanoparticle Covid-19 Vaccines: Structure and Stability. *International Journal of Pharmaceutics* **2021,** *601*, 120586.

(14) Huang, X.; El-Sayed, M. A. Gold Nanoparticles: Optical Properties and Implementations in Cancer Diagnosis and Photothermal Therapy. *Journal of advanced research* **2010,** *1* (1), 13-28.

(15) Javed, I.; He, J.; Kakinen, A.; Faridi, A.; Yang, W.; Davis, T. P.; Ke, P. C.; Chen, P. Probing the Aggregation and Immune Response of Human Islet Amyloid Polypeptides with Ligand-Stabilized Gold Nanoparticles. *ACS applied materials & interfaces* **2019,** *11* (11), 10462-10471.

(16) Watanabe, K. Photochemistry on Nanoparticles. In *Encyclopedia of Interfacial Chemistry: Surface Science and Electrochemistry*; Elsevier: 2018; pp 563-572.

(17) Mejía-Salazar, J.; Oliveira Jr, O. N. Plasmonic Biosensing: Focus Review. *Chemical reviews* **2018,** *118* (20), 10617-10625.

(18) Naresh, V.; Lee, N. A Review on Biosensors and Recent Development of Nanostructured Materials-Enabled Biosensors. *Sensors* **2021,** *21* (4), 1109.

(19) Bhalla, N.; Jolly, P.; Formisano, N.; Estrela, P. Essays Biochem.,". *Introduction to biosensors* **2016,** *60* (1), 1-8.
(20) Heineman, W. R.; Jensen, W. B. Leland C. Clark Jr.(1918–2005). *Biosensors and Bioelectronics* **2006,** *8* (21), 1403-1404.
(21) Clark Jr, L. C.; Lyons, C. Electrode Systems for Continuous Monitoring in Cardiovascular Surgery. *Annals of the New York Academy of sciences* **1962,** *102* (1), 29-45.
(22) Guilbault, G. G.; Montalvo Jr, J. G. Urea-Specific Enzyme Electrode. *Journal of the American Chemical Society* **1969,** *91* (8), 2164-2165.
(23) Clemens, A. The Development of Biostator, a Glucose Controlled Insulin Infusion System (Gciis). *Horm Metab Res* **1977,** *7*, 23-33.
(24) Geyssant, A.; Dormois, D.; Barthelemy, J.; Lacour, J. Lactate Determination with the Lactate Analyser La 640: A Critical Study. *Scandinavian journal of clinical and laboratory investigation* **1985,** *45* (2), 145-149.
(25) Liedberg, B.; Nylander, C.; Lunström, I. Surface Plasmon Resonance for Gas Detection and Biosensing. *Sensors and actuators* **1983,** *4*, 299-304.
(26) He, J.; Brimmo, A. T.; Qasaimeh, M. A.; Chen, P.; Chen, W. Recent Advances and Perspectives in Microfluidics‐Based Single‐Cell Biosensing Techniques. *Small Methods* **2017,** *1* (10), 1700192.
(27) Syahir, A.; Usui, K.; Tomizaki, K.-y.; Kajikawa, K.; Mihara, H. Label and Label-Free Detection Techniques for Protein Microarrays. *Microarrays* **2015,** *4* (2), 228-244.
(28) Giepmans, B. N.; Adams, S. R.; Ellisman, M. H.; Tsien, R. Y. The Fluorescent Toolbox for Assessing Protein Location and Function. *science* **2006,** *312* (5771), 217-224.
(29) Petryayeva, E.; Algar, W. R.; Medintz, I. L. Quantum Dots in Bioanalysis: A Review of Applications across Various Platforms for Fluorescence Spectroscopy and Imaging. *Applied spectroscopy* **2013,** *67* (3), 215-252.
(30) Szkola, A.; Linares, E.; Worbs, S.; Dorner, B.; Dietrich, R.; Märtlbauer, E.; Niessner, R.; Seidel, M. Rapid and Simultaneous Detection of Ricin, Staphylococcal Enterotoxin B and Saxitoxin by Chemiluminescence-Based Microarray Immunoassay. *Analyst* **2014,** *139* (22), 5885-5892.
(31) Domon, B.; Aebersold, R. Mass Spectrometry and Protein Analysis. *science* **2006,** *312* (5771), 212-217.
(32) Niederkofler, E. E.; Tubbs, K. A.; Kiernan, U. A.; Nedelkov, D.; Nelson, R. W. Novel Mass Spectrometric Immunoassays for the Rapid Structural Characterization of Plasma Apolipoproteins. *Journal of lipid research* **2003,** *44* (3), 630-639.
(33) Niederkofler, E. E.; Tubbs, K. A.; Gruber, K.; Nedelkov, D.; Kiernan, U. A.; Williams, P.; Nelson, R. W. Determination of B-2 Microglobulin Levels in Plasma Using a High-Throughput Mass Spectrometric Immunoassay System. *Analytical chemistry* **2001,** *73* (14), 3294-3299.
(34) Yukihira, D.; Miura, D.; Saito, K.; Takahashi, K.; Wariishi, H. Maldi− Ms-Based High-Throughput Metabolite Analysis for Intracellular Metabolic Dynamics. *Analytical chemistry* **2010,** *82* (10), 4278-4282.
(35) Han, J.; Zhang, J.; Xia, Y.; Li, S.; Jiang, L. An Immunoassay in Which Magnetic Beads Act Both as Collectors and Sensitive Amplifiers for Detecting Antigens in a Microfluidic Chip (Mfc)–Quartz Crystal Microbalance (Qcm) System. *Colloids and Surfaces A: Physicochemical and Engineering Aspects* **2011,** *379* (1-3), 2-9.
(36) Salam, F.; Uludag, Y.; Tothill, I. E. Real-Time and Sensitive Detection of Salmonella Typhimurium Using an Automated Quartz Crystal Microbalance (Qcm) Instrument with Nanoparticles Amplification. *Talanta* **2013,** *115*, 761-767.
(37) SOARES, E. C. d. L. Desenvolvimento De Testes Diagnósticos Para Hepatite B Baseados Em Imunossensores. **2016**.
(38) Sauerbrey, G. The Use of Quarts Oscillators for Weighing Thin Layers and for Microweighing. *Z. Phys.* **1959,** *155*, 206-222.

(39) Lee, J.; Choi, Y.-S.; Lee, Y.; Lee, H. J.; Lee, J. N.; Kim, S. K.; Han, K. Y.; Cho, E. C.; Park, J. C.; Lee, S. S. Sensitive and Simultaneous Detection of Cardiac Markers in Human Serum Using Surface Acoustic Wave Immunosensor. *Analytical chemistry* **2011,** *83* (22), 8629-8635.
(40) Siegmann-Thoss, C.; Renneberg, R.; Glatz, J. F.; Spener, F. Enzyme Immunosensor for Diagnosis of Myocardial Infarction. *Sensors and Actuators B: Chemical* **1996,** *30* (1), 71-76.
(41) Liu, Y.; Tuleouva, N.; Ramanculov, E.; Revzin, A. Aptamer-Based Electrochemical Biosensor for Interferon Gamma Detection. *Analytical chemistry* **2010,** *82* (19), 8131-8136.
(42) Zhou, Q.; Rahimian, A.; Son, K.; Shin, D.-S.; Patel, T.; Revzin, A. Development of an Aptasensor for Electrochemical Detection of Exosomes. *Methods* **2016,** *97*, 88-93.
(43) Hsieh, K.; Patterson, A. S.; Ferguson, B. S.; Plaxco, K. W.; Soh, H. T. Rapid, Sensitive, and Quantitative Detection of Pathogenic DNA at the Point of Care through Microfluidic Electrochemical Quantitative Loop-Mediated Isothermal Amplification. *Angewandte Chemie International Edition* **2012,** *51* (20), 4896-4900.
(44) Guo, X.; Kulkarni, A.; Doepke, A.; Halsall, H. B.; Iyer, S.; Heineman, W. R. Carbohydrate-Based Label-Free Detection of Escherichia Coli Orn 178 Using Electrochemical Impedance Spectroscopy. *Analytical chemistry* **2012,** *84* (1), 241-246.
(45) Fenzl, C.; Hirsch, T.; Wolfbeis, O. S. Photonic Crystals for Chemical Sensing and Biosensing. *Angewandte Chemie International Edition* **2014,** *53* (13), 3318-3335.
(46) Vollmer, F.; Arnold, S. Whispering-Gallery-Mode Biosensing: Label-Free Detection Down to Single Molecules. *Nature methods* **2008,** *5* (7), 591-596.
(47) Chen, P.; Huang, N.-T.; Chung, M.-T.; Cornell, T. T.; Kurabayashi, K. Label-Free Cytokine Micro-and Nano-Biosensing Towards Personalized Medicine of Systemic Inflammatory Disorders. *Advanced drug delivery reviews* **2015,** *95*, 90-103.
(48) Ouellet, E.; Lausted, C.; Lin, T.; Yang, C. W. T.; Hood, L.; Lagally, E. T. Parallel Microfluidic Surface Plasmon Resonance Imaging Arrays. *Lab on a Chip* **2010,** *10* (5), 581-588.
(49) Sonato, A.; Agostini, M.; Ruffato, G.; Gazzola, E.; Liuni, D.; Greco, G.; Travagliati, M.; Cecchini, M.; Romanato, F. A Surface Acoustic Wave (Saw)-Enhanced Grating-Coupling Phase-Interrogation Surface Plasmon Resonance (Spr) Microfluidic Biosensor. *Lab on a Chip* **2016,** *16* (7), 1224-1233.
(50) Liu, J.; Eddings, M. A.; Miles, A. R.; Bukasov, R.; Gale, B. K.; Shumaker-Parry, J. S. In Situ Microarray Fabrication and Analysis Using a Microfluidic Flow Cell Array Integrated with Surface Plasmon Resonance Microscopy. *Analytical chemistry* **2009,** *81* (11), 4296-4301.
(51) Whitesides, G. M. The Origins and the Future of Microfluidics. *nature* **2006,** *442* (7101), 368-373.
(52) Nielsen, J. B.; Hanson, R. L.; Almughamsi, H. M.; Pang, C.; Fish, T. R.; Woolley, A. T. Microfluidics: Innovations in Materials and Their Fabrication and Functionalization. *Analytical chemistry* **2019,** *92* (1), 150-168.
(53) Ma, C.; Witkowski, M. T.; Harris, J.; Dolgalev, I.; Sreeram, S.; Qian, W.; Tong, J.; Chen, X.; Aifantis, I.; Chen, W. Leukemia-on-a-Chip: Dissecting the Chemoresistance Mechanisms in B Cell Acute Lymphoblastic Leukemia Bone Marrow Niche. *Science advances* **2020,** *6* (44), eaba5536.
(54) Zhu, J.; He, J.; Verano, M.; Brimmo, A. T.; Glia, A.; Qasaimeh, M. A.; Chen, P.; Aleman, J. O.; Chen, W. An Integrated Adipose-Tissue-on-Chip Nanoplasmonic Biosensing Platform for Investigating Obesity-Associated Inflammation. *Lab on a Chip* **2018,** *18* (23), 3550-3560.
(55) Liu, Y.; Yang, M.; Deng, Y.; Su, G.; Enninful, A.; Guo, C. C.; Tebaldi, T.; Zhang, D.; Kim, D.; Bai, Z. High-Spatial-Resolution Multi-Omics Sequencing Via Deterministic Barcoding in Tissue. *Cell* **2020,** *183* (6), 1665-1681. e18.
(56) Liao, Z.; Zhang, Y.; Li, Y.; Miao, Y.; Gao, S.; Lin, F.; Deng, Y.; Geng, L. Microfluidic Chip Coupled with Optical Biosensors for Simultaneous Detection of Multiple Analytes: A Review. *Biosensors and Bioelectronics* **2019,** *126*, 697-706.
(57) Song, Y.; Lin, B.; Tian, T.; Xu, X.; Wang, W.; Ruan, Q.; Guo, J.; Zhu, Z.; Yang, C. Recent Progress in Microfluidics-Based Biosensing. *Analytical chemistry* **2018,** *91* (1), 388-404.

(58) Kabel, A. M. Relationship between Cancer and Cytokines. *Journal of Cancer Research and Treatment* **2014,** *2* (2), 41-43.
(59) Neurath, M. F. Cytokines in Inflammatory Bowel Disease. *Nature Reviews Immunology* **2014,** *14* (5), 329-342.
(60) Jun-Ming, Z.; Jianxiong, A. Cytokines, Inflammation and Pain. *International Anesthesiology Clinics* **2007,** *45* (2), 27-37.
(61) Liu, C.; Chu, D.; Kalantar‐Zadeh, K.; George, J.; Young, H. A.; Liu, G. Cytokines: From Clinical Significance to Quantification. *Advanced Science* **2021**, 2004433.
(62) Ruan, Q.; Yang, K.; Wang, W.; Jiang, L.; Song, J. Clinical Predictors of Mortality Due to Covid-19 Based on an Analysis of Data of 150 Patients from Wuhan, China. *Intensive care medicine* **2020,** *46* (5), 846-848.
(63) Del Valle, D. M.; Kim-Schulze, S.; Huang, H.-H.; Beckmann, N. D.; Nirenberg, S.; Wang, B.; Lavin, Y.; Swartz, T. H.; Madduri, D.; Stock, A. An Inflammatory Cytokine Signature Predicts Covid-19 Severity and Survival. *Nature medicine* **2020,** *26* (10), 1636-1643.
(64) Whiteside, T. L. Cytokines and Cytokine Measurements in a Clinical Laboratory. *Clinical and Diagnostic Laboratory Immunology* **1994,** *1* (3), 257.
(65) Oliver, J.; Bland, L.; Oettinger, C.; Arduino, M.; McAllister, S.; Aguero, S.; Favero, M. Cytokine Kinetics in an in Vitro Whole Blood Model Following an Endotoxin Challenge. *Lymphokine and cytokine research* **1993,** *12* (2), 115-120.
(66) Zhou, X.; Fragala, M. S.; McElhaney, J. E.; Kuchel, G. A. Conceptual and Methodological Issues Relevant to Cytokine and Inflammatory Marker Measurements in Clinical Research. *Current opinion in clinical nutrition and metabolic care* **2010,** *13* (5), 541.
(67) Andersson, R.; Andersson, B.; Andersson, E.; Eckerwall, G.; Nordén, M.; Tingstedt, B. Immunomodulation in Surgical Practice. *HPB* **2006,** *8* (2), 116-123.
(68) Singh, A.; Peppas, N. A. Hydrogels and Scaffolds for Immunomodulation. *Advanced materials* **2014,** *26* (38), 6530-6541.
(69) He, J.; Brimmo, A. T.; Qasaimeh, M. A.; Chen, P.; Chen, W. Recent Advances and Perspectives in Microfluidics-Based Single-Cell Biosensing Techniques. *Small Methods* **2017,** *1* (10), 1700192, DOI: https://doi.org/10.1002/smtd.201700192.
(70) Hou, J.; Liu, T.; Chen, R.; Liu, J.; Chen, J.; Zhao, C.; Yin, L.; Li, C.; Xu, X.; Shi, Q. Guided Protein/Cell Patterning on Superhydrophilic Polymer Brushes Functionalized with Mussel-Inspired Polydopamine Coatings. *Chemical Communications* **2017,** *53* (50), 6708-6711.
(71) Corletto, A.; Yu, L.; Shearer, C. J.; Gibson, C. T.; Shapter, J. G. Direct‐Patterning Swcnts Using Dip Pen Nanolithography for Swcnt/Silicon Solar Cells. *Small* **2018,** *14* (16), 1800247.
(72) Zhang, Z.; Zhang, X.; Xin, Z.; Deng, M.; Wen, Y.; Song, Y. Controlled Inkjetting of a Conductive Pattern of Silver Nanoparticles Based on the Coffee‐Ring Effect. *Advanced Materials* **2013,** *25* (46), 6714-6718.
(73) Lau, U. Y.; Saxer, S. S.; Lee, J.; Bat, E.; Maynard, H. D. Direct Write Protein Patterns for Multiplexed Cytokine Detection from Live Cells Using Electron Beam Lithography. *Acs Nano* **2016,** *10* (1), 723-729.
(74) Wang, Q.; Meng, Q.; Wang, P.; Liu, H.; Jiang, L. Bio-Inspired Direct Patterning Functional Nanothin Microlines: Controllable Liquid Transfer. *ACS nano* **2015,** *9* (4), 4362-4370.
(75) Wang, Q.; Su, B.; Liu, H.; Jiang, L. Chinese Brushes: Controllable Liquid Transfer in Ratchet Conical Hairs. *Advanced Materials* **2014,** *26* (28), 4889-4894.
(76) Dugas, V.; Broutin, J.; Souteyrand, E. Droplet Evaporation Study Applied to DNA Chip Manufacturing. *Langmuir* **2005,** *21* (20), 9130-9136.
(77) Yunker, P. J.; Still, T.; Lohr, M. A.; Yodh, A. Suppression of the Coffee-Ring Effect by Shape-Dependent Capillary Interactions. *Nature* **2011,** *476* (7360), 308-311.

(78) Amenabar, I.; Poly, S.; Nuansing, W.; Hubrich, E. H.; Govyadinov, A. A.; Huth, F.; Krutokhvostov, R.; Zhang, L.; Knez, M.; Heberle, J. Structural Analysis and Mapping of Individual Protein Complexes by Infrared Nanospectroscopy. *Nature communications* **2013,** *4* (1), 1-9.
(79) Grdadolnik, J.; Maréchal, Y. Bovine Serum Albumin Observed by Infrared Spectrometry. I. Methodology, Structural Investigation, and Water Uptake. *Biopolymers: Original Research on Biomolecules* **2001,** *62* (1), 40-53.
(80) Martinez, F. O.; Sica, A.; Mantovani, A.; Locati, M. Macrophage Activation and Polarization. *Front Biosci* **2008,** *13* (1), 453-461.
(81) Noy, R.; Pollard, J. W. Tumor-Associated Macrophages: From Mechanisms to Therapy. *Immunity* **2014,** *41* (1), 49-61.
(82) Murray, P. J. Macrophage Polarization. *Annual review of physiology* **2017,** *79*, 541-566.
(83) Dutta, K.; Mishra, M. K.; Nazmi, A.; Kumawat, K. L.; Basu, A. Minocycline Differentially Modulates Macrophage Mediated Peripheral Immune Response Following Japanese Encephalitis Virus Infection. *Immunobiology* **2010,** *215* (11), 884-893.
(84) Lee, M.; Park, C.-S.; Lee, Y.-R.; Im, S.-A.; Song, S.; Lee, C.-K. Resiquimod, a Tlr7/8 Agonist, Promotes Differentiation of Myeloid-Derived Suppressor Cells into Macrophages and Dendritic Cells. *Archives of pharmacal research* **2014,** *37* (9), 1234-1240.
(85) Pajarinen, J.; Tamaki, Y.; Antonios, J. K.; Lin, T. H.; Sato, T.; Yao, Z.; Takagi, M.; Konttinen, Y. T.; Goodman, S. B. Modulation of Mouse Macrophage Polarization in Vitro Using Il‐4 Delivery by Osmotic Pumps. *Journal of biomedical materials research Part A* **2015,** *103* (4), 1339-1345.
(86) Hachim, D.; LoPresti, S. T.; Yates, C. C.; Brown, B. N. Shifts in Macrophage Phenotype at the Biomaterial Interface Via Il-4 Eluting Coatings Are Associated with Improved Implant Integration. *Biomaterials* **2017,** *112*, 95-107.
(87) Mangalmurti, N.; Hunter, C. A. Cytokine Storms: Understanding Covid-19. *Immunity* **2020**.
(88) Qin, C.; Zhou, L.; Hu, Z.; Zhang, S.; Yang, S.; Tao, Y.; Xie, C.; Ma, K.; Shang, K.; Wang, W. Dysregulation of Immune Response in Patients with Coronavirus 2019 (Covid-19) in Wuhan, China. *Clinical infectious diseases* **2020,** *71* (15), 762-768.
(89) Tan, M.; Liu, Y.; Zhou, R.; Deng, X.; Li, F.; Liang, K.; Shi, Y. Immunopathological Characteristics of Coronavirus Disease 2019 Cases in Guangzhou, China. *Immunology* **2020,** *160* (3), 261-268.
(90) Whetton, A. D.; Preston, G. W.; Abubeker, S.; Geifman, N. Proteomics and Informatics for Understanding Phases and Identifying Biomarkers in Covid-19 Disease. *Journal of proteome research* **2020,** *19* (11), 4219-4232.
(91) Russell, S. M.; Alba-Patiño, A.; Barón, E.; Borges, M.; Gonzalez-Freire, M.; De La Rica, R. Biosensors for Managing the Covid-19 Cytokine Storm: Challenges Ahead. *ACS sensors* **2020,** *5* (6), 1506-1513.
(92) Shang, L.; Zhao, J.; Hu, Y.; Du, R.; Cao, B. On the Use of Corticosteroids for 2019-Ncov Pneumonia. *The Lancet* **2020,** *395* (10225), 683-684.
(93) Oh, B.-R.; Huang, N.-T.; Chen, W.; Seo, J. H.; Chen, P.; Cornell, T. T.; Shanley, T. P.; Fu, J.; Kurabayashi, K. Integrated Nanoplasmonic Sensing for Cellular Functional Immunoanalysis Using Human Blood. *ACS nano* **2014,** *8* (3), 2667-2676.
(94) He, J.; Jiang, Y.; Peng, J.; Li, C.; Yan, B.; Wang, X. Fast Synthesis of Hierarchical Cuprous Oxide for Nonenzymatic Glucose Biosensors with Enhanced Sensitivity. *Journal of Materials Science* **2016,** *51* (21), 9696-9704.
(95) Mayer, K. M.; Hafner, J. H. Localized Surface Plasmon Resonance Sensors. *Chemical reviews* **2011,** *111* (6), 3828-3857.
(96) Qavi, A. J.; Washburn, A. L.; Byeon, J.-Y.; Bailey, R. C. Label-Free Technologies for Quantitative Multiparameter Biological Analysis. *Analytical and bioanalytical chemistry* **2009,** *394* (1), 121-135.

(97) Cai, Y.; Zhu, J.; He, J.; Yang, W.; Ma, C.; Xiong, F.; Li, F.; Chen, W.; Chen, P. Magnet Patterned Superparamagnetic Fe3o4/Au Core–Shell Nanoplasmonic Sensing Array for Label-Free High Throughput Cytokine Immunoassay. *Advanced healthcare materials* **2019,** *8* (4), 1801478.
(98) Cobley, C. M.; Chen, J.; Cho, E. C.; Wang, L. V.; Xia, Y. Gold Nanostructures: A Class of Multifunctional Materials for Biomedical Applications. *Chemical Society Reviews* **2011,** *40* (1), 44-56.
(99) Gong, S. L.; Yu, Z. J.; Meng, L. Z.; Hu, L.; He, Y. B. Dye-Molecular-Imprinted Polysiloxanes. Ii. Preparation, Characterization, and Recognition Behavior. *Journal of applied polymer science* **2004,** *93* (2), 637-643.
(100) Muyldermans, S. Applications of Nanobodies. *Annual review of animal biosciences* **2021,** *9*, 401-421.
(101) Wegner, K. D.; Lindén, S.; Jin, Z.; Jennings, T. L.; Khoulati, R. e.; van Bergen en Henegouwen, P. M.; Hildebrandt, N. Nanobodies and Nanocrystals: Highly Sensitive Quantum Dot-Based Homogeneous Fret Immunoassay for Serum-Based Egfr Detection. *Small* **2014,** *10* (4), 734-740.
(102) Akazawa-Ogawa, Y.; Nagai, H.; Hagihara, Y. Heat Denaturation of the Antibody, a Multi-Domain Protein. *Biophysical reviews* **2018,** *10* (2), 255-258.
(103) Reverdatto, S.; Burz, D. S.; Shekhtman, A. Peptide Aptamers: Development and Applications. *Current topics in medicinal chemistry* **2015,** *15* (12), 1082.
(104) Kim, S.-H.; Oh, S. S.; Kim, K.-J.; Kim, J.-E.; Park, H. Y.; Hess, O.; Kee, C.-S. Subwavelength Localization and Toroidal Dipole Moment of Spoof Surface Plasmon Polaritons. *Physical Review B* **2015,** *91* (3), 035116.
(105) Hoffman, J. M.; Margolis, K. G. Building Community in the Gut: A Role for Mucosal Serotonin. *Nature Reviews Gastroenterology & Hepatology* **2020,** *17* (1), 6-8.
(106) Mascini, M.; Palchetti, I.; Tombelli, S. Nucleic Acid and Peptide Aptamers: Fundamentals and Bioanalytical Aspects. *Angewandte Chemie International Edition* **2012,** *51* (6), 1316-1332.
(107) Pardon, E.; Laeremans, T.; Triest, S.; Rasmussen, S. G.; Wohlkönig, A.; Ruf, A.; Muyldermans, S.; Hol, W. G.; Kobilka, B. K.; Steyaert, J. A General Protocol for the Generation of Nanobodies for Structural Biology. *Nature protocols* **2014,** *9* (3), 674-693.
(108) Klarenbeek, A.; Blanchetot, C.; Schragel, G.; Sadi, A. S.; Ongenae, N.; Hemrika, W.; Wijdenes, J.; Spinelli, S.; Desmyter, A.; Cambillau, C. Combining Somatic Mutations Present in Different in Vivo Affinity-Matured Antibodies Isolated from Immunized Lama Glama Yields Ultra-Potent Antibody Therapeutics. *Protein Engineering, Design and Selection* **2016,** *29* (4), 123-133.
(109) Treuel, L.; Brandholt, S.; Maffre, P.; Wiegele, S.; Shang, L.; Nienhaus, G. U. Impact of Protein Modification on the Protein Corona on Nanoparticles and Nanoparticle–Cell Interactions. *ACS nano* **2014,** *8* (1), 503-513.
(110) Wang, G.; Chen, X.; Liu, S.; Wong, C.; Chu, S. Mechanical Chameleon through Dynamic Real-Time Plasmonic Tuning. *Acs Nano* **2016,** *10* (2), 1788-1794.
(111) Ruiz, G.; Tripathi, K.; Okyem, S.; Driskell, J. D. Ph Impacts the Orientation of Antibody Adsorbed onto Gold Nanoparticles. *Bioconjugate chemistry* **2019,** *30* (4), 1182-1191.
(112) Zhou, S.; Huo, D.; Goines, S.; Yang, T.-H.; Lyu, Z.; Zhao, M.; Gilroy, K. D.; Wu, Y.; Hood, Z. D.; Xie, M. Enabling Complete Ligand Exchange on the Surface of Gold Nanocrystals through the Deposition and Then Etching of Silver. *Journal of the American Chemical Society* **2018,** *140* (38), 11898-11901.
(113) Del Caño, R.; Gisbert-González, J. M.; González-Rodríguez, J.; Sánchez-Obrero, G.; Madueño, R.; Blázquez, M.; Pineda, T. Effective Replacement of Cetyltrimethylammonium Bromide (Ctab) by Mercaptoalkanoic Acids on Gold Nanorod (Aunr) Surfaces in Aqueous Solutions. *Nanoscale* **2020,** *12* (2), 658-668.
(114) Oliveira, J. P.; Prado, A. R.; Keijok, W. J.; Antunes, P. W. P.; Yapuchura, E. R.; Guimarães, M. C. C. Impact of Conjugation Strategies for Targeting of Antibodies in Gold Nanoparticles for Ultrasensitive Detection of 17β-Estradiol. *Scientific reports* **2019,** *9* (1), 1-8.

(115) Busch, R. T.; Karim, F.; Weis, J.; Sun, Y.; Zhao, C.; Vasquez, E. S. Optimization and Structural Stability of Gold Nanoparticle–Antibody Bioconjugates. *ACS omega* **2019,** *4* (12), 15269-15279.
(116) Kedem, O.; Vaskevich, A.; Rubinstein, I. Critical Issues in Localized Plasmon Sensing. *The Journal of Physical Chemistry C* **2014,** *118* (16), 8227-8244.
(117) Celiksoy, S.; Ye, W.; Wandner, K.; Kaefer, K.; Sönnichsen, C. Intensity-Based Single Particle Plasmon Sensing. *Nano Letters* **2021,** *21* (5), 2053-2058.
(118) Haes, A. J.; Zou, S.; Schatz, G. C.; Van Duyne, R. P. Nanoscale Optical Biosensor: Short Range Distance Dependence of the Localized Surface Plasmon Resonance of Noble Metal Nanoparticles. *The Journal of Physical Chemistry B* **2004,** *108* (22), 6961-6968.
(119) Tay, M.; Poh, C.; Rénia, L.; MacAry, P.; Ng, L. P.(2020) the Trinity of Covid-19: Immunity. *Inflammation and Intervention. Nat. Rev. Immunol 20*, 363.
(120) Wang, W.; Ye, L.; Ye, L.; Li, B.; Gao, B.; Zeng, Y.; Kong, L.; Fang, X.; Zheng, H.; Wu, Z. Up-Regulation of Il-6 and Tnf-A Induced by Sars-Coronavirus Spike Protein in Murine Macrophages Via Nf-Kb Pathway. *Virus research* **2007,** *128* (1-2), 1-8.
(121) Dosch, S. F.; Mahajan, S. D.; Collins, A. R. Sars Coronavirus Spike Protein-Induced Innate Immune Response Occurs Via Activation of the Nf-Kb Pathway in Human Monocyte Macrophages in Vitro. *Virus research* **2009,** *142* (1-2), 19-27.
(122) Huang, C.; Wang, Y.; Li, X.; Ren, L.; Zhao, J.; Hu, Y.; Zhang, L.; Fan, G.; Xu, J.; Gu, X. Clinical Features of Patients Infected with 2019 Novel Coronavirus in Wuhan, China. *The lancet* **2020,** *395* (10223), 497-506.
(123) Moore, J. B.; June, C. H. Cytokine Release Syndrome in Severe Covid-19. *Science* **2020,** *368* (6490), 473-474.
(124) Ye, Q.; Wang, B.; Mao, J. The Pathogenesis and Treatment of Thecytokine Storm'in Covid-19. *Journal of infection* **2020,** *80* (6), 607-613.
(125) Mou, L.; Jiang, X. Materials for Microfluidic Immunoassays: A Review. *Advanced healthcare materials* **2017,** *6* (15), 1601403.
(126) Han, K. N.; Li, C. A.; Seong, G. H. Microfluidic Chips for Immunoassays. *Annual review of analytical chemistry* **2013,** *6*, 119-141.
(127) Nge, P. N.; Rogers, C. I.; Woolley, A. T. Advances in Microfluidic Materials, Functions, Integration, and Applications. *Chemical reviews* **2013,** *113* (4), 2550-2583.
(128) Song, Y.; Sandford, E.; Tian, Y.; Yin, Q.; Kozminski, A. G.; Su, S.-H.; Cai, T.; Ye, Y.; Chung, M. T.; Lindstrom, R. Rapid Single-Molecule Digital Detection of Protein Biomarkers for Continuous Monitoring of Systemic Immune Disorders. *Blood* **2021,** *137* (12), 1591-1602.
(129) He, Z.; Huffman, J.; Curtin, K.; Garner, K. L.; Bowdridge, E. C.; Li, X.; Nurkiewicz, T. R.; Li, P. Composable Microfluidic Plates (Cplate): A Simple and Scalable Fluid Manipulation System for Multiplexed Enzyme-Linked Immunosorbent Assay (Elisa). *Analytical Chemistry* **2020,** *93* (3), 1489-1497.
(130) Hsu, M. N.; Wei, S. C.; Guo, S.; Phan, D. T.; Zhang, Y.; Chen, C. H. Smart Hydrogel Microfluidics for Single‐Cell Multiplexed Secretomic Analysis with High Sensitivity. *Small* **2018,** *14* (49), 1802918.
(131) Rissin, D. M.; Kan, C. W.; Campbell, T. G.; Howes, S. C.; Fournier, D. R.; Song, L.; Piech, T.; Patel, P. P.; Chang, L.; Rivnak, A. J. Single-Molecule Enzyme-Linked Immunosorbent Assay Detects Serum Proteins at Subfemtomolar Concentrations. *Nature biotechnology* **2010,** *28* (6), 595-599.
(132) Walt, D. R. Optical Methods for Single Molecule Detection and Analysis. *Analytical chemistry* **2013,** *85* (3), 1258-1263.
(133) Wu, Y.; Bennett, D.; Tilley, R. D.; Gooding, J. J. How Nanoparticles Transform Single Molecule Measurements into Quantitative Sensors. *Advanced Materials* **2020,** *32* (18), 1904339.
(134) Farka, Z.; Mickert, M. J.; Pastucha, M.; Mikušová, Z.; Skládal, P.; Gorris, H. H. Advances in Optical Single‐Molecule Detection: En Route to Supersensitive Bioaffinity Assays. *Angewandte Chemie International Edition* **2020,** *59* (27), 10746-10773.

(135) Ma, F.; Li, Y.; Tang, B.; Zhang, C.-y. Fluorescent Biosensors Based on Single-Molecule Counting. *Accounts of chemical research* **2016,** *49* (9), 1722-1730.
(136) Song, Y.; Ye, Y.; Su, S.-H.; Stephens, A.; Cai, T.; Chung, M.-T.; Han, M. K.; Newstead, M. W.; Yessayan, L.; Frame, D. A Digital Protein Microarray for Covid-19 Cytokine Storm Monitoring. *Lab on a Chip* **2021,** *21* (2), 331-343.
(137) Farka, Z.; Mickert, M. J.; Hlavacek, A.; Skládal, P.; Gorris, H. H. Single Molecule Upconversion-Linked Immunosorbent Assay with Extended Dynamic Range for the Sensitive Detection of Diagnostic Biomarkers. *Analytical chemistry* **2017,** *89* (21), 11825-11830.
(138) Peng, Y.; Xiong, B.; Peng, L.; Li, H.; He, Y.; Yeung, E. S. Recent Advances in Optical Imaging with Anisotropic Plasmonic Nanoparticles. *Analytical chemistry* **2015,** *87* (1), 200-215.
(139) Sriram, M.; Markhali, B. P.; Nicovich, P. R.; Bennett, D. T.; Reece, P. J.; Hibbert, D. B.; Tilley, R. D.; Gaus, K.; Vivekchand, S.; Gooding, J. J. A Rapid Readout for Many Single Plasmonic Nanoparticles Using Dark-Field Microscopy and Digital Color Analysis. *Biosensors and Bioelectronics* **2018,** *117*, 530-536.
(140) Poon, C.-Y.; Wei, L.; Xu, Y.; Chen, B.; Xiao, L.; Li, H.-W. Quantification of Cancer Biomarkers in Serum Using Scattering-Based Quantitative Single Particle Intensity Measurement with a Dark-Field Microscope. *Analytical chemistry* **2016,** *88* (17), 8849-8856.
(141) Li, G.; Zhu, L.; Wu, Z.; He, Y.; Tan, H.; Sun, S. Digital Concentration Readout of DNA by Absolute Quantification of Optically Countable Gold Nanorods. *Analytical chemistry* **2016,** *88* (22), 10994-11000.
(142) Ahijado-Guzman, R.; Prasad, J.; Rosman, C.; Henkel, A.; Tome, L.; Schneider, D.; Rivas, G.; Sönnichsen, C. Plasmonic Nanosensors for Simultaneous Quantification of Multiple Protein–Protein Binding Affinities. *Nano letters* **2014,** *14* (10), 5528-5532.
(143) Rosman, C.; Prasad, J.; Neiser, A.; Henkel, A.; Edgar, J.; Sönnichsen, C. Multiplexed Plasmon Sensor for Rapid Label-Free Analyte Detection. *Nano letters* **2013,** *13* (7), 3243-3247.
(144) Ament, I.; Prasad, J.; Henkel, A.; Schmachtel, S.; Sonnichsen, C. Single Unlabeled Protein Detection on Individual Plasmonic Nanoparticles. *Nano letters* **2012,** *12* (2), 1092-1095.
(145) Beuwer, M. A.; Prins, M. W.; Zijlstra, P. Stochastic Protein Interactions Monitored by Hundreds of Single-Molecule Plasmonic Biosensors. *Nano letters* **2015,** *15* (5), 3507-3511.
(146) Taylor, A. B.; Zijlstra, P. Single-Molecule Plasmon Sensing: Current Status and Future Prospects. *ACS sensors* **2017,** *2* (8), 1103-1122.
(147) Zijlstra, P.; Paulo, P. M.; Orrit, M. Optical Detection of Single Non-Absorbing Molecules Using the Surface Plasmon Resonance of a Gold Nanorod. *Nature nanotechnology* **2012,** *7* (6), 379-382.
(148) Willets, K. A.; Wilson, A. J.; Sundaresan, V.; Joshi, P. B. Super-Resolution Imaging and Plasmonics. *Chemical reviews* **2017,** *117* (11), 7538-7582.
(149) Zhou, W.; Gao, X.; Liu, D.; Chen, X. Gold Nanoparticles for in Vitro Diagnostics. *Chemical Reviews* **2015,** *115* (19), 10575-10636.
(150) Dreaden, E. C.; Alkilany, A. M.; Huang, X.; Murphy, C. J.; El-Sayed, M. A. The Golden Age: Gold Nanoparticles for Biomedicine. *Chemical Society Reviews* **2012,** *41* (7), 2740-2779.
(151) Rycenga, M.; Cobley, C. M.; Zeng, J.; Li, W.; Moran, C. H.; Zhang, Q.; Qin, D.; Xia, Y. Controlling the Synthesis and Assembly of Silver Nanostructures for Plasmonic Applications. *Chemical reviews* **2011,** *111* (6), 3669-3712.
(152) Kelly, K. L.; Coronado, E.; Zhao, L. L.; Schatz, G. C., The Optical Properties of Metal Nanoparticles: The Influence of Size, Shape, and Dielectric Environment. ACS Publications: 2003.
(153) Hermanson, G. T. *Bioconjugate Techniques*, Academic press: 2013.
(154) Skrabalak, S. E.; Au, L.; Li, X.; Xia, Y. Facile Synthesis of Ag Nanocubes and Au Nanocages. *Nature protocols* **2007,** *2* (9), 2182-2190.
(155) Xia, X.; Zeng, J.; Oetjen, L. K.; Li, Q.; Xia, Y. Quantitative Analysis of the Role Played by Poly (Vinylpyrrolidone) in Seed-Mediated Growth of Ag Nanocrystals. *Journal of the American Chemical Society* **2012,** *134* (3), 1793-1801.

(156) Otsu, N. A Threshold Selection Method from Gray-Level Histograms. *IEEE transactions on systems, man, and cybernetics* **1979,** *9* (1), 62-66.
(157) Johnson, P. B.; Christy, R.-W. Optical Constants of the Noble Metals. *Physical review B* **1972,** *6* (12), 4370.
(158) Zhang, Q.; Li, W.; Moran, C.; Zeng, J.; Chen, J.; Wen, L.-P.; Xia, Y. Seed-Mediated Synthesis of Ag Nanocubes with Controllable Edge Lengths in the Range of 30− 200 Nm and Comparison of Their Optical Properties. *Journal of the American Chemical Society* **2010,** *132* (32), 11372-11378.
(159) Moran, C. H.; Rycenga, M.; Zhang, Q.; Xia, Y. Replacement of Poly (Vinyl Pyrrolidone) by Thiols: A Systematic Study of Ag Nanocube Functionalization by Surface-Enhanced Raman Scattering. *The Journal of Physical Chemistry C* **2011,** *115* (44), 21852-21857.
(160) Nehilla, B. J.; Vu, T. Q.; Desai, T. A. Stoichiometry-Dependent Formation of Quantum Dot− Antibody Bioconjugates: A Complementary Atomic Force Microscopy and Agarose Gel Electrophoresis Study. *The Journal of Physical Chemistry B* **2005,** *109* (44), 20724-20730.
(161) Xia, Y.; Ramgopal, Y.; Li, H.; Shang, L.; Srinivas, P.; Kickhoefer, V. A.; Rome, L. H.; Preiser, P. R.; Boey, F.; Zhang, H. Immobilization of Recombinant Vault Nanoparticles on Solid Substrates. *ACS nano* **2010,** *4* (3), 1417-1424.
(162) Ming, T.; Chen, H.; Jiang, R.; Li, Q.; Wang, J. Plasmon-Controlled Fluorescence: Beyond the Intensity Enhancement. *The Journal of Physical Chemistry Letters* **2012,** *3* (2), 191-202.
(163) Thomas, G. D. Effect of Dose, Molecular Size, and Binding Affinity on Uptake of Antibodies. In *Drug Targeting*; Springer: 2000; pp 115-132.
(164) He, H.; Yan, S.; Lyu, D.; Xu, M.; Ye, R.; Zheng, P.; Lu, X.; Wang, L.; Ren, B., Deep Learning for Biospectroscopy and Biospectral Imaging: State-of-the-Art and Perspectives. ACS Publications: 2021.
(165) Zhang, D.; Wu, G.; Zhou, L. *Machine Learning in Medical Imaging*, Springer: 2014.
(166) Song, Y.; Zhao, J.; Cai, T.; Stephens, A.; Su, S.-H.; Sandford, E.; Flora, C.; Singer, B. H.; Ghosh, M.; Choi, S. W. Machine Learning-Based Cytokine Microarray Digital Immunoassay Analysis. *Biosensors and Bioelectronics* **2021,** *180*, 113088.
(167) Zhang, X.; Liu, Z. Superlenses to Overcome the Diffraction Limit. *Nature materials* **2008,** *7* (6), 435-441.
(168) Wen, S.; Liu, Y.; Wang, F.; Lin, G.; Zhou, J.; Shi, B.; Suh, Y. D.; Jin, D. Nanorods with Multidimensional Optical Information Beyond the Diffraction Limit. *Nature communications* **2020,** *11* (1), 1-8.
(169) Herold, T.; Jurinovic, V.; Arnreich, C.; Lipworth, B. J.; Hellmuth, J. C.; von Bergwelt-Baildon, M.; Klein, M.; Weinberger, T. Elevated Levels of Il-6 and Crp Predict the Need for Mechanical Ventilation in Covid-19. *Journal of Allergy and Clinical Immunology* **2020,** *146* (1), 128-136. e4.
(170) Yessayan, L.; Szamosfalvi, B.; Napolitano, L.; Singer, B.; Kurabayashi, K.; Song, Y.; Westover, A.; Humes, H. D. Treatment of Cytokine Storm in Covid-19 Patients with Immunomodulatory Therapy. *Asaio Journal* **2020,** *66* (10), 1079-1083.
(171) Luo, P.; Liu, Y.; Qiu, L.; Liu, X.; Liu, D.; Li, J. Tocilizumab Treatment in Covid‐19: A Single Center Experience. *Journal of medical virology* **2020,** *92* (7), 814-818.
(172) Alzghari, S. K.; Acuña, V. S. Supportive Treatment with Tocilizumab for Covid-19: A Systematic Review. *Journal of Clinical Virology* **2020,** *127*, 104380.
(173) Zraika, S.; Hull, R.; Verchere, C.; Clark, A.; Potter, K.; Fraser, P.; Raleigh, D.; Kahn, S. Toxic Oligomers and Islet Beta Cell Death: Guilty by Association or Convicted by Circumstantial Evidence? *Diabetologia* **2010,** *53* (6), 1046-1056.
(174) Schmitz, O.; Brock, B.; Rungby, J. Amylin Agonists: A Novel Approach in the Treatment of Diabetes. *Diabetes* **2004,** *53* (suppl 3), S233-S238.
(175) Ke, P. C.; Sani, M.-A.; Ding, F.; Kakinen, A.; Javed, I.; Separovic, F.; Davis, T. P.; Mezzenga, R. Implications of Peptide Assemblies in Amyloid Diseases. *Chemical Society Reviews* **2017,** *46* (21), 6492-6531.

(176) Haataja, L.; Gurlo, T.; Huang, C. J.; Butler, P. C. Islet Amyloid in Type 2 Diabetes, and the Toxic Oligomer Hypothesis. *Endocrine reviews* **2008,** *29* (3), 303-316.
(177) Javed, I.; Yu, T.; Peng, G.; Sánchez-Ferrer, A.; Faridi, A.; Kakinen, A.; Zhao, M.; Mezzenga, R.; Davis, T. P.; Lin, S. In Vivo Mitigation of Amyloidogenesis through Functional–Pathogenic Double-Protein Coronae. *Nano letters* **2018,** *18* (9), 5797-5804.
(178) DeToma, A. S.; Salamekh, S.; Ramamoorthy, A.; Lim, M. H. Misfolded Proteins in Alzheimer's Disease and Type Ii Diabetes. *Chemical Society Reviews* **2012,** *41* (2), 608-621.
(179) Knowles, T. P.; Vendruscolo, M.; Dobson, C. M. The Amyloid State and Its Association with Protein Misfolding Diseases. *Nature reviews Molecular cell biology* **2014,** *15* (6), 384-396.
(180) Eisenberg, D.; Jucker, M. The Amyloid State of Proteins in Human Diseases. *Cell* **2012,** *148* (6), 1188-1203.
(181) Li, L.; Guest, W.; Huang, A.; Plotkin, S. S.; Cashman, N. R. Immunological Mimicry of Prpc–Prpsc Interactions: Antibody-Induced Prp Misfolding. *Protein Engineering, Design & Selection* **2009,** *22* (8), 523-529.
(182) Honig, L. S.; Vellas, B.; Woodward, M.; Boada, M.; Bullock, R.; Borrie, M.; Hager, K.; Andreasen, N.; Scarpini, E.; Liu-Seifert, H. Trial of Solanezumab for Mild Dementia Due to Alzheimer's Disease. *New England Journal of Medicine* **2018,** *378* (4), 321-330.
(183) Abbott, A.; Dolgin, E. Failed Alzheimer's Trial Does Not Kill Leading Theory of Disease. *Nature News* **2016,** *540* (7631), 15.
(184) Sevigny, J.; Chiao, P.; Bussière, T.; Weinreb, P. H.; Williams, L.; Maier, M.; Dunstan, R.; Salloway, S.; Chen, T.; Ling, Y. The Antibody Aducanumab Reduces Aβ Plaques in Alzheimer's Disease. *Nature* **2016,** *537* (7618), 50-56.
(185) Kayed, R.; Head, E.; Sarsoza, F.; Saing, T.; Cotman, C. W.; Necula, M.; Margol, L.; Wu, J.; Breydo, L.; Thompson, J. L. Fibril Specific, Conformation Dependent Antibodies Recognize a Generic Epitope Common to Amyloid Fibrils and Fibrillar Oligomers That Is Absent in Prefibrillar Oligomers. *Molecular neurodegeneration* **2007,** *2* (1), 1-11.
(186) Hefti, F.; Goure, W. F.; Jerecic, J.; Iverson, K. S.; Walicke, P. A.; Krafft, G. A. The Case for Soluble Aβ Oligomers as a Drug Target in Alzheimer's Disease. *Trends in Pharmacological Sciences* **2013,** *34* (5), 261-266.
(187) Kayed, R.; Head, E.; Thompson, J. L.; McIntire, T. M.; Milton, S. C.; Cotman, C. W.; Glabe, C. G. Common Structure of Soluble Amyloid Oligomers Implies Common Mechanism of Pathogenesis. *Science* **2003,** *300* (5618), 486-489.
(188) Javed, I.; Sun, Y.; Adamcik, J.; Wang, B.; Kakinen, A.; Pilkington, E. H.; Ding, F.; Mezzenga, R.; Davis, T. P.; Ke, P. C. Cofibrillization of Pathogenic and Functional Amyloid Proteins with Gold Nanoparticles against Amyloidogenesis. *Biomacromolecules* **2017,** *18* (12), 4316-4322.
(189) Gowen, A. A.; O'Donnell, C. P.; Cullen, P. J.; Downey, G.; Frias, J. M. Hyperspectral Imaging–an Emerging Process Analytical Tool for Food Quality and Safety Control. *Trends in food science & technology* **2007,** *18* (12), 590-598.
(190) Wen, Y.; Geitner, N. K.; Chen, R.; Ding, F.; Chen, P.; Andorfer, R. E.; Govindan, P. N.; Ke, P. C. Binding of Cytoskeletal Proteins with Silver Nanoparticles. *Rsc Advances* **2013,** *3* (44), 22002-22007.
(191) Lim, D.-H.; Jang, J.; Kim, S.; Kang, T.; Lee, K.; Choi, I.-H. The Effects of Sub-Lethal Concentrations of Silver Nanoparticles on Inflammatory and Stress Genes in Human Macrophages Using Cdna Microarray Analysis. *Biomaterials* **2012,** *33* (18), 4690-4699.
(192) Smith, B. R.; Ghosn, E. E. B.; Rallapalli, H.; Prescher, J. A.; Larson, T.; Herzenberg, L. A.; Gambhir, S. S. Selective Uptake of Single-Walled Carbon Nanotubes by Circulating Monocytes for Enhanced Tumour Delivery. *Nature nanotechnology* **2014,** *9* (6), 481-487.

(193) Mortimer, M.; Gogos, A.; Bartolomé, N.; Kahru, A.; Bucheli, T. D.; Slaveykova, V. I. Potential of Hyperspectral Imaging Microscopy for Semi-Quantitative Analysis of Nanoparticle Uptake by Protozoa. *Environmental science & technology* **2014,** *48* (15), 8760-8767.
(194) Badireddy, A. R.; Wiesner, M. R.; Liu, J. Detection, Characterization, and Abundance of Engineered Nanoparticles in Complex Waters by Hyperspectral Imagery with Enhanced Darkfield Microscopy. *Environmental science & technology* **2012,** *46* (18), 10081-10088.
(195) Haiss, W.; Thanh, N. T.; Aveyard, J.; Fernig, D. G. Determination of Size and Concentration of Gold Nanoparticles from Uv− Vis Spectra. *Analytical chemistry* **2007,** *79* (11), 4215-4221.
(196) Javed, I.; Hussain, S. Z.; Shahzad, A.; Khan, J. M.; Rehman, M.; Usman, F.; Razi, M. T.; Shah, M. R.; Hussain, I. Lecithin-Gold Hybrid Nanocarriers as Efficient and Ph Selective Vehicles for Oral Delivery of Diacerein—in-Vitro and in-Vivo Study. *Colloids and Surfaces B: Biointerfaces* **2016,** *141*, 1-9.
(197) Liu, X.; Atwater, M.; Wang, J.; Huo, Q. Extinction Coefficient of Gold Nanoparticles with Different Sizes and Different Capping Ligands. *Colloids and Surfaces B: Biointerfaces* **2007,** *58* (1), 3-7.
(198) Whitmore, L.; Wallace, B. A. Protein Secondary Structure Analyses from Circular Dichroism Spectroscopy: Methods and Reference Databases. *Biopolymers: Original Research on Biomolecules* **2008,** *89* (5), 392-400.
(199) Westwell-Roper, C.; Denroche, H. C.; Ehses, J. A.; Verchere, C. B. Differential Activation of Innate Immune Pathways by Distinct Islet Amyloid Polypeptide (Iapp) Aggregates. *Journal of Biological Chemistry* **2016,** *291* (17), 8908-8917.
(200) Ding, F.; Radic, S.; Chen, R.; Chen, P.; Geitner, N. K.; Brown, J. M.; Ke, P. C. Direct Observation of a Single Nanoparticle–Ubiquitin Corona Formation. *Nanoscale* **2013,** *5* (19), 9162-9169.
(201) Schöttler, S.; Becker, G.; Winzen, S.; Steinbach, T.; Mohr, K.; Landfester, K.; Mailänder, V.; Wurm, F. R. Protein Adsorption Is Required for Stealth Effect of Poly (Ethylene Glycol)-and Poly (Phosphoester)-Coated Nanocarriers. *Nature nanotechnology* **2016,** *11* (4), 372-377.
(202) Chen, G.; Roy, I.; Yang, C.; Prasad, P. N. Nanochemistry and Nanomedicine for Nanoparticle-Based Diagnostics and Therapy. *Chemical reviews* **2016,** *116* (5), 2826-2885.
(203) Blanco, E.; Shen, H.; Ferrari, M. Principles of Nanoparticle Design for Overcoming Biological Barriers to Drug Delivery. *Nature biotechnology* **2015,** *33* (9), 941-951.
(204) Mahmoud, M. A.; Chamanzar, M.; Adibi, A.; El-Sayed, M. A. Effect of the Dielectric Constant of the Surrounding Medium and the Substrate on the Surface Plasmon Resonance Spectrum and Sensitivity Factors of Highly Symmetric Systems: Silver Nanocubes. *Journal of the American Chemical Society* **2012,** *134* (14), 6434-6442.
(205) Mahmoud, M.; Snyder, B.; El-Sayed, M. Surface Plasmon Fields and Coupling in the Hollow Gold Nanoparticles and Surface-Enhanced Raman Spectroscopy. Theory and Experiment. *The Journal of Physical Chemistry C* **2010,** *114* (16), 7436-7443.
(206) Mahmoud, M.; El-Sayed, M. Aggregation of Gold Nanoframes Reduces, Rather Than Enhances, Sers Efficiency Due to the Trade-Off of the Inter-and Intraparticle Plasmonic Fields. *Nano letters* **2009,** *9* (8), 3025-3031.
(207) Corbett, J.; Wang, J.; Sweetland, M.; Lancaster, J. R.; McDaniel, M. Interleukin 1 Beta Induces the Formation of Nitric Oxide by Beta-Cells Purified from Rodent Islets of Langerhans. Evidence for the Beta-Cell as a Source and Site of Action of Nitric Oxide. *The Journal of clinical investigation* **1992,** *90* (6), 2384-2391.
(208) Bendtzen, K.; Mandrup-Poulsen, T.; Nerup, J.; Nielsen, J. H.; Dinarello, C. A.; Svenson, M. Cytotoxicity of Human Pi 7 Interleukin-1 for Pancreatic Islets of Langerhans. *Science* **1986,** *232* (4757), 1545-1547.
(209) Cedervall, T.; Lynch, I.; Lindman, S.; Berggård, T.; Thulin, E.; Nilsson, H.; Dawson, K. A.; Linse, S. Understanding the Nanoparticle–Protein Corona Using Methods to Quantify Exchange Rates and Affinities of Proteins for Nanoparticles. *Proceedings of the National Academy of Sciences* **2007,** *104* (7), 2050-2055.

(210) Ai, W.; Li, H.; Song, N.; Li, L.; Chen, H. Optimal Method to Stimulate Cytokine Production and Its Use in Immunotoxicity Assessment. *International journal of environmental research and public health* **2013,** *10* (9), 3834-3842.
(211) Baud, V.; Karin, M. Signal Transduction by Tumor Necrosis Factor and Its Relatives. *Trends in cell biology* **2001,** *11* (9), 372-377.
(212) Jiang, W.; Kim, B. Y.; Rutka, J. T.; Chan, W. C. Nanoparticle-Mediated Cellular Response Is Size-Dependent. *Nature nanotechnology* **2008,** *3* (3), 145-150.
(213) Deng, Z. J.; Liang, M.; Monteiro, M.; Toth, I.; Minchin, R. F. Nanoparticle-Induced Unfolding of Fibrinogen Promotes Mac-1 Receptor Activation and Inflammation. *Nature nanotechnology* **2011,** *6* (1), 39-44.
(214) Lynch, I.; Salvati, A.; Dawson, K. A. What Does the Cell See? *Nature nanotechnology* **2009,** *4* (9), 546-547.